

TECHNISCHE UNIVERSITÄT MÜNCHEN

Department Chemie

Lehrstuhl I für Technische Chemie

**Efficient Methanol Synthesis Catalysts: Long-Term
Stability and Deactivation Phenomena**

Matthias Benedikt Fichtl

Vollständiger Abdruck der von der Fakultät für Chemie der Technischen Universität München zur Erlangung des akademischen Grades eines

Doktors der Naturwissenschaften (Dr. rer. nat.)

genehmigten Dissertation.

Vorsitzende: Univ.-Prof. Dr. S. Weinkauf

Prüfer der Dissertation: 1. Univ.-Prof. Dr. K.-O. Hinrichsen
2. Univ.-Prof. Dr. K. Köhler
3. Univ.-Prof. Dr. T. Nilges

Die Dissertation wurde am 14.10.2014 bei der Technischen Universität München eingereicht und durch die Fakultät für Chemie am 08.12.2014 angenommen.

Acknowledgments

This work would not have been possible without the help and support of so many people in so many ways. I would like to thank all persons who have helped me to overcome the scientific and non-scientific challenges, encouraged me on my way or just were there and had fun working with me.

I thank Prof. Dr.-Ing. Kai-Olaf Hinrichsen for providing me with such an interesting and challenging research topic. Our discussions always offered fresh ideas, insights and opportunities to tackle the scientific problems and I am very grateful for the trust he has placed in me and my decisions.

Special thanks go to all the people, I got to know and appreciate in course of the cooperation project: Prof. Dr. Malte Behrens, Prof. Dr. Robert Schlögl, Julia Schumann, Dr. Stefan Zander from the Fritz Haber Institute in Berlin, Prof. Dr. Martin Muhler, Dr. Wilma Busser, Dr. Stefan Kaluza, Dr. Volker Hagen from the Ruhr University Bochum, Dr.-Ing. Andreas Reitzmann, Dr. Nikolas Jacobsen, Dr. Tobias Henkel, Dr. Willi Brandstädter, and Dr. Patrick Kurr from Clariant. The different aspects and fields of expertise you contributed made it the interesting and exciting task it was. I enjoyed working with you and I am grateful for the very positive and encouraging working atmosphere.

Doubtless to say, without my colleagues and friends at the university this work would not have turned out the way it has. You made my Ph.D. the enjoyable and interesting experience, I would not hesitate to do again. I will miss all the fun, scientific and non-scientific discussions, barbeques, trips, Nerf Gun battles, beer and whisky tastings we had and I wish you all the best for your future goals. Special thanks go to Franz, David, Moritz and Anne, for enduring me in the office and trying to keep calm during my sometimes very spontaneous ideas...

Last but not least I would like to thank my family who made it possible to pursue my goals and wishes in the first place. Thank you for the extraordinary support during my studies and for always being there when needed.

"A scientist in his laboratory is not a mere technician: he is also a child confronting natural phenomena that impress him as though they were fairy tales."

Marie Curie

Abstract

Methanol counts among the most important basic chemicals and represents a fundamental C1 building block for other chemicals. It provides access to a whole variety of important industrial products, like formaldehyde, acetic acid, dimethyl ether (DME) or methyl-*tert*-butylether (MTBE) which is used for upgrading of low octane number gasoline. The methanol to olefins (MTO) or methanol to propylene (MTP) processes offer the possibility to synthesize important monomers for commodity polymers from different carbon sources. Apart from the chemical industry usage, the liquid can also be mixed with gasoline or directly used as fuel for cars. Methanol is commonly produced by hydrogenation of a feed containing carbon monoxide and carbon dioxide using Cu/ZnO/Al₂O₃ catalysts. Since it is a common platform molecule and can in general be generated from sustainable H₂ and CO₂ sources, it gathers rising attention as a renewable energy storage and carrier, which led to the term "methanol economy".

Deactivation of heterogeneous catalysts is a major issue in application-oriented research and majorly defines a catalyst's suitability for plant operation. In case of methanol synthesis catalysts the lifetime is limited; however detailed information about catalyst deactivation and structural changes during this process is very scarce and often not applicable under typical industrial conditions: many of the literature-known models present a very rapid deactivation behavior which leads to a virtually inactive catalyst after a few months. Apart from external deactivation factors like catalyst poisoning, the intrinsic deactivation is commonly attributed to sintering phenomena. However, only few studies about the sintering mechanism or stabilizing effects for methanol synthesis catalysts are available. In this thesis multiple catalysts are selected, aged under industrial conditions for more than 1000 h time on stream and systematically characterized with multiple in situ and ex situ methods. Main focus lies on the microstructural changes of the active catalyst and the derivation of different deactivation mechanisms. Furthermore, two methods to determine the copper surface area of such catalysts - the reactive N₂O frontal chromatography and the temperature programmed H₂ desorption - are studied in detail and revised. The scientific results of the thesis are presented in four different contributions.

In the first contribution the main focus is set on deactivation behavior of five different high performance Cu/ZnO/Al₂O₃ catalysts. After activation, the catalysts are aged under constant conditions at 573 K and 60 bar for 240, 480, 720 and 960 h respectively. The fresh activated and the aged samples are minutely characterized via elemental analysis, high resolution transmission electron spectroscopy (HR-TEM), x-ray diffraction (XRD), nitrogen physisorption (BET), H₂-TPD, N₂O-RFC and kinetic experiments. The results indicate that the phase composition of the catalyst precursor has a major

influence on the aging process and mechanism. In the typically present ex-zinc-malachite structure the ZnO acts as structural spacer and keeps the copper particles apart. During the deactivation process, this spacer is locally depleted, leading to new contacts between the copper particles and the formation of stable twinning boundaries. In excess of alumina, this effect is accelerated by the crystallization of ZnAl_2O_4 which acts as a sink for the formerly mobile ZnO species. In the ex-aurichalcite and hydrotalcite like structure the copper particles are well stabilized by embedding them in either a partially amorphous ZnO or an amorphous $\text{ZnO}/\text{Al}_2\text{O}_3$ matrix respectively. This prevents sintering of the particles, however, the strong embedding and the strong Cu-ZnO interaction block active sites from the gas phase.

In the second contribution three of the five catalysts are systematically analyzed for their time dependent catalytic activity. The systems are aged under equilibrium conditions at 493 K, 523 K, and 553 K and at a pressure of 60 bar. Approximately every 20 hours the catalytic activity is determined by measuring the methanol yield under kinetic conditions at 483 K and at a pressure of 60 bar. The results indicate that the catalyst deactivation can be described by third and fourth order power law models and that the nature of the active site does not change significantly during this process. Furthermore, the particle size distribution determined by HR-TEM measurements at 240, 480, 720 and 960 h TOS is evaluated with sintering models like Ostwald Ripening and different collision models. It can be concluded that sintering in ex-zinc-malachite type precursors can be best described by a random collision of copper particles independent of the respective particle diameter. This is in agreement with results of the theory that local depletion of the ZnO in between the copper particles promotes the sintering process.

In the third contribution a comparative analysis of H_2 -TPD and N_2O -RFC measurements on different supported copper systems is presented. The results allow the conclusion that the N_2O -RFC not only oxidizes the copper surface area, but also reacts with ZnO oxygen defect sites present at the Cu-ZnO interface. This leads to an overestimation of the exposed metal surface area. In absence of ZnO a linear correlation between the copper surface area according to the N_2O -RFC and H_2 -TPD can be established for Al_2O_3 and MgO supported systems, as well as for the unsupported polycrystalline metal. The copper surface is saturated with hydrogen at a $2/3$ ML coverage, i.e. three copper atoms bind two hydrogen atoms.

The fourth contribution is focused on H_2 -TPD studies on polycrystalline and Al_2O_3 supported copper. Two model systems are synthesized and systematically analyzed via H_2 -TPD and model parameters for a second order H_2 desorption kinetics are determined. The results lead to the conclusion that the desorption kinetics for hydrogen adsorbed on polycrystalline Cu and $\text{Cu}/\text{Al}_2\text{O}_3$ are equal and that Al_2O_3 has no significant influence on the adsorption properties of the copper surface. Furthermore it is shown, that the

desorption signals can also be described by three single desorption processes from the copper low index planes Cu(111), Cu(110) and Cu(100). Here, the ratio of the three index planes is a fixed value derived by the Wulff construction.

Inhaltszusammenfassung

Methanol zählt zu den wichtigsten Basischemikalien und stellt einen bedeutenden C1 Baustein für andere Chemikalien dar. Es bietet Zugang zu einer Vielzahl wichtiger industrieller Chemikalien, wie Formaldehyd, Essigsäure, Dimethylether (DME) oder Methyl-tert-butylether (MTBE). Letzterer wird für das Upgrading von Ottokraftstoffen mit geringer Oktanzahl verwendet. Mittels der Methanol-zu-Olefin (MTO) oder Methanol-zu-Propen (MTP) Prozesse eröffnet sich die Möglichkeit, Monomere für den Massenmarkt aus verschiedenen Kohlenstoffquellen zu erzeugen. Unabhängig vom Gebrauch in der chemischen Industrie kann die Flüssigkeit mit Ottokraftstoffen gemischt oder direkt als Kraftstoff verwendet werden. Methanol wird üblicherweise durch Hydrierung eines kohlenstoffmonoxid- und kohlenstoffdioxidhaltigen Feedstroms über Cu/ZnO/Al₂O₃-Katalysatoren gewonnen. Da es ein gängiges Plattformmolekül ist und prinzipiell auch aus CO₂ und regenerativ gewonnenem H₂ hergestellt werden kann, gewinnt es zunehmend an Aufmerksamkeit als erneuerbarer Energiespeicher und -träger. Dies wurde durch den Term der „Methanolwirtschaft“ geprägt.

Das Desaktivierungsverhalten heterogener Katalysatoren ist ein bedeutendes Thema in der anwendungsorientierten Forschung und bestimmt maßgeblich über die Eignung eines Katalysatorsystems zum industriellen Einsatz. Im Falle von Katalysatoren zur Methanolsynthese ist die Lebensspanne eines Katalysators auf einige Jahre begrenzt. Jedoch sind nur wenig Informationen über das genaue Desaktivierungsverhalten und strukturelle Änderungen während des Desaktivierungsvorganges verfügbar und diese zudem nicht auf industrielle Bedingungen anwendbar. Viele der literaturbekannten Modelle zeigen ein sehr schnelles Desaktivierungsverhalten, welches in wenigen Monaten zu einem nahezu inaktiven Katalysatorsystem führt. Neben externen Desaktivierungsfaktoren wie Katalysatorvergiftung wird die Desaktivierung intrinsischen Vorgängen wie Sinterphänomenen zugeschrieben, jedoch gibt es nur wenige Studien zu Sintermechanismen oder stabilisierenden Effekten. In dieser Arbeit werden mehrere verschiedene Katalysatoren ausgewählt, für mehr als 1000 Stunden unter industriellen Bedingungen gealtert und systematisch mit einer Vielzahl an in-situ und ex-situ Methoden charakterisiert. Der Schwerpunkt liegt hierbei auf den mikrostrukturellen Änderungen des Katalysatorsystems. Hieraus werden verschiedene Desaktivierungsmechanismen abgeleitet. Weiterhin werden zwei Methoden zur Bestimmung der Kupferoberfläche solcher Katalysatoren - die reaktive N₂O-Frontalchromatographie und die temperaturprogrammierte H₂-Desorption - detailliert betrachtet. Die wissenschaftlichen Erkenntnisse dieser Arbeit sind in vier inhaltlich geschlossenen Kapiteln verfasst.

Im ersten Beitrag liegt der Schwerpunkt auf der Darstellung des Desaktivierungsverhaltens von fünf verschiedenen, teils hoch aktiven, Cu/ZnO/Al₂O₃-Katalysatoren.

Nach dem Aktivierungsprozess werden sie für 240, 480, 720 und 960 Stunden unter konstanten Bedingungen bei einer Temperatur von 523 K und einem Druck von 60 bar gealtert. Zusammen mit dem frisch aktivierten Katalysatormaterial werden diese anschließend eingehend mit den folgenden Techniken charakterisiert: Elementaranalyse, hochauflösende Transmissionselektronenmikroskopie (HR-TEM), Pulverdiffraktometrie (XRD), Stickstoffadsorption (BET), H_2 -TPD, N_2O -RFC und kinetische Messungen. Die Ergebnisse lassen den Schluss zu, dass die Phasenzusammensetzung der Precursoren einen maßgeblichen Einfluss auf den Alterungsvorgang und -mechanismus hat. In den hauptsächlich vorliegenden ex-Zink-Malachit-Strukturen agiert ZnO als räumliches Trennmittel für die Kupferpartikel. Im Verlauf der Desaktivierung wird dieser Trenner lokal entzogen, was zu neuen Kontaktstellen zwischen Kupferpartikeln und zur Bildung von stabilen Zwillingsgrenzen führt. In Gegenwart eines Überschusses an Aluminium wird dieser Effekt durch Kristallisation von $ZnAl_2O_4$, welches als thermodynamische Senke für das ursprünglich mobile ZnO agiert, beschleunigt. Im Falle von ex-Aurichalcit und Hydrotalcit-ähnlichen Strukturen sind die Kupferpartikel durch Einbettung in eine partiell amorphe ZnO-Matrix oder eine amorphe ZnO/Al_2O_3 -Matrix stabilisiert. Dies verhindert Sintervorgänge, jedoch führt die starke Einbettung der Partikel zu deren Abschottung von der Gasphase.

Im zweiten Beitrag werden drei der fünf Katalysatoren systematisch auf ihr zeitabhängiges Aktivitätsverhalten hin untersucht. Die Systeme werden hierzu unter Gleichgewichtsbedingungen bei 493 K, 523 K, und 553 K sowie einem Druck von 60 bar gealtert. Ungefähr alle 20 Stunden wird die Katalysatoraktivität durch Bestimmung der Methanolausbeute unter kinetischen Bedingungen, einer Temperatur von 483 K sowie einem Druck von 60 bar gemessen. Die Ergebnisse deuten an, dass das Desaktivierungsverhalten der Katalysatoren mit Potenzansätzen dritter und vierter Ordnung bestimmt werden kann und dass die Natur des aktiven Zentrums keinen signifikanten Änderungen unterworfen ist. Des Weiteren wird die Partikelgrößenverteilung der Katalysatoren, welche nach einer Standzeit von 240, 480, 720 und 960 Stunden mittels den HR-TEM Messungen bestimmt wurde, mit verschiedenen Sintermodellen wie Ostwald-Reifung und unterschiedlichen Kollisionsmodellen verglichen. Aus den Ergebnissen kann geschlossen werden, dass das Sinterverhalten von ex-Zink-Malachit-Precursoren unabhängig vom Partikeldurchmesser mittels eines zufälligen Kollisionsmodells am besten beschrieben werden kann. Dies ist im Einklang mit der Annahme, dass Sinterprozesse durch lokale Abreicherung des ZnO-Trenners zwischen den Kupferpartikeln hervorgerufen werden.

Im dritten Beitrag wird ein Vergleich von H_2 -TPD und N_2O -RFC Messungen vorgestellt. Die Ergebnisse führen zu dem Schluss, dass die N_2O -RFC nicht nur die Kupferoberfläche oxidiert, sondern auch mit ZnO_x -Fehlstellen reagiert, welche an der

Cu-ZnO-Grenzfläche vorhanden sind. Dies führt zu einer Überschätzung der Kupfer-Metalloberfläche. In Abwesenheit von ZnO kann eine lineare Korrelation der Kupferoberfläche nach N₂O-RFC und H₂-TPD für polykristallines Kupfer, sowie für Al₂O₃ und MgO geträgerte Systeme erstellt werden. Die Kupferoberfläche ist hier mit 2/3 ML adsorbiertem Wasserstoff bedeckt, d.h. drei Kupferatome binden zwei Wasserstoffatome.

Der vierte Beitrag konzentriert sich auf H₂-TPD Studien mit polykristallinem und Al₂O₃ geträgertem Kupfer. Hierfür wurden zwei Modellsysteme hergestellt, systematisch via H₂-TPD untersucht und die Modellparameter einer H₂-Desorptionskinetik zweiter Ordnung bestimmt. Aus den Ergebnissen kann geschlossen werden, dass die Desorptionskinetiken für Wasserstoff, welcher auf polykristallinem und Al₂O₃ geträgertem Kupfer adsorbiert ist, gleich sind. Somit hat Al₂O₃ keinen signifikanten Einfluss auf die Adsorptionseigenschaften der Kupferoberfläche. Des Weiteren wird gezeigt, dass das Desorptionssignal einer Überlagerung von Desorptionsprozessen von den niedrig indizierten Kupferoberflächen Cu(100), Cu(110) und Cu(111) entspricht. Das Verhältnis der einzelnen Flächen zueinander ist hierbei durch die Wulff-Konstruktion fest vorgegeben.

Contents

1	Introduction	1
1.1	Motivation	1
1.2	Objectives	3
2	Theoretical Background	6
2.1	General Aspects of Methanol Synthesis	6
2.2	Mechanistic Aspects	9
2.3	The Industrial Catalyst	11
2.4	Catalyst Deactivation	15
3	Experimental	26
3.1	Catalyst Preparation and Characterization	26
3.2	Setup for Long-term Kinetic Studies	28
3.3	Setup for Short-term and Transient Studies	31
4	Deactivation Mechanisms on Cu/ZnO/Al₂O₃ Methanol Synthesis Catalysts	34
4.1	Abstract	34
4.2	Introduction	34
4.3	Experimental	36
4.3.1	Catalyst Preparation	36
4.3.2	Deactivation and Kinetic Experiments	37
4.4	Catalyst Characterization	39
4.4.1	Transmission electron spectroscopy (TEM, TEM-EDX)	39
4.4.2	X-ray Diffraction (XRD)	39
4.4.3	Reactive N ₂ O Frontal Chromatography (N ₂ O-RFC)	39
4.4.4	Nitrogen Physisorption	39
4.4.5	H ₂ -TPD Measurements (H ₂ -TPD)	40
4.5	Results	41
4.5.1	Activity and Copper Surface Area	41
4.5.2	Transmission Electron Spectroscopy	42
4.5.3	XRD Analysis	45

4.5.4	Particle Surface Area and Pore Structure	47
4.5.5	Temperature Programmed Hydrogen Desorption	48
4.6	Discussion	51
4.7	Conclusion	55
4.8	Supporting Information	56
5	Kinetics of Deactivation on Cu/ZnO/Al₂O₃ Methanol Synthesis Catalysts	64
5.1	Abstract	64
5.2	Introduction	64
5.3	Experimental and Computational Methods	66
5.3.1	Catalyst preparation	66
5.3.2	Deactivation and Kinetic Experiments	67
5.3.3	Reactive N ₂ O Frontal Chromatography (N ₂ O-RFC)	69
5.3.4	Modeling Approach	70
5.4	Results	71
5.4.1	Deactivation Behavior	71
5.4.2	Modeling Results	76
5.5	Discussion	78
5.6	Summary	83
5.7	Supporting Information	84
5.7.1	Ostwald Ripening	84
5.7.2	Coalescence	86
6	Counting of Oxygen Defects vs. Metal Surface Sites	91
6.1	Abstract	91
6.2	Methods and Results	91
6.3	Supporting Information	100
6.3.1	Catalyst Preparation and Characterization	100
6.3.2	Experimental Setup, Activation Procedure and Activity Study . .	102
6.3.3	Hydrogen Temperature Programmed Desorption (H ₂ -TPD)	103
6.3.4	Nitrous Oxide - Reactive Frontal Chromatography (N ₂ O-RFC) and Defect Concentration	105
6.3.5	Model For The Microstructure of Common Cu/ZnO/Al ₂ O ₃ Methanol Synthesis Catalysts	107
6.4	Copyright Information	109
7	On the temperature programmed desorption of hydrogen	113
7.1	Abstract	113
7.2	Introduction	113

7.3	Experimental and Computational Methods	115
7.3.1	Catalyst preparation	115
7.3.2	Hydrogen Temperature Programmed Desorption (H ₂ -TPD)	116
7.3.3	Reactive N ₂ O Frontal Chromatography	117
7.3.4	Modelling of the Desorption Signal	118
7.3.5	Results and Discussion	121
7.3.6	Conclusion	125
7.4	Supporting Information	125
8	Closing	129
8.1	Summary	129
8.2	Outlook	132
	Curriculum Vitae	134
	Publications	136
	Licensing Information	138
	List of Figures	146
	List of Tables	150
	Abschließende Erklärung	152

1 Introduction

In this thesis the deactivation behavior of Cu/ZnO/Al₂O₃ methanol synthesis catalysts is systematically analyzed. Kinetic long-term measurements under controlled conditions are combined with detailed ex situ and in situ characterization of the deactivated systems in order to gain insight into the microstructural changes of the catalyst during the aging process.

1.1 Motivation

Methanol (methyl alcohol) is the most simple organic alcohol and was first isolated in pure form by Robert Boyle in 1661.[1] Under standard conditions it is a volatile, colorless liquid with an alcohol-like odor and a density of 0.79 g cm⁻³. It can be freely mixed with water, has a boiling point of $T_b = 337.6$ K and freezes at $T_m = 175.6$ K. Until the early 1920s, the most common source of methanol was the pyrolysis of wood and charcoal, yielding roughly 10-20 L methanol per ton of wood.[2] At that time, its application was mainly the usage as lamp oil or other burning fuel. With the development of an industrial feasible production process its importance significantly rose and today methanol is one of the most important basic chemicals with a global demand of more than 65 million tons per year in 2013 and a projected demand of about 100 million tons per year in 2016.[3, 4]

Today, about 80% of methanol are converted into other chemicals, mainly formaldehyde, methyl-*tert*-butylether (MTBE) and acetic acid. A typical product distribution derived from methanol is given in figure 1.1. Formaldehyde and acetic acid are intermediates for commodity products like formaldehyde resins in plywood, methylenebis(4-phenylisocyanate) (MDI) foam in thermal insulators and mattresses or polyvinyl acetate (PVAc) in adhesive applications. MTBE is an organic compound used in upgrading the RON of gasoline. In modern countries it has completely replaced the former commonly used organolead compounds. The remaining 20% are mainly used as solvent or directly as fuel. Especially the latter application is under current investigation and is believed to further increase the methanol demand. As methanol can easily be produced from other carbon sources than oil, the demand for cheap coal derived (China) or shale gas derived (USA) fuel is rising. Until 2016, alone in China the domestic methanol production is

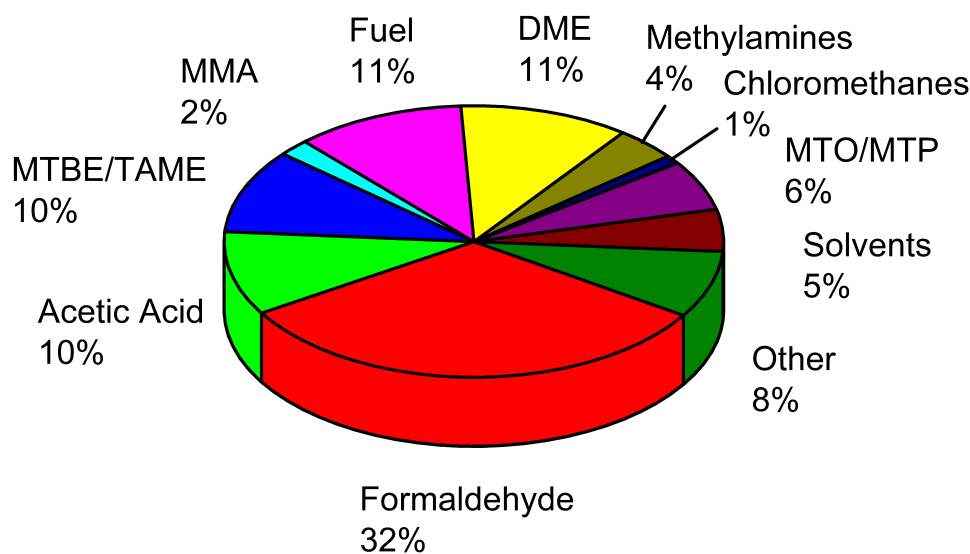


Figure 1.1: Typical distribution of products derived from methanol.[3, 4]

expected to rise by 30 million tons per yer.[5] This also effects other commonly oil-derived compounds like propylene or other olefins. Hence, also a significant rise in methanol to propylene (MTP) and methanol to olefin (MTO) industry is expected.

Although typically produced from natural gas or coal, methanol can be synthesized from a broad feedstock including sustainable sources like biomass, wood or solar derived hydrogen combined with CO_2 from carbon capture and storage sources. In contrast to hydrogen as an energy carrier, the liquid can furthermore be stored, transported, and handled easily. These factors make methanol an interesting candidate for sustainable energy storage, transportation fuel and the long-term replacement of fossil fuels and led to the concept of the "methanol economy".[2]

However, the transition from natural gas to other feedstocks is a challenge for the conventional $\text{Cu}/\text{ZnO}/\text{Al}_2\text{O}_3$ catalysts. In case of CO_2 hydrogenation more active catalytic systems, which can produce methanol at lower temperatures, are needed to effectively circumvent limitations by the thermodynamic equilibrium. In case of coal derived synthesis gas the H_2/CO ratio is typically much lower ($\text{H}_2/\text{CO} \approx 1$) than in synthesis gas from natural gas sources ($\text{H}_2/\text{CO} \approx 2$).[6] These conditions may state new requirements for the industrial catalysts and may also require a revisit of the catalyst stability. Unfortunately, although the current catalysts perform excellent under CO and CO_2 rich conditions, data about the catalyst stability is generally very scarce. Also, no satisfying answers about the deactivation mechanisms or systematic deactivation studies are available in the scientific community.

1.2 Objectives

The aim of this thesis is to establish a general understanding of the deactivation mechanisms in Cu/ZnO/Al₂O₃ catalysts by systematic deactivation of selected model systems, characterization and kinetic modeling of the deactivation process. The content is subdivided into several logically secluded chapters.

- **Chapter 1** gives a short introduction and sketches the general aims of this work.
- **Chapter 2** examines the theoretical background of the methanol synthesis and state-of-the-art knowledge about Cu/ZnO/Al₂O₃ methanol synthesis catalysts.
- **Chapter 3** characterizes the kinetic setups and methods used in this thesis.
- **Chapter 4** presents deactivation studies on five different catalyst samples. The catalysts are systematically aged up to 1600 h time on stream (TOS) and analyzed via TEM, XRD, N₂O-RFC, H₂-TPD, N₂ physisorption and kinetic measurements. Furthermore deactivation mechanisms for different catalyst microstructures are discussed. The chapter will also be submitted for publication in a peer-reviewed journal under the title: "*Deactivation mechanisms on Cu/ZnO/Al₂O₃ methanol synthesis catalysts*".[7]
- **Chapter 5** contains detailed kinetic long term deactivation studies up to 1600 h TOS for three selected catalyst samples and three different aging temperatures. For every system a power law model describing the deactivation behavior is presented. Furthermore, simulations of TEM particle size distributions with Ostwald Ripening models and different collision models are performed to gain insight into the microstructural deactivation process. The chapter will also be submitted for publication in a peer-reviewed journal under the title: "*Kinetics of deactivation on Cu/ZnO/Al₂O₃ methanol synthesis catalysts*".[8]
- **Chapter 6** examines the reactive N₂O frontal chromatography (N₂O-RFC) and temperature programmed H₂ desorption (H₂-TPD) as two methods typically used in characterizing methanol synthesis catalysts in detail. It unravels the relationship between the measured surface area, the metal surface area and oxygen defect sites in the ZnO_x support. The chapter has also been published in a peer-reviewed journal under the title: "*Counting of oxygen defects vs. metal surface sites in methanol synthesis catalysts by different probe molecules*".[9]
- **Chapter 7** analyzes the influence of Al₂O₃ on the temperature programmed desorption behavior of polycrystalline copper. The chapter has also been accepted

for publication in a peer-reviewed journal under the title: "*On the temperature programmed desorption of hydrogen from polycrystalline copper*"[10]

- **Chapter 8** summarizes the results and gives an outlook for possible future research activities.

References

- [1] R. Boyle, *The Sceptical Chymist*, London, **1661**.
- [2] G. A. Olah, A. Goeppert, G. K. S. Prakash, *Beyond Oil and Gas: The Methanol Economy*, Wiley-VCH Verlag GmbH & Co. KGaA, Weinheim, Auflage: 2. vollst. überarb. u. erw. Auflage, **2009**.
- [3] The Methanol Industry, <http://www.methanol.org/Methanol-Basics/The-Methanol-Industry.aspx>, visited: 24.06.2014, **2014**.
- [4] D. Johnson, IHS Inc. Global Methanol Market Review, **2012**.
- [5] C.-J. Yang, R. B. Jackson, *Energy Policy* **2012**, *41*, 878–884, DOI 10.1016/j.enpol.2011.11.037.
- [6] Y. Cao, Z. Gao, J. Jin, H. Zhou, M. Cohron, H. Zhao, H. Liu, W. Pan, *Energy Fuels* **2008**, *22*, 1720–1730, DOI 10.1021/ef7005707.
- [7] M. B. Fichtl, J. Schumann, N. Jacobsen, W. Busser, M. Muhler, M. Behrens, R. Schlögl, O. Hinrichsen, *in preparation*.
- [8] M. B. Fichtl, D. Schlereth, N. Jacobsen, I. Kasatkin, J. Schumann, M. Behrens, R. Schlögl, O. Hinrichsen, *in preparation*.
- [9] M. B. Fichtl, J. Schumann, I. Kasatkin, N. Jacobsen, M. Behrens, R. Schlögl, M. Muhler, O. Hinrichsen, *Angew. Chem. Int. Ed.* **2014**, *53*, 7043–7047, DOI 10.1002/anie.201400575.
- [10] M. B. Fichtl, O. Hinrichsen, *Catal. Lett.* **2014**, *accepted*.

2 Theoretical Background

2.1 General Aspects of Methanol Synthesis

Today, the majority of methanol is produced from fossil resource like natural gas or coal. Despite some promising efforts to find a direct oxidation route of CH_4 to MeOH [1], the industrial process commonly relies on the production of synthesis gas and a downstream hydrogenation of the $\text{CO}/\text{CO}_2/\text{H}_2$ mixture. However, aiming at a more sustainable source of energy, also the hydrogenation of pure CO_2 with (renewable produced) H_2 is under current research.[2–5] The hydrogenation of CO and CO_2 to methanol is in both cases exothermic and accompanied by a decrease of volume:[6]



Both hydrogenations are coupled by the water-gas-shift reaction, which simultaneously occurs on the catalyst.



Although the continuous interconversion of CO and CO_2 complicates mechanistical studies, CO_2 was identified to be the active carbon source in the methanol synthesis over Cu/ZnO . [7–9] Recently Zander et al. [10] showed, that the activity for CO hydrogenation in Cu/MgO systems is much higher than for CO_2 hydrogenation, however this effect is reversed in the presence of ZnO .

In the early 1920s the first methanol synthesis plants were operated using $\text{Zn}/\text{Cr}_2\text{O}_3$ based catalysts. Due to the only moderate catalytic activity, reaction temperatures ranging from 573 to 673 K had to be employed. At these temperatures, high pressure of about 300 bar was needed to shift the methanol equilibrium yield to profitable values. This is illustrated in the equilibrium yield plot in figure 2.1.

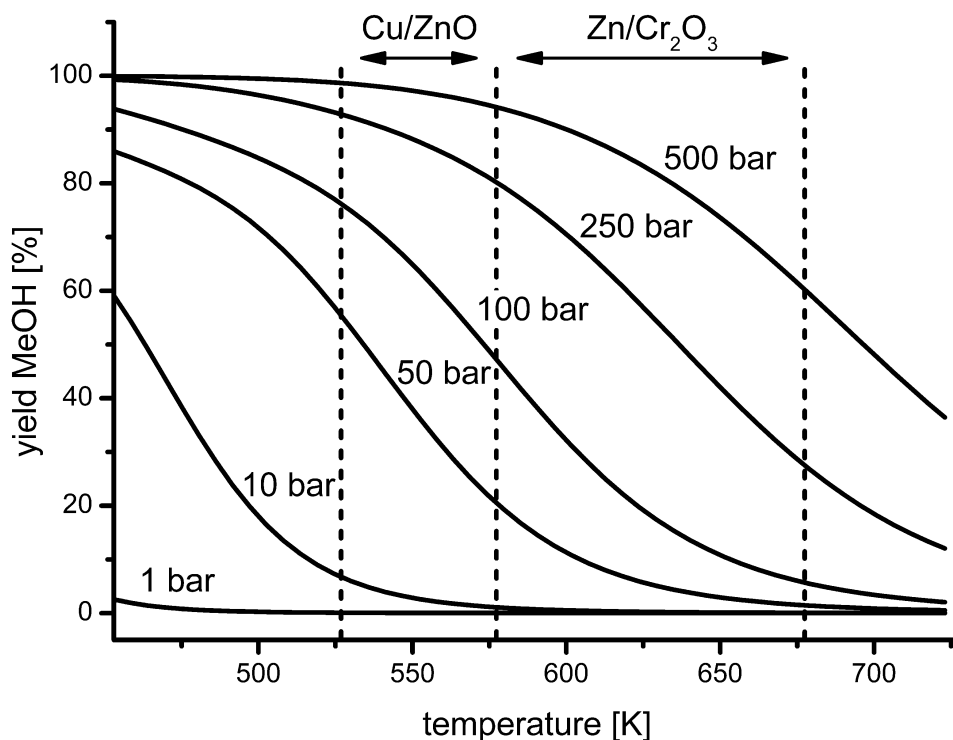


Figure 2.1: Equilibrium MeOH yield as a function of pressure and temperature. Synthesis gas composition: 13.5% CO, 3.5% CO₂, 73.5% H₂, 9.5% N₂.

Although, the high activity of copper based systems was already known in the early 1930s,[11–13] those catalysts were not used until the introduction of the ICI process in 1961.[14] The advantage of the only medium active Zn/Cr₂O₃ systems was their high resistance against catalyst poisons like sulfur, metal carbonyls or halogenides largely present in the formerly coal derived synthesis gas. Whereas the first two substances actively bind to the active metal surface effectively reducing the active sites, the halogenides play an important role in promoting sintering processes. This is described in more detail in section 2.4. With the development of better synthesis gas purification methods, the more sensitive but also much more active copper based catalysts could be employed.[6, 15, 16] Such Cu/ZnO/Al₂O₃ systems are still in use today and the reaction is typically conducted in a temperature region of 523 to 573 K applying pressures ranging from 40 bar to 100 bar.[17]

Apart from the reaction equilibrium, also the exothermicity of the reaction is one of the major design factors of the industrial methanol synthesis concept. Temperature control is a crucial factor in the whole system, as the copper based catalysts are very prone to sintering at elevated temperatures.[16] Typically multi-tubular reactors with

different cooling and heat-recovery processes are employed to efficiently manage the reaction temperature and catalyst activity. One example is the Lurgi MegaMethanol[®] reactor concept with a maximum production capacity of 5000 t methanol per day.[18] The reactor is illustrated in 2.2.

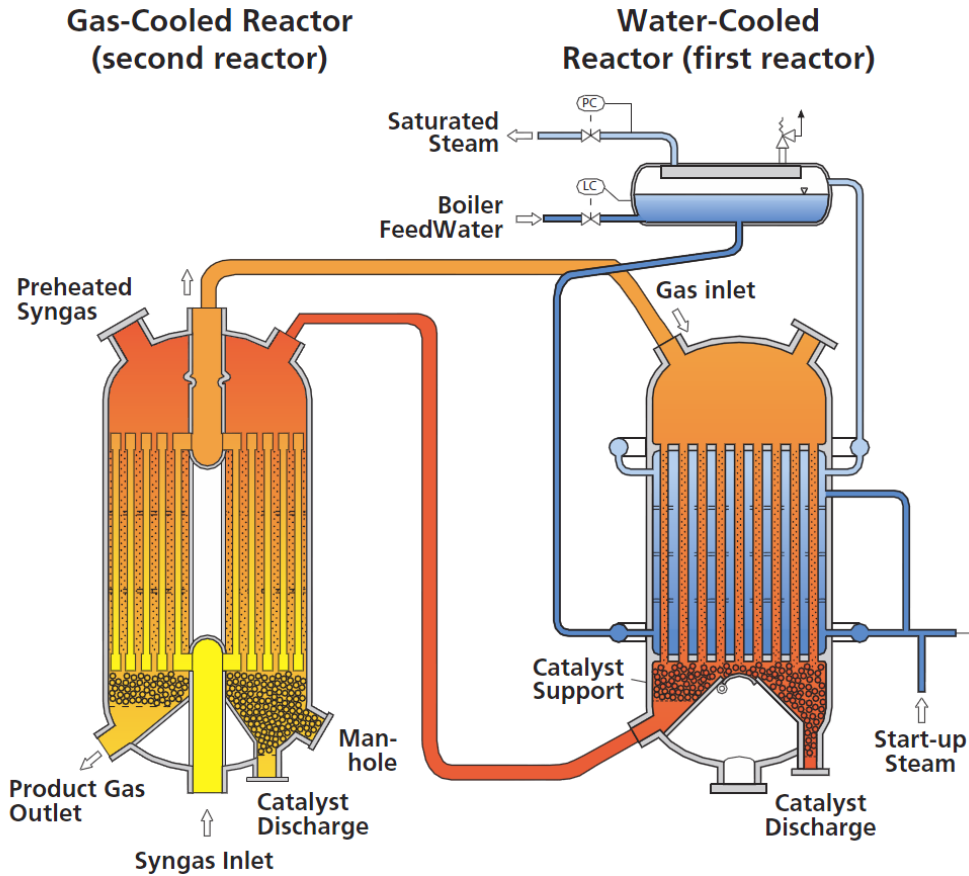


Figure 2.2: Schematic of the Lurgi MegaMethanol[®] methanol reactor concept.[18]

The temperature management is achieved by implementing two separated reaction chambers. The first reactor is a vertical aligned multi-tubular reactor immersed in boiling water with the catalyst sitting inside the tubes. This compartment is operated isothermally and the temperature control is achieved by controlling the exit steam pressure. The methanol containing product gas is led into a second multi-tubular reactor and used in a heat exchanger to preheat the fresh synthesis gas. As the product gas simultaneously cools down, the reaction equilibrium is further shifted to produce more methanol.

2.2 Mechanistic Aspects

The understanding of heterogeneous catalysis and of the function of the individual catalyst components is one of the main goals in technical chemistry and allows the specific design and optimization of catalytic systems. In case of methanol synthesis catalysts, a large amount of model considerations [19–24], microkinetic and mean field approximation models [25–28] and detailed studies containing dynamic changes of the copper crystal morphology are available.[29, 30] However, despite the large effort and huge amount of experimental methods employed, there are still some controversial issues about the basic functioning of the catalyst and the nature of the active site(s) as well as the role of ZnO in the system. The main points of discussion are as follows:

- What is the state of the catalyst and the active site under working conditions?
- What are the most abundant surface intermediates (MASI)?
- What is(are) the rate determining step(s)?
- Is the main carbon source for methanol synthesis CO or CO₂?

Isotope labeling studies and transient experiments show[7–9] that CO₂ seems to be the more important carbon source for the methanol synthesis. Recently, Zander et al. [10] showed that Cu/MgO is a highly active CO hydrogenation catalyst but virtually inert for CO₂ hydrogenation. This behavior is reversed when impregnating the same Cu/MgO catalyst with ZnO and is in line with the assumption of two different routes for CO and CO₂ hydrogenation depending on the presence of ZnO.[31]

Technical improvements and the application of a whole variety of measuring techniques led to the identification of three important and abundant surface intermediates.[32] These are presented in figure 2.3. Typically, the rate determining step in the CO₂-route is assumed to be the hydrogenation of the stable bi- or tridentate formyl species to the methoxy species.

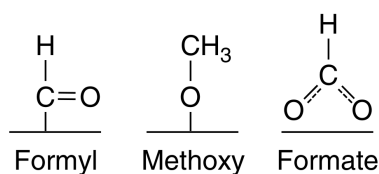


Figure 2.3: Most abundant surface intermediates in copper based methanol synthesis catalysts.

Due to the sheer amount of data available, an exhaustive description of all suggested models and active sites is not constructive within the scope of this work. However, detailed descriptions and reviews are available in literature.[33–37] A brief overview of the main concepts for the reaction mechanism is presented in table 2.1.

Table 2.1: Overview of the different reaction mechanisms and active sites in literature.[32]

Mechanistic concept	References
Cu ⁺ in a ZnO Matrix as the active site	[20, 38–40]
The Schottky Junction theory	[19]
Partially oxidized Cu independent of the support	[41]
Metallic Cu in dynamic interaction with the support	[23, 29, 42, 43]
Cu-Zn surface alloy model	[20, 44, 45]
Copper defect sites decorated with ZnO _x	[24]

2.3 The Industrial Catalyst

Apart from the initially used $\text{ZnO}/\text{Cr}_2\text{O}_3$ and very successful $\text{Cu}/\text{ZnO}/\text{Al}_2\text{O}_3$ systems a variety of other catalysts - mostly also based on copper - has been explored. Typical examples are Raney-type copper/zinc preparation techniques, intermetallic compounds like ThCu_6 or Cu-Ni alloys [46, 47], noble metal systems containing Pt, Ir or Pd [48], or gold on oxide supports like TiO_2 , Fe_2O_3 , or ZnO . [49] Further, rather exotic, examples are sulfide systems like alkaline metal promoted MoS_2 [50, 51] or noble metal sulfides. [52] Also, numerous experiments changing the structural Al_2O_3 support or doping the existing $\text{Cu}/\text{ZnO}/\text{Al}_2\text{O}_3$ system with other elements were performed. [34, 53] However, the original $\text{Cu}/\text{ZnO}/\text{Al}_2\text{O}_3$ system has not been replaced so far, which is attributed to its high activity and excellent methanol selectivity commonly above 99.9%. [32]

Much progress was achieved in the preparation technique of the $\text{Cu}/\text{ZnO}/\text{Al}_2\text{O}_3$ catalysts since the original co-precipitation route was patented by ICI in 1961. [14] Although the exact preparation technique for industrial methanol synthesis catalysts is unknown for obvious reasons, general assumptions and hints can be found in literature. [54, 55] Typically these catalysts are prepared by co-precipitation of the metal nitrate salts with an alkaline precipitation agent, which are commonly carbonates, hydroxycarbonates, or hydroxides. A simplified preparation scheme for $\text{Cu}/\text{ZnO}/\text{Al}_2\text{O}_3$ systems is presented in figure 2.4. [56]

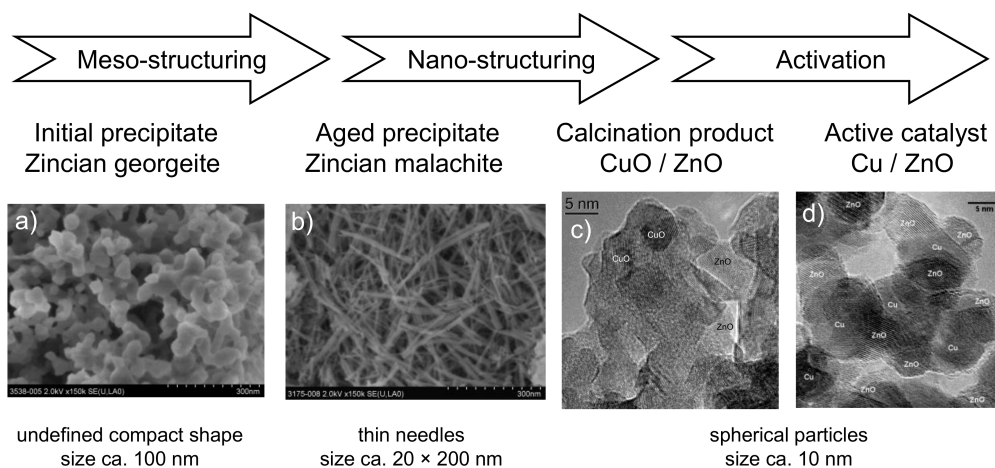


Figure 2.4: Simplified preparation scheme for $\text{Cu}/\text{ZnO}/\text{Al}_2\text{O}_3$ systems and TEM images of the different preparation stages: (a) initial precipitate before aging in the mother liquor (b) formation of thin zinc malachite needles upon aging (c) intimate mixture of CuO and ZnO after calcination (d) reduced nanoparticulate Cu/ZnO catalyst. [56]

The precipitation process is a crucial step in the catalyst synthesis and significantly predetermines the catalytic activity. This behaviour is also often called the "chemical memory" of the catalyst.[57] The complexity of the precipitation process results from various precursor phases, which can be formed during the precipitation process as a function of the pH value, temperature and the mixture composition. An overview of the most important phases found in the precipitate is presented in table 2.2.[32]

Table 2.2: Overview of the most important phases found in a Cu/ZnO/Al₂O₃ precursor.[32]

Chemical Formula	Name
Cu ₂ (OH) ₂ CO ₃	Malachite
Cu ₂ (OH) ₃ NO ₃	Gerhardite
Zn ₅ (OH) ₆ (CO ₃) ₂	Hydrozincite
Zn ₄ (OH) ₆ (CO ₃) · H ₂ O	Zinc hydroxycarbonate
Al(OH) ₃	Aluminium hydroxide
(Cu _x Zn _{1-x}) ₅ (OH) ₆ (CO ₃) ₂	Cu hydrozincite (x < 0.1)
(Cu _x Zn _{1-x}) ₅ (OH) ₆ (CO ₃) ₂	Aurichalcite (0.27 < x < 0.45)
(Cu _{1-x} Zn ₂) ₂ (OH) ₂ CO ₃	Zinc malachite (x < 0.3)
(Cu _{1-x} Zn ₂) ₂ (OH) ₂ CO ₃	Rosasite (0.33 < x < 0.5)
(Cu _x Zn _{1-x}) ₆ Al ₂ (OH) ₆ CO ₃ · 4 H ₂ O	(Cu, Zn, Al) hydroxycarbonate
(Cu _x Zn _{1-x}) ₆ Al ₂ (OH) ₆ CO ₃ · 4 H ₂ O	Roderite

Today, the preparation of Cu/ZnO/Al₂O₃ catalysts is well understood and the occurring processes during the single synthesis steps can be monitored and explained down to the nanoscale. Behrens et al. [58] recently showed that the zinc-malachite is the most active precursor in industrial-like systems and that the catalyst synthesis has been empirically optimized to yield a maximal amount of this phase. Starting from a zinc-malachite type precursor, the active state of the catalyst after reduction in hydrogen is a porous aggregate of intimately mixed spherical copper and ZnO nano-particles of roughly 10 nm in size. Here, the ZnO acts as spacer and structural support, increasing the dispersion of copper.[59] This is illustrated in figure 2.5.

Although the active state of the methanol synthesis catalyst has been thoroughly characterized for years, the concise contributions of the single components Cu, ZnO and Al₂O₃ are still under debate. This is mainly attributed to the fact that the interaction of the single components strongly influences the structure and catalytic behavior of the whole catalyst. Especially ZnO is much more important for the catalytic activity than a simple structural support: it has been shown many times, that the Cu-ZnO interaction also dramatically enhances the intrinsic activity.[20, 23, 61]. In case of Cu/MgO systems

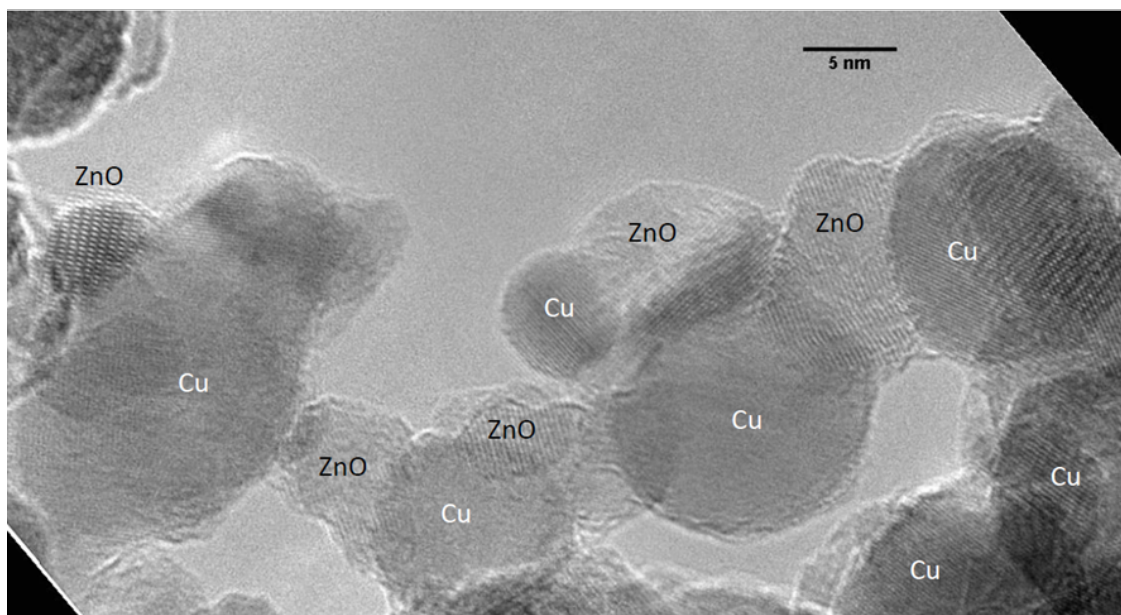


Figure 2.5: HR-TEM image of an activated ex-zinc-malachite catalyst.[60]

an impregnation of a calcined Cu/MgO sample with 5% ZnO resulted in a more than 10-fold increase in methanol yield from CO₂ containing synthesis gas, although the exposed copper surface area measured by N₂O reactive frontal chromatography was not changed significantly.[10] In the active catalyst, the ZnO at the Cu-Zn interface is partially reduced to ZnO_x and forms amorphous layers which cover the copper surface to some extent. This behavior is attributed to the well-known strong metal support interaction (SMSI) of Cu-ZnO.[62–65] The exact structure of the resulting Cu-ZnO interaction is not yet known or - which is more likely - a function of the catalyst environment like temperature, pressure or the gas atmosphere reduction strength. This is also reflected in current literature: on the one hand the quantification of a defined Cu-Zn surface alloy has been recently proposed by Kuld et al. [66], on the other hand Schott et al. [67] showed the existence of a unique δ^+ -polarized ZnO layer structure on copper.

Independent of the particular structure of the Cu/ZnO interaction, Behrens et al. [24] pointed out that the most promising candidate of the active site of the methanol synthesis is a highly defected Cu(0) surface and explained the influence of ZnO using DFT techniques. They elaborated that the incorporation of single Zn atoms into a stepped Cu surface (which is generated due to the mentioned defect structure) increases the adsorption strength of intermediates and reduces activation barriers, hence increasing the catalytic activity.

The strong interaction of the two catalyst components Cu and ZnO is further influenced by the presence of alumina. Although the role of Al₂O₃ has been commonly

accepted as a sole structural support, results from Behrens et al. [68] state that Al_3^+ acts as a dopant in ZnO and poses another interacting factor in Cu/ZnO/ Al_2O_3 systems. In good analogy to Ga doped systems [69], Al_3^+ influences the band structure of ZnO and improves the n-type semiconductivity of ZnO which has a positive effect on the intrinsic activity of Cu(0) and modifies the ZnO defect structure. Summarizing the current literature, a high performance methanol synthesis catalyst is characterized by multiple factors:

- porous microstructure, easily accessible for the gas phase
- high copper surface area stabilized by ZnO and Al_2O_3
- high concentration of defect sites in copper
- homogeneous distribution of ZnO in the catalyst

2.4 Catalyst Deactivation

Catalyst stability is a major issue in methanol synthesis. As already mentioned in section 2.1, the industrial success of the highly active copper based systems was closely connected with improvements in synthesis gas purification methods and the usage of cleaner natural gas as source for synthesis gas generation. Typical poisons are sulfur compounds, the deposition of nickel and iron carbonyls as well as halogenides. Here, the major mechanism is believed to be blocking of active sites by strong chemisorption of the poison compounds on copper.[70–73] Today, natural gas is still the most established source for synthesis gas and the applied reforming processes are highly efficient. A typical two-stage reforming process for the conversion of natural gas into synthesis gas for the methanol production is presented in figure 2.6.[74]

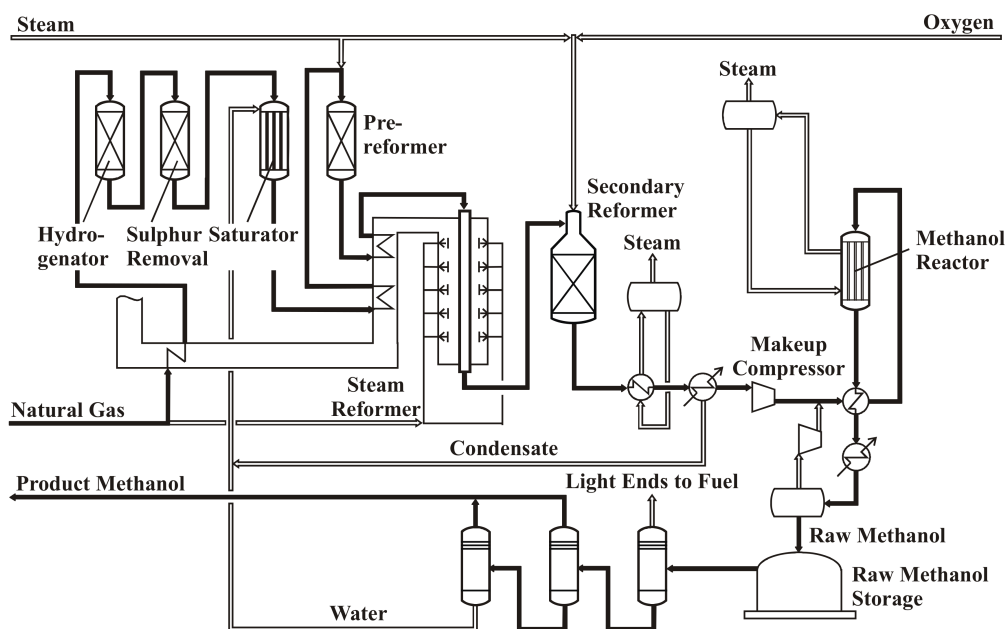


Figure 2.6: Simplified flow diagram for a two-step reforming process and integrated methanol plant.[74]

Nevertheless, as industrial desulfurization and halogenide removal are well implemented processes, poisoning should not be a striking issue in up-to-date methanol plants - independent of the carbon source.[15, 16] Especially in China more than 75% of the current methanol production are based on coal and the rising demand for transportation fuel and DME will further increase this number.[75]

Today, the typical lifetime of industrial methanol synthesis catalysts is limited to several years time on stream.[76] Here, the most prominent deactivation mechanism is believed to be the thermal sintering of the copper particles.[77, 78] Above specific temperature limits single atoms or small clusters start to migrate over the surface, agglomerate and form more stable larger crystallites, which increases the mean particle size and decreases the specific copper surface area. In heterogeneous catalysis the temperature onset for sintering phenomena is usually approximated by the Hüttig and Tammann temperature concepts:

$$T_{Tammann}^i [K] = 0.5 \cdot T_{melt}^i [K] \quad (2.4)$$

$$T_{Hüttig}^i [K] = 0.3 \cdot T_{melt}^i [K] \quad (2.5)$$

Above the Tammann temperature small clusters start to migrate and the whole copper lattice becomes mobile, whereas the migration of single atoms starts at the lower Hüttig temperature. The Tammann and Hüttig temperatures for the single catalyst components as well as for selected copper halides are presented in table 2.3. Taking into account the common temperature range of industrial methanol synthesis plants (523 to 573 K), sintering should only occur on copper. Furthermore, the detrimental effect of halogenides on the catalyst stability can be explained by the very low melting point of these substances and hence also very low Tammann and Hüttig temperatures, which lead to a very pronounced sintering effect.[79, 80] These concepts, however, are only approximations and do not account for stabilizing effects of support structures, metal-support interactions or the influence of adsorbate molecules.

Table 2.3: Tammann and Hüttig temperatures of selected catalyst components and copper halides

Component	T_{melt} [81, 82]	$T_{Tammann}$	$T_{Hüttig}$
Cu	1083 °C	405 °C	179 °C
ZnO	1975 °C	851 °C	476 °C
Al ₂ O ₃	2054 °C	891 °C	502 °C
CuCl	430 °C	78.5 °C	-39 °C
CuBr ₂	498 °C	113 °C	-16 °C

Although catalyst stability is an important design factor for methanol synthesis catalysts, literature about the deactivation mechanisms, deactivation kinetics or even detailed deactivation studies is very scarce and often no common structural development of the catalyst can be deduced: whereas Roberts et al. [72] found an increase of the copper crystallite size, a stable ZnO-particle size and loss in BET surface area, Kung

et al. [16] and Ladebeck [83] also report sintering of ZnO. Also the role of CO is ambivalent. Wu et al. [84] report an increased stability of Cu/ZnO/Al₂O₃ systems which is attributed to a decreased amount of water in the system, whereas Klier et al. and Sun et al. [35, 78] found a faster deactivation under the influence of CO. Many of those differences may rise from the huge variety of Cu/ZnO/Al₂O₃ precursors (see section 2.3) or the susceptibility to formation of Cu-Zn alloys under different reducing conditions and elevated temperatures.[85]

The decrease of catalytic activity $a(TOS)$ by sintering is normally modeled by an empiric power law expression (PLE). As the catalytic activity in some cases levels off at a constant value, these models can further be generalized (general power law model, GPLE) with an asymptotic activity value $a_{eq} > 0$ for an infinite time on stream (TOS). The temperature dependency of the deactivation speed k_d is expressed in an Arrhenius type expression. n is an empiric factor which describes the curvature of the activity plot. Typical values range from 2 to 16.[86]

$$\frac{\delta a}{\delta t} = -k_d (a - a_{eq})^n \quad (2.6)$$

$$k_d = k_0 \cdot e^{\left(\frac{-E_{A,d}}{RT}\right)} \quad (2.7)$$

A summary of power-law deactivation models presented in literature is given in the work of Løvik.[87] It should be noted, that some of these models lack either a detailed characterization, detailed information about the kinetic measurements or are parameterized with data from a large scale reactor without knowing the exact sampling conditions. By extrapolating the long-term behavior of the systems, Løvik found that only two out of seven models are applicable to describe the long-term behavior for more than two years. Prieto et al. [88] recently published a detailed study about methanol synthesis catalyst deactivation and possible methods to stabilize the systems against sintering by separating the nanoparticles using a zeolite pore system. However, even the best catalyst by Prieto et al. [88] is not stable enough to retain more than 10% activity over 400 days, which is much too low for industrial application. An exemplary activity extrapolation over two years is presented in figure 2.7 and illustrates the huge divergence of the kinetic models and the lack of understanding still present.

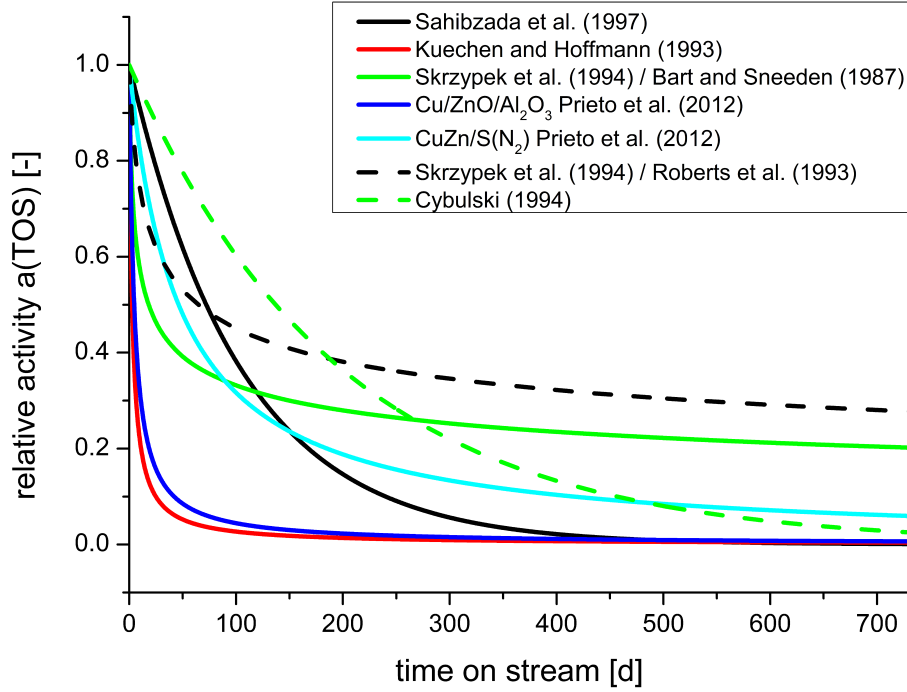


Figure 2.7: Deactivation behavior according to selected literature-known power law models. The solid lines represent gas phase reactions and the dashed lines slurry reactors. Reproduction of data presented in [87] and [88].

Besides the empiric description of catalyst deactivation by (general) power law models, also a mechanistic model was postulated by Rahimpour et al. [89]. According to the authors, methanol is formed by hydrogenation of CO and CO₂ on different active sites and catalyst deactivation is a result of poisoning the CO-hydrogenation centers with CO₂ and vice versa. The governing equations are given in formula 2.8-2.11.

$$r_1 = a_1 \frac{k_{f1} K_{CO} K_H^2 K_{CH} p_{CO} p_{H_2}^2}{1 + K_{CO} p_{CO} + K_{CO} K_H^{\frac{3}{2}} K_{CH} p_{CO} p_{H_2}^{\frac{3}{2}}} \quad (2.8)$$

$$r_2 = a_2 \frac{k_{f2} K_{CO_2} K_H K_{HCO_2} p_{CO_2} p_{H_2}^2}{1 + K_{CO_2} p_{CO_2} + K_{CO_2} K_H^{\frac{1}{2}} K_{HCO_2} p_{CO_2} p_{H_2}^{\frac{1}{2}}} \quad (2.9)$$

$$\frac{\delta a_1}{\delta t} = -a_1^{d1} \frac{k_{d1} p_{CO_2}^2}{1 + K_{CO} p_{CO} + K_{CO} K_H^{\frac{3}{2}} K_{CH} p_{CO} p_{H_2}^{\frac{3}{2}}} \quad (2.10)$$

$$\frac{\delta a_2}{\delta t} = -a_2^{d2} \frac{k_{d2} p_{CO}^2}{1 + K_{CO_2} p_{CO_2} + K_{CO_2} K_H^{\frac{1}{2}} K_{HCO_2} p_{CO_2} p_{H_2}^{\frac{1}{2}}} \quad (2.11)$$

Although the concept offers a mechanistic way to implement the dependency of the deactivation process on the gas atmosphere it has some major disadvantages. Løvik [87] showed that the catalysts described by this model deactivate too fast and are not sufficiently stable for industrial application. Furthermore, the assumption of two different centers for CO_x hydrogenation is not in line with the current mechanistic understanding.[27, 28] Most important, the deactivation by CO_x adsorption should be completely reversible and, in contrast to experimental findings, the model does not account for sintering processes at all.

References

- [1] R. A. Periana, D. J. Taube, S. Gamble, H. Taube, T. Satoh, H. Fujii, *Science* **1998**, *280*, 560–564, DOI 10.1126/science.280.5363.560.
- [2] J. S. Lee, K. H. Lee, S. Y. Lee, Y. G. Kim, *J. Catal.* **1993**, *144*, 414–424, DOI 10.1006/jcat.1993.1342.
- [3] X.-M. Liu, G. Q. Lu, Z.-F. Yan, J. Beltramini, *Ind. Eng. Chem. Res.* **2003**, *42*, 6518–6530, DOI 10.1021/ie020979s.
- [4] Q. Sun, Z. Liu, *Front. Chem. China* **2011**, *6*, 164–172, DOI 10.1007/s11458-011-0250-9.
- [5] F. Arena, K. Barbera, G. Italiano, G. Bonura, L. Spadaro, F. Frusteri, *J. Catal.* **2007**, *249*, 185–194, DOI 10.1016/j.jcat.2007.04.003.
- [6] G. A. Olah, *Angew. Chem. Int. Ed.* **2013**, *52*, 104–107, DOI 10.1002/anie.201204995.
- [7] G. C. Chinchon, P. J. Denny, D. G. Parker, M. S. Spencer, D. A. Whan, *Appl. Catal.* **1987**, *30*, 333–338, DOI 10.1016/S0166-9834(00)84123-8.
- [8] G. Liu, D. Willcox, M. Garland, H. H. Kung, *J. Catal.* **1985**, *96*, 251–260, DOI 10.1016/0021-9517(85)90378-1.
- [9] M. Muhler, E. Törnqvist, L. P. Nielsen, B. S. Clausen, H. Topsøe, *Catal. Lett.* **1994**, *25*, 1–10, DOI 10.1007/BF00815409.
- [10] S. Zander, E. L. Kunkes, M. E. Schuster, J. Schumann, G. Weinberg, D. Teschner, N. Jacobsen, R. Schlögl, M. Behrens, *Angew. Chem. Int. Ed.* **2013**, *52*, 6536–6540, DOI 10.1002/anie.201301419.
- [11] D. S. Cryder, P. K. Frolich, *Ind. Eng. Chem.* **1929**, *21*, 867–871, DOI 10.1021/ie50237a019.
- [12] M. R. Fenske, P. K. Frolich, *Ind. Eng. Chem.* **1929**, *21*, 1052–1055, DOI 10.1021/ie50239a019.
- [13] P. K. Frolich, M. R. Fenske, D. Quiggle, *Ind. Eng. Chem.* **1928**, *20*, 694–698, DOI 10.1021/ie50223a008.
- [14] P. Davies, F.F. Snowdon, G.W. Bridger, D.O. Huges, P.W. Young, UK Patent 1010871, **1961**.
- [15] G. Hochgesand, *Ind. Eng. Chem.* **1970**, *62*, 37–43, DOI 10.1021/ie50727a007.
- [16] H. H. Kung, *Catal. Today* **1992**, *11*, 443–453, DOI 10.1016/0920-5861(92)80037-N.

- [17] M. Baerns, A. Behr, A. Brehm, J. Gmehling, H. Hofmann, U. Onken, A. Renken, K.-O. Hinrichsen, R. Palkovits, *Technische Chemie*, Wiley-VCH Verlag GmbH & Co. KGaA, Weinheim, Auflage: 2. Auflage, **2013**.
- [18] <http://www.lurgi.com>, Lurgi MegaMethanol(R), Stand: 10.06.2014, **2014**.
- [19] J. C. Frost, *Nature* **1988**, *334*, 577–580, DOI 10.1038/334577a0.
- [20] T. Fujitani, M. Saito, Y. Kanai, T. Kakumoto, T. Watanabe, J. Nakamura, T. Uchijima, *Catal. Lett.* **1994**, *25*, 271–276, DOI 10.1007/BF00816307.
- [21] G. C. Chinchin, K. C. Waugh, D. A. Whan, *Appl. Cat.* **1986**, *25*, 101–107, DOI 10.1016/S0166-9834(00)81226-9.
- [22] R. Burch, S. E. Golunski, M. S. Spencer, *Catal. Lett.* **1990**, *5*, 55–60, DOI 10.1007/BF00772093.
- [23] H. Topsøe, C. V. Ovesen, B. S. Clausen, N. Y. Topsøe, P. E. Højlund Nielsen, E. Törnqvist, J. K. Nørskov in *Studies in Surface Science and Catalysis*, (Ed.: G.F. Froment and K.C. Waugh), Dynamics of Surfaces and Reaction Kinetics in Heterogeneous Catalysis Proceedings of the International Symposium, Elsevier, **1997**, pp. 121–139.
- [24] M. Behrens, F. Studt, I. Kasatkin, S. Kühl, M. Hävecker, F. Abild-Pedersen, S. Zander, F. Girgsdies, P. Kurr, B.-L. Kniep, M. Tovar, R. W. Fischer, J. K. Nørskov, R. Schlögl, *Science* **2012**, *336*, 893–897, DOI 10.1126/science.1219831.
- [25] G. Graaf, E. Stamhuis, A. Beenackers, *Chem. Eng. Sci.* **1988**, *43*, 3185–3195, DOI 10.1016/0009-2509(88)85127-3.
- [26] K. M. V. Bussche, G. F. Froment, *J. Catal.* **1996**, *161*, 1–10, DOI 10.1006/jcat.1996.0156.
- [27] T. Askgaard, *J. Catal.* **1995**, *156*, 229–242, DOI 10.1006/jcat.1995.1250.
- [28] L. C. Grabow, M. Mavrikakis, *ACS Catal.* **2011**, *1*, 365–384, DOI 10.1021/cs200055d.
- [29] C. V. Ovesen, P. Stoltze, J. K. Nørskov, C. T. Campbell, *J. Catal.* **1992**, *134*, 445–468.
- [30] M. Peter, M. B. Fichtl, H. Ruland, S. Kaluza, M. Muhler, O. Hinrichsen, *Chem. Eng. Sci.* **2012**, *203*, 480–491, DOI 10.1016/j.ces.2012.06.066.
- [31] B. Denise, R. P. A. Sneed, *Appl. Cat.* **1986**, *28*, 235–239, DOI 10.1016/S0166-9834(00)82507-5.
- [32] *Handbook of Heterogeneous Catalysis: Online*, (Eds.: G. Ertl, H. Knözinger, F. Schüth, J. Weitkamp), Wiley-VCH Verlag GmbH & Co. KGaA, Weinheim, Germany, **2008**.

- [33] J. Bart, R. Sneed, *Catal. Today* **1987**, *2*, 1–124, DOI 10.1016/0920-5861(87)80001-9.
- [34] G. Chinchin, P. Denny, J. Jennings, M. Spencer, K. Waugh, *Appl. Cat.* **1988**, *36*, 1–65, DOI 10.1016/S0166-9834(00)80103-7.
- [35] K. Klier in *Advances in Catalysis, Vol. 31*, (Eds.: D. Eley, H. Pines, P. B. Weisz), Academic Press, **1982**, pp. 243–313.
- [36] H. H. Kung, *Catal. Rev.* **1980**, *22*, 235–259, DOI 10.1080/03602458008066535.
- [37] K. C. Waugh, *Catal. Lett.* **2012**, *142*, 1153–1166, DOI 10.1007/s10562-012-0905-2.
- [38] L. E. Y. Nonneman, V. Ponec, *Catal. Lett.* **1990**, *7*, 213–217, DOI 10.1007/BF00764504.
- [39] G. R. Sheffer, T. S. King, *J. Catal.* **1989**, *116*, 488–497, DOI 10.1016/0021-9517(89)90115-2.
- [40] V. Ponec, *Surf. Sci.* **1992**, *272*, 111–117, DOI 10.1016/0039-6028(92)91427-D.
- [41] M. Bowker, R. A. Hadden, H. Houghton, J. N. K. Hyland, K. C. Waugh, *J. Catal.* **1988**, *109*, 263–273, DOI 10.1016/0021-9517(88)90209-6.
- [42] P. L. Hansen, J. B. Wagner, S. Helveg, J. R. Rostrup-Nielsen, B. S. Clausen, H. Topsøe, *Science* **2002**, *295*, 2053–2055, DOI 10.1126/science.1069325.
- [43] J.-D. Grunwaldt, A. Molenbroek, N.-Y. Topsøe, H. Topsøe, B. S. Clausen, *J. Catal.* **2000**, *194*, 452–460, DOI 10.1006/jcat.2000.2930.
- [44] T. Fujitani, J. Nakamura, *Appl. Cat. A* **2000**, *191*, 111–129, DOI 10.1016/S0926-860X(99)00313-0.
- [45] T. Fujitani, J. Nakamura, *Catal. Lett.* **1998**, *56*, 119–124, DOI 10.1023/A:1019000927366.
- [46] J. Friedrich, M. Wainwright, D. Young, *J. Catal.* **1983**, *80*, 1–13, DOI 10.1016/0021-9517(83)90223-3.
- [47] Q. Wu, W. L. Eriksen, L. D. L. Duchstein, J. M. Christensen, C. D. Damsgaard, J. B. Wagner, B. Temel, J.-D. Grunwaldt, A. D. Jensen, *Catal. Sci. Technol.* **2014**, *4*, 378–386, DOI 10.1039/C3CY00546A.
- [48] M. L. Poutsma, L. F. Elek, P. A. Ibarbia, A. P. Risch, J. A. Rabo, *J. Catal.* **1978**, *52*, 157–168, DOI 10.1016/0021-9517(78)90131-8.
- [49] H. Sakurai, M. Haruta, *Catal. Today*, Second Japan-EC Joint Workshop on the Frontiers of Catalytic Science and Technology for Energy, Environment and Risk Prevention **1996**, *29*, 361–365, DOI 10.1016/0920-5861(95)00305-3.

- [50] H. C. Woo, K. Y. Park, Y. G. Kim, I.-S. Namau, J. S. Chung, J. S. Lee, *Appl. Cat.* **1991**, *75*, 267–280, DOI 10.1016/S0166-9834(00)83136-X.
- [51] J. Zhang, Y. Wang, L. Chang, *Appl. Cat. A* **1995**, *126*, L205–L218, DOI 10.1016/0926-860X(95)00060-7.
- [52] N. Koizumi, K. Murai, T. Ozaki, M. Yamada, *Catal. Today*, Synthesis of Ecological High Quality Transportation Fuels **2004**, *89*, 465–478, DOI 10.1016/j.cattod.2004.02.002.
- [53] G. Chinchin, K. Mansfield, M. Spencer, *Chemtech* **1990**, 692–699.
- [54] M. Twigg, *The Catalyst Handbook*, Manson Publishing Ltd, London, Auflage: 2nd Revised edition, **1996**.
- [55] E. Doesburg, R. Höppener, B. de Koning, X. Xiaoding, J. Scholten in *Preparation of catalysts IV scientific bases for the preparation of heterogeneous catalysts: proceedings of the fourth international symposium; Louvain-la-Neuve, September 1-4, 1986*, (Ed.: B. Delmon, F. Grange, P.A. Jacobs, G. Poncelet), Preparation of Catalysts IV Scientific Bases for the Preparation of Heterogeneous Catalysts, Elsevier, Amsterdam, **1987**, pp. 767–780.
- [56] M. Behrens, *J. Catal.* **2009**, *267*, 24–29.
- [57] B. Bems, M. Schur, A. Dassenoy, H. Junkes, D. Herein, R. Schlögl, *Chem. Eur. J.* **2003**, *9*, 2039–2052, DOI 10.1002/chem.200204122.
- [58] M. Behrens, R. Schlögl, *Z. Anorg. Allg. Chem.* **2013**, *639*, 2683–2695, DOI 10.1002/zaac.201300356.
- [59] M. S. Spencer, *Top. Catal.* **1999**, *8*, 259–266, DOI 10.1023/A:1019181715731.
- [60] M. B. Fichtl, J. Schumann, N. Jacobsen, W. Busser, M. Muhler, M. Behrens, R. Schlögl, O. Hinrichsen, *in preparation*.
- [61] Y. Choi, K. Futagami, T. Fujitani, J. Nakamura, *Appl. Cat. A* **2001**, *208*, 163–167, DOI 10.1016/S0926-860X(00)00712-2.
- [62] J. Nakamura, T. Uchijima, Y. Kanai, T. Fujitani, *Catal. Today* **1996**, *28*, 223–230, DOI 10.1016/0920-5861(95)00240-5.
- [63] S. Polarz, J. Strunk, V. Ischenko, M. W. E. van den Berg, O. Hinrichsen, M. Muhler, M. Driess, *Angew. Chem. Int. Ed* **2006**, *45*, 2965–2969, DOI 10.1002/anie.200503068.
- [64] R. N. d’Alnoncourt, X. Xia, J. Strunk, E. Löffler, O. Hinrichsen, M. Muhler, *Phys. Chem. Chem. Phys.* **2006**, *8*, 1525–1538, DOI 10.1039/B515487A.

- [65] T. Kandemir, F. Girgsdies, T. C. Hansen, K.-D. Liss, I. Kasatkin, E. L. Kunkes, G. Wowsnick, N. Jacobsen, R. Schlögl, M. Behrens, *Angew. Chem. Int. Ed.* **2013**, *52*, 5166–5170, DOI 10.1002/anie.201209539.
- [66] S. Kuld, C. Conradsen, P. G. Moses, I. Chorkendorff, J. Sehested, *Angew. Chem. Int. Ed.* **2014**, *53*, 5941–5945, DOI 10.1002/anie.201311073.
- [67] V. Schott, H. Oberhofer, A. Birkner, M. Xu, Y. Wang, M. Muhler, K. Reuter, C. Wöll, *Angew. Chem. Int. Ed.* **2013**, *52*, 11925–11929, DOI 10.1002/anie.201302315.
- [68] M. Behrens, S. Zander, P. Kurr, N. Jacobsen, J. Senker, G. Koch, T. Ressler, R. W. Fischer, R. Schlögl, *J. Am. Chem. Soc.* **2013**, *135*, 6061–6068, DOI 10.1021/ja310456f.
- [69] R. Wang, A. W. Sleight, D. Cleary, *Chem. Mater.* **1996**, *8*, 433–439, DOI 10.1021/cm950372k.
- [70] C. H. Bartholomew, *Appl. Cat. A* **2001**, *212*, 17–60, DOI 10.1016/S0926-860X(00)00843-7.
- [71] C. T. Campbell, B. E. Koel, *Surf. Sci.* **1987**, *183*, 100–112, DOI 10.1016/S0039-6028(87)80337-0.
- [72] G. W. Roberts, D. M. Brown, T. H. Hsiung, J. J. Lewnard, *Ind. Eng. Chem. Res.* **1993**, *32*, 1610–1621, DOI 10.1021/ie00020a012.
- [73] P. Forzatti, L. Lietti, *Catal. Today* **1999**, *52*, 165–181, DOI 10.1016/S0920-5861(99)00074-7.
- [74] <http://www.topsoe.com>, Large Scale Methanol Production from Natural Gas, Haldor Topsøe, Stand 23.06.2014, **2014**.
- [75] C.-J. Yang, R. B. Jackson, *Energy Policy* **2012**, *41*, 878–884, DOI 10.1016/j.enpol.2011.11.037.
- [76] M. R. Rahimpour, B. Moghtaderi, A. Jahanmiri, N. Rezaie, *Chem. Eng. Technol.* **2005**, *28*, 226–234, DOI 10.1002/ceat.200407062.
- [77] M. Kurtz, H. Wilmer, T. Genger, O. Hinrichsen, M. Muhler, *Catal. Lett.* **2003**, *86*, 77–80–80, DOI 10.1023/A:1022663125977.
- [78] J. T. Sun, I. S. Metcalfe, M. Sahibzada, *Ind. Eng. Chem. Res.* **1999**, *38*, 3868–3872, DOI 10.1021/ie990078s.
- [79] M. V. Twigg, M. S. Spencer, *Appl. Cat. A* **2001**, *212*, 161–174, DOI 10.1016/S0926-860X(00)00854-1.

- [80] M. V. Twigg, M. S. Spencer, *Top. Catal.* **2003**, *22*, 191–203, DOI 10.1023/A:1023567718303.
- [81] G. Brauer, *Handbuch der präparativen anorganischen Chemie, in 3 Bdn.* Enke, **1996**.
- [82] A. F. Holleman, E. Wiberg, *Lehrbuch der Anorganischen Chemie*, Gruyter, Berlin, 102nd ed., **2007**.
- [83] J. Ladebeck, *Hydrocarbon Processing* **1993**, 89–91.
- [84] J. Wu, M. Saito, M. Takeuchi, T. Watanabe, *Appl. Cat. A* **2001**, *218*, 235–240, DOI 10.1016/S0926-860X(01)00650-0.
- [85] T. Kandemir, D. Wallacher, T. Hansen, K.-D. Liss, R. Naumann d’Alnoncourt, R. Schlögl, M. Behrens, *Nuclear Instruments and Methods in Physics Research Section A: Accelerators Spectrometers Detectors and Associated Equipment* **2012**, *673*, 51–55, DOI 10.1016/j.nima.2012.01.019.
- [86] J. Skrzypek, J. Sloczyński, S. Ledakowicz, *Methanol synthesis: science and engineering*, Polish Scientific Publishers, **1994**.
- [87] I. Løvik, PhD thesis, Norwegian University of Science and Technology, **2001**.
- [88] G. Prieto, J. Zečević, H. Friedrich, K. P. de Jong, P. E. de Jongh, *Nature Materials* **2012**, DOI 10.1038/nmat3471.
- [89] M. R. Rahimpour, J. Fathikalajahi, A. Jahanmiri, *Can. J. Chem. Eng.* **1998**, *76*, 753–761, DOI 10.1002/cjce.5450760410.

3 Experimental

3.1 Catalyst Preparation and Characterization

All ZnO-free systems in this work are produced by coprecipitation of the metal nitrates at constant pH and temperature in a stirred tank reactor following the recipes presented in the refs. [1, 2]. All reagents (Na_2CO_3 : Sigma-Aldrich *puriss.*, $\text{Cu}(\text{NO}_3)_2 \cdot 2.5 \text{H}_2\text{O}$: Riedel-de Haën *purum*, $\text{Al}(\text{NO}_3)_3 \cdot 9 \text{H}_2\text{O}$: Sigma-Aldrich *p.a.*) are used without further purification. The experimental setup is illustrated in figure 3.1.



Figure 3.1: Experimental setup for the precipitation of copper catalysts.

In a typical precipitation experiment, the reactor is prefilled with 250 mL bidistilled water and thermally equilibrated for 30 min under constant stirring at 400 RPM. Subsequently, 100 mL of the 1 M metal nitrate solution is dosed into the reactor using a

flow rate of 5 ml min^{-1} . The pH value is measured and controlled by dosing $0.5 \text{ M Na}_2\text{CO}_3$ solution using a calibrated automatic titrator (Metrohm 716 DMS Titrino). The precipitate is aged for 2 h in the mother liquor, filtered off, washed three times with 100 mL bidistilled water, and dried for 12 h at 353 K . After powdering the product in a mortar, the precursor is calcined in synthetic air heating up from RT to 603 K with 1 K min^{-1} and holding for 5 h.

The metal content (Na, K, Cu, Al, Zn) of the calcined precursor is analyzed via ICP/OES (SpectroFlame FTMOA81A, Spectro Analytical Instruments) using a multi element standard (ICP multi element standard solution VIII, VWR) for calibration. 250 mg of the powder is dissolved in 25 mL boiling *aqua regia*, inspissated till dry, and redispersed in 25 mL 1 M HNO_3 . Prior to the analysis, the clear solution is further diluted with 1 M HNO_3 until an approximate metal concentration of 1 mg L^{-1} to 250 mg L^{-1} is acquired.

The mass loss during catalyst activation is determined by TPR-TG-MS measurements. Approximately 20 mg of the calcined sample is placed in a Al_2O_3 crucible and flushed with $Q = 60 \text{ sccm}$ of $10\% \text{ H}_2/\text{Ar}$. Subsequently it is heated up at 1 K min^{-1} from RT to 483 K holding the end temperature for 2 h. An exemplary TPR-TG-MS study is presented in figure 3.2.

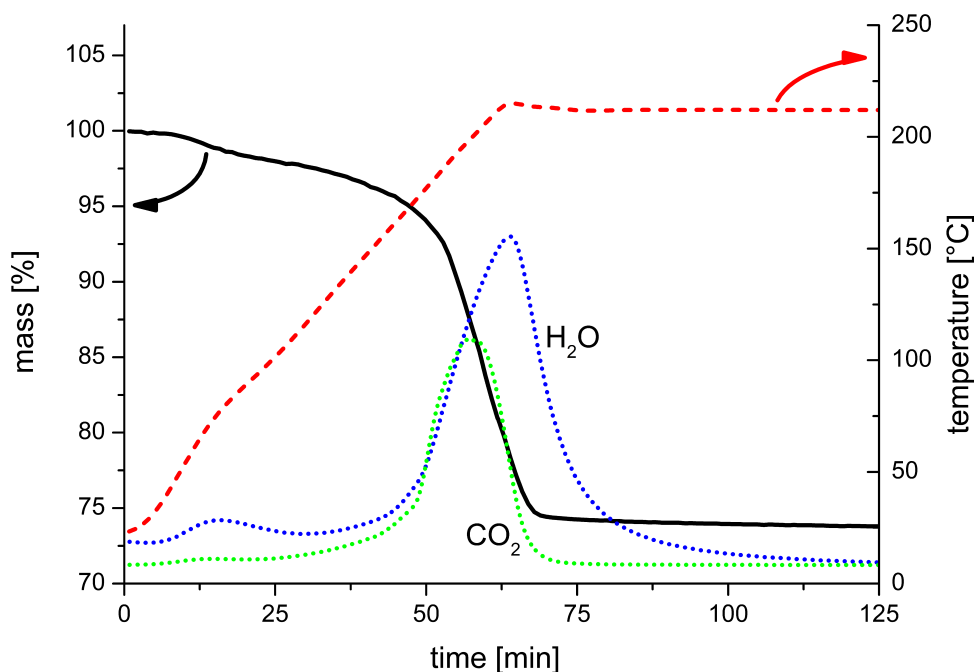


Figure 3.2: Exemplary TPR-TG-MS study of a $\text{Cu/ZnO/Al}_2\text{O}_3$ system. The dotted lines represent the CO_2 and H_2O content in the purge gas atmosphere.

3.2 Setup for Long-term Kinetic Studies

Long-term deactivation studies (TOS > 1000 h) are performed in a single-pass setup equipped with four parallel fixed-bed reactors. Possible reaction temperature range from RT to 773 K and pressures ranging from 1 bar to 60 bar can be applied. Shutoff valves before and after the reactors provide the possibility to remove the catalyst under inert conditions. The whole setup can be heated to 473 K to prevent condensation of liquid reaction products. For each reactor the feed is controlled by one mass flow controller (Brooks 5850TR) with a maximum operating range of 5-500 sccm. The sieved catalyst fraction is placed in 1/2" glass lined steel reactors with a maximum volume of 7 cm³ and secured with silica wool plugs. The flow schema and the setup in working condition are presented in the figures 3.3 and 3.4, the reactors are illustrated in more detail in figure 3.5.

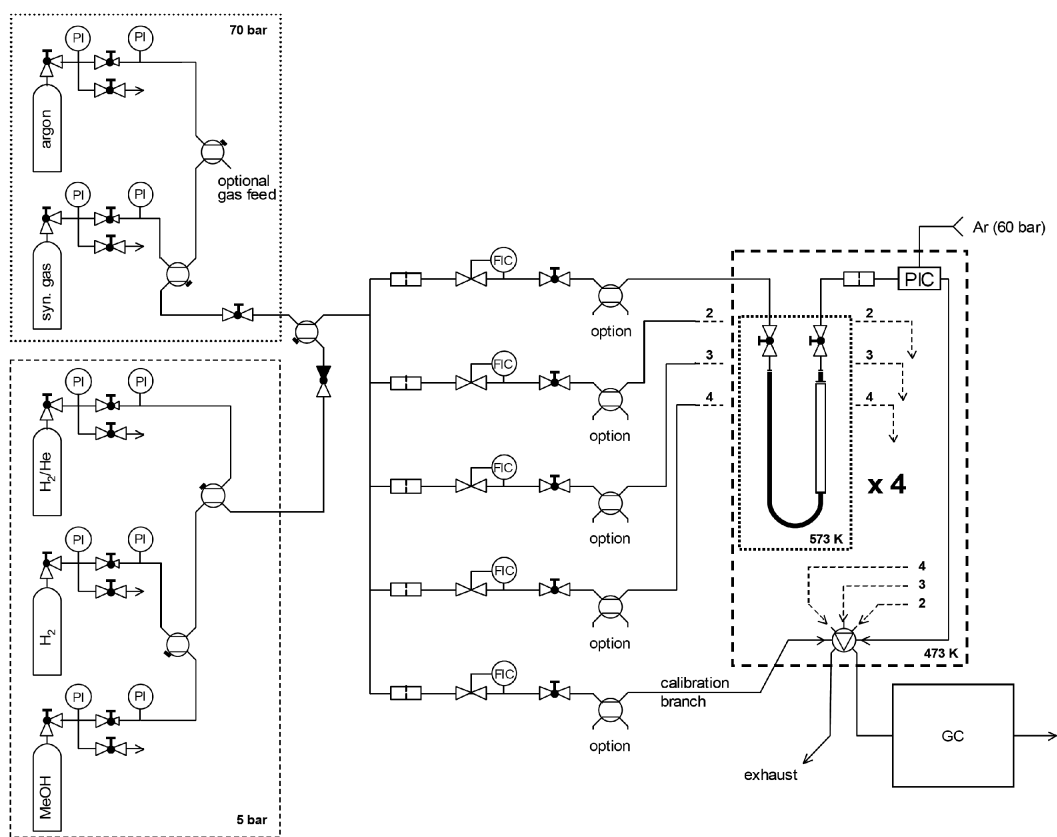


Figure 3.3: Schematic representation of the kinetic setup for long-term deactivation studies.



Figure 3.4: Front view of the final setup for long-term deactivation experiments.

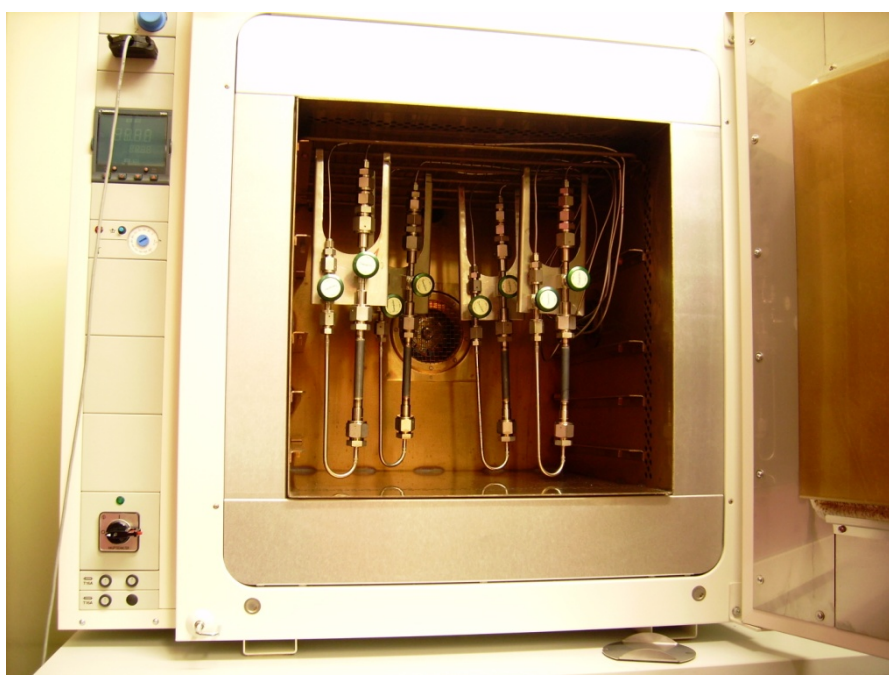


Figure 3.5: View of the four parallel fixed bed reactors in the heating chamber and the attached shutoff valves.

The reaction products are analyzed via gas chromatography (GC, Agilent 7820A) equipped with two thermal conductivity detectors, a packed Porapack N column (\varnothing 3.2 mm, Sigma-Alrich) for separation of CO_2 , H_2O and CH_3OH and a packed molecular sieve 5 Å column (\varnothing 3.2 mm, Sigma-Alrich) for separation of Ar, O_2 , N_2 , H_2 , CH_4 and CO. Furthermore, the setup is connected with a mass spectrometer (Pfeiffer Omnistar GSD 301 O) in order to provide accurate data and the possibility of time-resolved measurements. An exemplary combined GC-MS analysis is presented in figure 3.6.

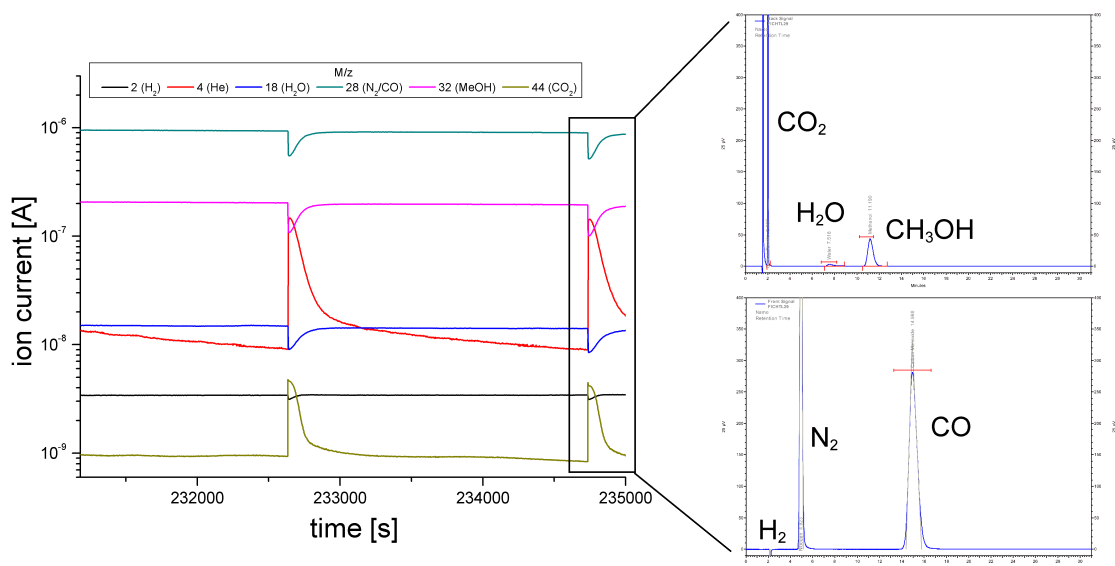


Figure 3.6: Exemplary results of a combined GC-MS measurement.

A detailed description of the specific measurement procedure applied and of the data evaluation methods is given in the respective supporting information of the following chapters.

3.3 Setup for Short-term and Transient Studies

Short-term deactivation studies (TOS < 500 h), kinetic measurements and transient characterizations methods like H₂-TPD are performed in a single-pass setup equipped with one fixed-bed reactor, an upstream water saturator and a gas mixing unit. A flow-scheme is presented in figure 3.7.

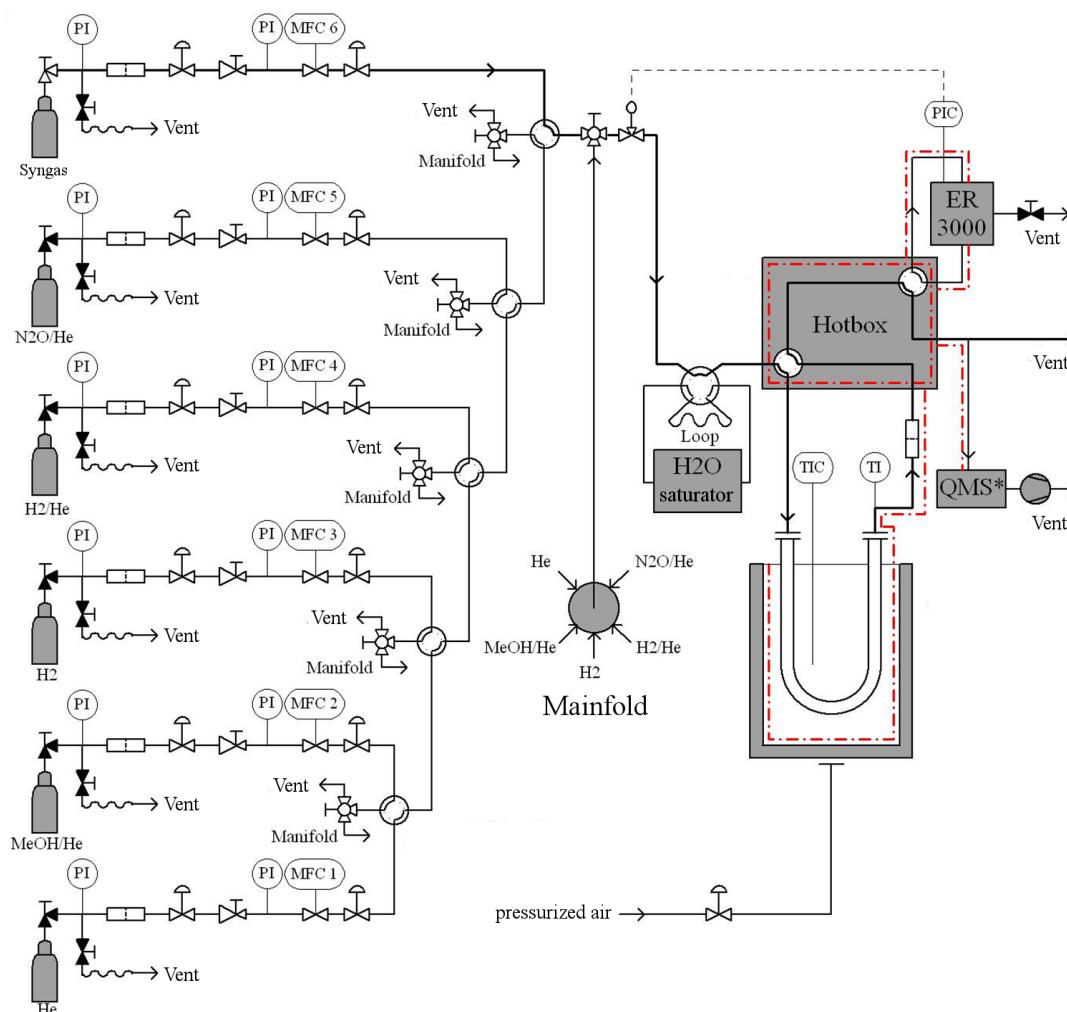


Figure 3.7: Flow scheme of the setup for transient experiments.

In order to enable proper transient experiments, the gas supply unit is designed to have a very small dead volume and virtually no no-flow regions. It can be further equipped with a cooling bath allowing an operation temperature range of 77 to 773 K at a pressure rating of 1 to 28 bar. The catalyst is placed in a 1/4" glass lined tubing, secured with

silica wool plugs and directly contacted with a thermocouple. This is illustrated in figure 3.8.

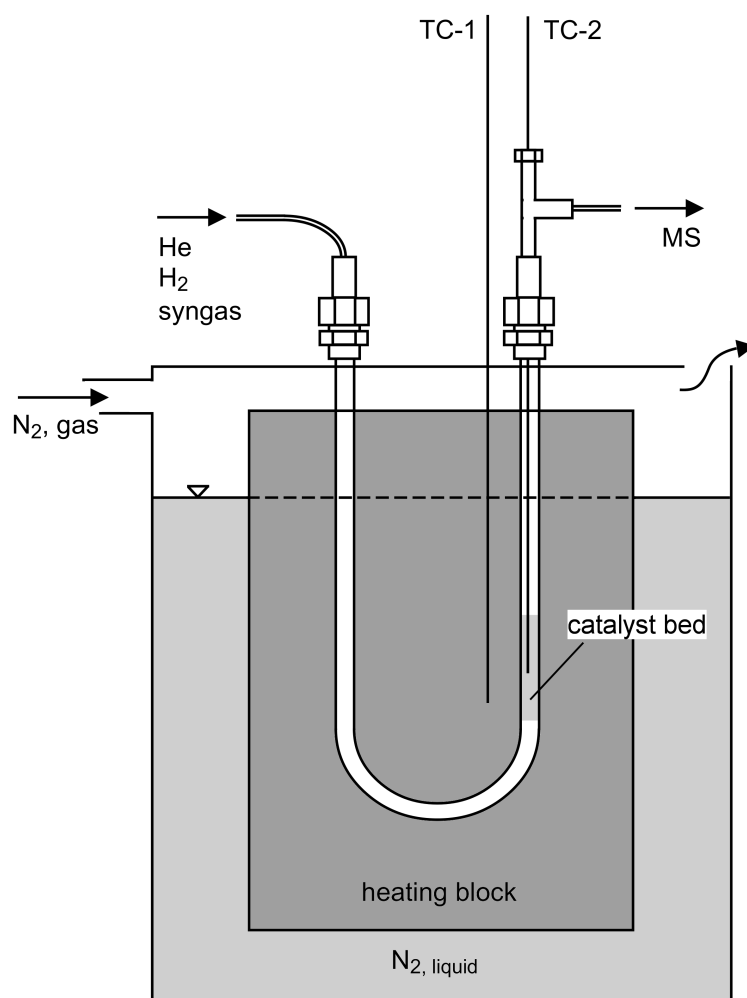


Figure 3.8: Schema of the heating block and attached cooling bath.

Product analysis is performed via the same mass spectrometer and gas chromatograph described in section 3.2. A detailed description of the specific measurement procedure and of the data evaluation methods is given in the respective supporting information of the following chapters.

References

- [1] E. Doesburg, R. Höppener, B. de Koning, X. Xiaoding, J. Scholten in *Preparation of catalysts IV scientific bases for the preparation of heterogeneous catalysts: proceedings of the fourth international symposium; Louvain-la-Neuve, September 1-4, 1986*, (Ed.: B. Delmon, F. Grange, P.A. Jacobs, G. Poncelet), Preparation of Catalysts IV Scientific Bases for the Preparation of Heterogeneous Catalysts, Elsevier, Amsterdam, **1987**, pp. 767–780.
- [2] M. Behrens, R. Schlögl, *Z. Anorg. Allg. Chem.* **2013**, *639*, 2683–2695, DOI 10.1002/zaac.201300356.

4 Deactivation Mechanisms on Cu/ZnO/Al₂O₃ Methanol Synthesis Catalysts

4.1 Abstract

Deactivation of heterogeneous catalysts is an important issue in application-oriented research and majorly defines a catalyst's suitability for plant operation. In case of methanol synthesis catalysts the lifetime is limited; however only few detailed information about catalyst deactivation and structural changes during this process is available. In order to elucidate the basic deactivation mechanisms on ternary Cu/ZnO/Al₂O₃ methanol synthesis catalysts, five different samples with varying performance data and microstructure are prepared, systematically aged and extensively characterized using activity tests, TEM, XRD, BET as well as N₂O and H₂ chemisorption methods. Depending on the particular microstructure, different deactivation mechanisms are found and discussed. It turns out that the presumed classically sintering of copper particles in fact is better described by rigid copper spheres agglomerating upon depletion of the structural spacer ZnO.

4.2 Introduction

Methanol counts among the most important basic chemicals and represents an important C1 building block for industrial chemicals. It offers access to a whole variety of important industrial products, like formaldehyde, dimethyl ether (DME) or methyl-tert-butylether (MTBE) which is used for upgrading of low octane number gasoline. Using methanol to olefins (MTO) or methanol to propylene (MTP) processes, a lot of other important chemical compounds are accessible. Apart from the chemical industry usage, the liquid can also be mixed with gasoline or directly used as fuel for cars. Methanol is commonly produced by hydrogenation of a feed containing carbon monoxide and carbon dioxide. In the typical low-pressure process over Cu/ZnO/Al₂O₃ catalysts pressures ranging from 50 to 100 bar and temperatures of about 483 - 563 K are employed.[1] Since methanol

is a platform molecule and can in general be generated from sustainable hydrogen and CO₂ sources, it gathers rising attention as a renewable energy storage and carrier, which has been proposed and further developed as the "methanol economy" by Olah et al..[2, 3]

Deactivation of heterogeneous catalysts is an ongoing important topic in many industrial fields. Accordingly, catalyst design has been heavily influenced by attempts to create catalytic systems which show high activity and selectivity as well as a high long-term stability. Extensive studies have been performed on almost every high performance catalytic system, giving a variety of recipes how to choose proper process conditions or additives to catalysts in order to stabilize the catalyst activity with time on stream (TOS).[4, 5] In case of methanol synthesis, external factors like poisoning of the catalysts were early identified as an important problem and in fact the early usage of copper based catalysts was limited by the insufficient removal of sulfur from coal-derived synthesis gas.[6] Other typical poisons are the deposition of nickel and iron carbonyls as well as halogenides. The latter ones - in particular chloride - play a special role in copper catalyst deactivation, as they do not actively block copper sites, but greatly enhance the sintering tendency of the metal by forming volatile CuCl and CuCl₂. [6, 7] Nevertheless, as industrial desulfurization and halogenide removal are well implemented processes, poisoning should not be a striking issue in today's methanol plants.[8, 9] However, intrinsic deactivation - processes like sintering or segregation - plays still an important role in the methanol synthesis.[10] To our knowledge, for the methanol synthesis on copper-based catalysts under industrial-type conditions no microstructural deactivation mechanism, systematic long-term study or even detailed long-term measurements combined with characterization can be found in literature. The scarce information about deactivation mechanisms is insofar remarkable, as even today - 50 years after the commercial introduction of the Cu/ZnO/Al₂O₃ system - the nature of the active site(s) of methanol synthesis is still under discussion and a huge variety of experimental techniques is employed to elaborate the interplay of the different catalyst components.[11–13] The high complexity of the ternary system - including dynamic morphologic changes of copper [14–16], evident influence of particle strain and stress [13, 17] and a synergistic SMSI-effect [18–20] as well as the decoration of copper particles with mobile ZnO_x species [13, 21] - gives rise to a huge amount of possible deactivation pathways. For copper based catalysts sintering is often described as one of the main reason for intrinsic catalyst deactivation and detailed mechanisms employing kinetic models like Ostwald ripening or particle migration are still under investigation.[6, 7, 22–24]

In this contribution systematic long-term deactivation studies on five Cu/ZnO/Al₂O₃ catalysts combined with a time dependent in-detail analysis of the deactivated systems

are performed and evaluated in order to shed light on probable deactivation mechanisms.

4.3 Experimental

4.3.1 Catalyst Preparation

Recently the strong correlation of catalytic activity and preparation technique in methanol synthesis and the resulting general concept of Cu/ZnO based high performance catalysts has been reviewed in detail.[25] In order to study the microstructural effect on the catalytic activity and deactivation behavior five different high-performance catalysts are prepared according to literature techniques. CZA1 is a reproduction of a catalyst described in previous work and detailed characterization data can be found therein.[26, 27] CZA2 and CZA3 are prepared via a typical coprecipitation method of the metal nitrate solutions at pH = 7 according to ref. [28] and in case of CZA4 and CZA5 a consecutive approach analogous to ref. [29] is employed. In the latter case CZA4 is prepared by combining the precipitate solution of Zn/Al with the precipitate solution of Cu whereas in case of CZA5 alumina is precipitated and combined with a precipitate solution of Cu/Zn.

Table 4.1 gives an overview of the systems employed and selected characterization results. It should be noted that the BET and N₂O-RFC surface areas are based on the mass of activated catalyst; hence the values are higher than reported in the corresponding literature, where typically the calcined mass is used for normalization.

Table 4.1: Metal ratio and properties of the synthesized catalysts.

Catalyst	Cu:Zn:Al ^[a] [%]	SA _{BET} ^[b] [m ² g _{cat} ⁻¹]	SA _{RFC} ^[b,c] [m ² g _{cat} ⁻¹]
CZA1	70:28:2	93.1	50.9
CZA2	58:26:16	86.2	29.5
CZA3	43:49:8	77.7	22.5
CZA4	55:24:20	113.9	34.8
CZA5	58:25:16	115.2	43.7

[a] molar, determined by EDX and XRF [b] activated catalyst [c] error $\pm 1\text{m}^2\text{g}_{\text{cat}}^{-1}$

4.3.2 Deactivation and Kinetic Experiments

The catalysts are aged on a single pass setup with four parallel fixed bed reactors which can be operated up to 70 bar and temperatures up to 773 K. The catalyst bed is placed in glass lined steel tubing (diameter 1/2 inch, maximum length 3 inch) and secured with silica wool plugs. Shutoff valves permit the removal of the catalyst under inert conditions. The analysis of the reaction products is performed with an Agilent 7820A gas chromatograph equipped with two thermal conductivity detectors, a packed Porapack-N column (Sigma Aldrich) for the quantification of CH₄, CO₂, H₂O, CH₂O, CH₃OH and a packed Molsieve 5 Å column (Sigma Aldrich) for the quantification of Ar, N₂, CH₄ and CO. If not reported otherwise, all gas purities are of very high grade (6.0 for Ar, H₂, N₂, 5.5 for CO₂, 5.0 for N₂O, 4.7 for CO) and have been checked for sulfur impurities below 100 ppb. A trap containing 10 g activated methanol synthesis catalyst at room temperature serves as additional guard reactor for traces of sulfur and metal carbonyls.

In a typical measurement 1000 mg calcined catalyst (m_{calc} , sieve fraction 500-710 μm) is heated up for 15 hours in 2.0% H₂ in Argon raising the temperature from 300 to 448 K at 1 K min⁻¹, then in H₂ raising the temperature from 448 to 513 K at 1 K min⁻¹ and holding for 30 minutes. After activation the catalyst is aged in a mixture of 13.5% CO, 3.5% CO₂, 73.5% H₂ and 9.5% N₂ at 60 bar pressure, a temperature of 523 K and a weight hourly space velocity (WHSV, $\frac{m_{\text{feed}}}{m_{\text{calc}}}$) of 0.51 h⁻¹. Under these conditions, all evaluated catalysts reach equilibrium constitution and are aged under the same atmosphere, which is confirmed by the product analysis. Also, no formation of a hotspot is observed. It should be noted that these conditions were specifically chosen to ensure a fast and reproducible deactivation by stressing the catalysts under high conversions. These conditions do not represent the gas phase composition which is typically present in the majority of the catalyst bed in an industrial reactor. Due to the large reactor cross section of 1/2 inch and the low volume flow at aging conditions, the catalyst is aged with only minor local concentration gradients along the catalyst bed ensuring homogeneous deactivation over the catalyst bed length. After 240, 480, 720 or 960 hours time on stream (TOS) respectively the reactors are depressurized and flushed with argon for 60 minutes. One reactor is removed from the oven and transferred under argon into a glovebox for further analysis whereas the remaining samples are reheated and further aged.

Careful analysis prior to the deactivation measurements showed that at aging conditions no pore diffusion limitation is present, but formation of a hotspot at high WHSVs and temperatures above 473 K may lead to inaccurate results. As diluting the catalyst with inert material interferes with the sample post processing steps, aging the catalysts for analysis - which demands a high amount of non-diluted catalyst sample - and detailed kinetic characterization of the aging process are split up into two different measurements

using the same aging conditions. In the kinetic measurements the catalyst is furthermore diluted with six mass equivalents of purified SiC of the sieve fraction 355–500 μm. The catalytic activity is measured at a temperature of 483 K, and a pressure of 60 bar under differential conditions. Due to the long aging periods and the high amount of synthesis gas needed for the measurement only three selected catalysts CZA1, CZA2 & CZA3 are analyzed at aging times corresponding to the ex situ analysis.

4.4 Catalyst Characterization

4.4.1 Transmission electron spectroscopy (TEM, TEM-EDX)

The aged samples are transferred under inert atmosphere into the glovebox, where the TEM grid was prepared. The specimen is brought to the microscope using a vacuum transfer holder. For the determination of the particle size distribution (PSD) images were recorded using a Philips CM200FEG microscope at 200 kV with a magnification of 72.000. Around 2000 or more particles were evaluated for each PSD. HR-TEM images were recorded for a more detailed view of certain areas.

4.4.2 X-ray Diffraction (XRD)

The aged samples are carefully powdered in the glovebox and loaded for further analysis into glass capillaries and sealed. Powder XRD patterns were recorded in capillary mode on a STOE STAD P diffractometer with a primary focusing Ge monochromator (Cu K_{α1} radiation) and a linear position sensitive detector. The full diffraction patterns were analyzed using the TOPAS software.[30]

4.4.3 Reactive N₂O Frontal Chromatography (N₂O-RFC)

The ex situ measured active copper surface area is determined by reactive frontal chromatography using a well established method described in ref. [31] in a setup described in ref. [32]. In a typical measurement 100 mg activated catalyst (m_{cat}) at 308 K, 1 bar pressure and a flow rate of 10 sccm N₂O (1%) in Ar are used. Prior to the measurement, the aged catalysts are transferred from the glovebox to the measuring setup under inert conditions and reduced for 1 h at 513 K in 4.5% H₂ in Argon. Due to the unavoidable subsurface oxidation of copper during the RFC experiment, an error margin of $1 \text{ m}^2 \text{ g}_{\text{cat}}^{-1}$ is assumed, which is higher than the actual measured error when reproducing the experiments. By comparing these values with in situ measurements that were done using a mass spectrometer on the aging setup it was ensured that the transfer process does not bias the results.

4.4.4 Nitrogen Physisorption

Samples were handled in the glove box and transferred under Ar. Static nitrogen physisorption experiments were performed at the boiling point of liquid N₂ subsequent to outgassing at 473 K (2 hours) in a Belsorp-max (Bel Japan, Inc.) setup. Data were analyzed according to the BET equation assuming that the area covered by one

N₂ molecule is 0.162 nm². The pore size distribution was obtained applying the BJH equation.

4.4.5 H₂-TPD Measurements (H₂-TPD)

The H₂-TPD experiments are performed with the aged catalyst samples which are generated during the kinetic experiments. Roughly 100 mg of the active catalyst are loaded into a glass lined steel reactor and transferred to the measurement setup described in ref.[33]. Prior to the TPD experiments the copper surface area is determined via N₂O-RFC and compared with data gathered during the aging procedure without catalyst dilution to check for errors during the transfer process. Afterwards, the catalyst is reactivated by heating it up to 523 K at 2 K min⁻¹ in 2% H₂/He. The TPD measurement follows a procedure described in ref. [34]. After the activation procedure, the catalyst is cooled down in He to 235 K and pressurized for 30 minutes with 24 bar of H₂. After the adsorption period the catalyst is rapidly cooled down to 77 K, depressurized to 1 bar and flushed with He for another 30 minutes until the H₂ baseline in the mass spectrometer is stable. The H₂-TPD experiment is conducted at 1 bar using a He flow rate of 100 sccm and heating rates β of 4, 6 and 10 K min⁻¹. The amount of hydrogen is calculated using the complete area under the desorption peak in the temperature region between 200 and 350 K.

In case of CZA2 also the effect of an oxidative treatment is analyzed: Subsequent to the TPD measurements, the activity is measured under differential conditions at 24 bar synthesis gas of the same composition as in the aging process, and temperatures ranging from 453 up to 523 K. Then the catalyst is cooled down in He to 110 K, flushed with 2% O₂/He and reheated to 673 K at 6 K min⁻¹. Due to the low temperature a very steady and modest O₂ consumption is visible in the mass spectrum which confirms a mild oxidation process. Afterwards the catalyst is reactivated using the program described in section 4.3.2 and again characterized via H₂-TPD, N₂O-RFC and activity measurements.

4.5 Results

4.5.1 Activity and Copper Surface Area

The active copper surface area according to N₂O-RFC and catalyst activity with TOS is given in figure 4.1 and table 4.4. All samples exhibit a high activity for methanol synthesis and a copper surface area which compares well with other published Cu/ZnO/Al₂O₃ systems.[35, 36] It should be noted that the presented N₂O-RFC data is based on activated catalyst samples and therefore roughly 20% higher than data based on the calcined sample before activation. As given in figure 4.1, the CZA1 system exhibits the highest activity which can be explained by an optimal incorporation of Al³⁺ ions in ZnO. The resulting increase in activity and in ZnO_x defect sites has been reported in literature.[26] The lower activity of CZA3 compared to the equally prepared CZA2 is consistent with the lower copper content and corresponding high Zn content which are both beyond the typical composition of industrial relevance (Cu:Zn ≈ 70:30).[37]

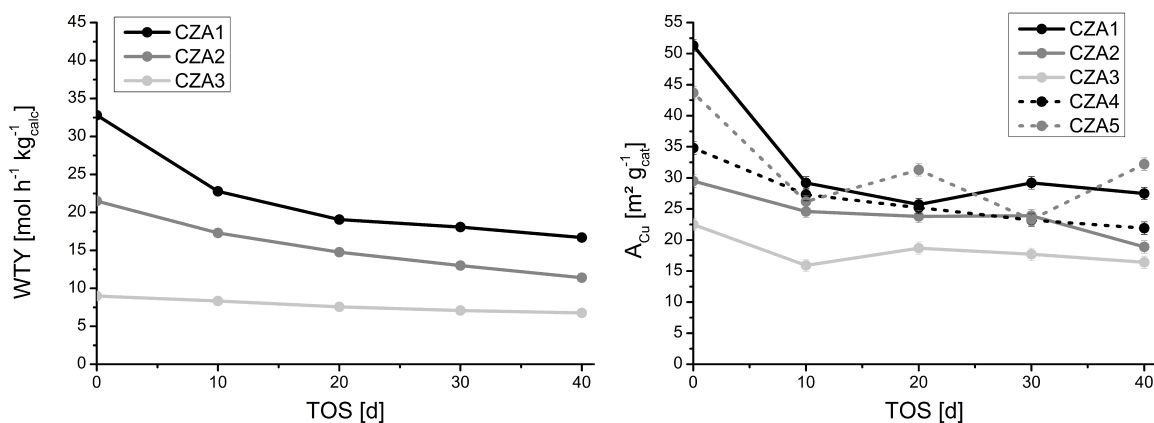


Figure 4.1: Catalyst activity of CZA1, CZA2 and CZA3 as a function of TOS (left) and corresponding specific copper surface area (right).

CZA1 and CZA2 exhibit a comparable apparent deactivation behavior and lose about 40% of the initial activity during the 40 day aging period whereas CZA3 only loses roughly 25%. This strong deactivation is attributed to the highly stressing conditions chosen for the aging periods. In all measurements the catalyst selectivity is beyond 99% over the whole lifetime and all mass balances are closed within 2% relative accuracy. In case of the highly active CZA1, traces of methane are observed during the aging periods.

In all cases the conversion of CO_x is below 15% of the corresponding equilibrium conversion which allows the assumption of differential measurement conditions. Measurements at lower temperatures and hence more differential conditions yield essentially

the same results, however the conversion of the low activity sample CZA3 is then too low for a proper activity evaluation. The relative catalyst activity a_{rel} as a function of the aging time is defined by the ratio of the WTY at a specific aging time and the initial catalyst activity.

$$a_{rel}(TOS) = \frac{WTY(t = TOS)}{WTY(t = 0)} \quad (4.1)$$

4.5.2 Transmission Electron Spectroscopy

High resolution transmission electron spectroscopy (HR-TEM) has proven to be a very important tool to analyze the microstructure of methanol synthesis catalysts and has been applied successfully in many studies.[13, 25, 38] In this study HR-TEM is applied to characterize the catalysts' microstructural composition and to discriminate between different aging processes within the different catalyst phases. The catalysts microstructural homogeneity is mainly controlled by the precipitation process which is known to generate a "chemical memory" and has a large effect on the resulting activity.[25, 39]

The local structure is mainly characterized by the Cu/Zn/Al metal ion ratio which can be ascribed to the prevalent precursor phases zinc malachite $(Cu,Zn)_2(OH)_2(CO_3)_2$, aurichalcite $(Cu,Zn)_5(CO_3)_2(OH)_6$, hydrotalcite $((Cu,Zn)_{1-x}Al_x)(OH)_2(CO_3)_{x/2}$ and single components like amorphous Al_2O_3 . Using TEM-EDX measurements it is possible to assign characteristic microstructural compositions to different precursor phases.[40] This is illustrated in figure 4.2.

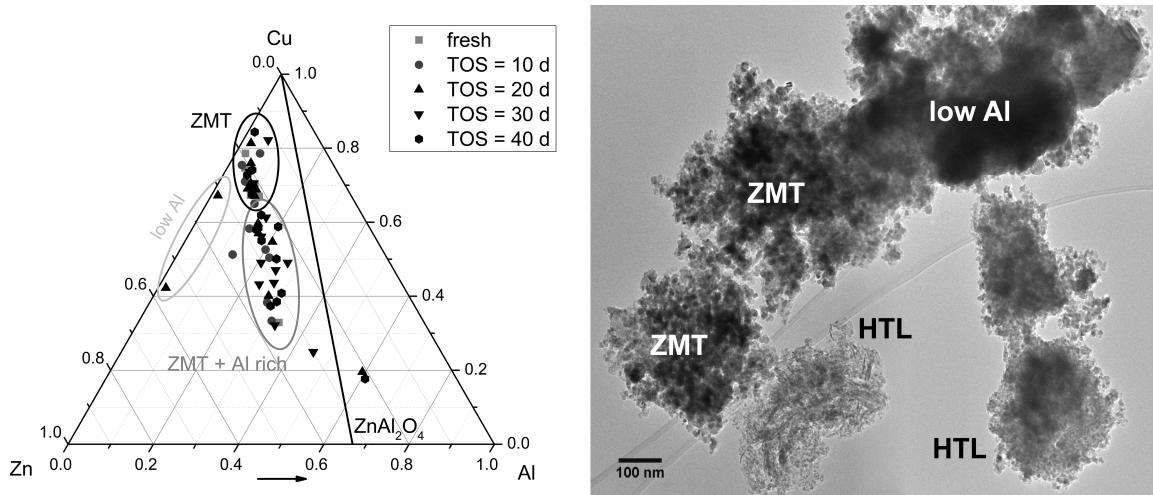


Figure 4.2: (left)EDX-results of the local composition of CZA2 during the aging period and an exemplary TEM image of the correlating microstructure (right).

As confirmed with the TEM-EDX measurements, the prevalent structural feature in these systems is an inhomogeneous mixture of ex-zinc-malachite type (ZMT) which is characterized by a high copper content, and a smaller amount of alumina rich ex-hydrotaalcite-like (HTL) phases. Also small amounts of low aluminum regions with large copper particles can be found. In case of CZA1 no HTL phase is present, which is a result of the low aluminum content of the precursor.[26] As an exception the sample CZA3 only exhibits a narrow ex-aurichalcite phase composition which is characterized by a lower copper/zinc ratio. This can be attributed to the increased Zn content in the catalyst precursor.

An analysis of the aged catalysts reveals that although the macroscopic composition stays constant during the deactivation period, a systematic trend for the sintering behavior of copper particles can be observed in the governing ZMT and HTL phases. This is depicted in figure 4.3.

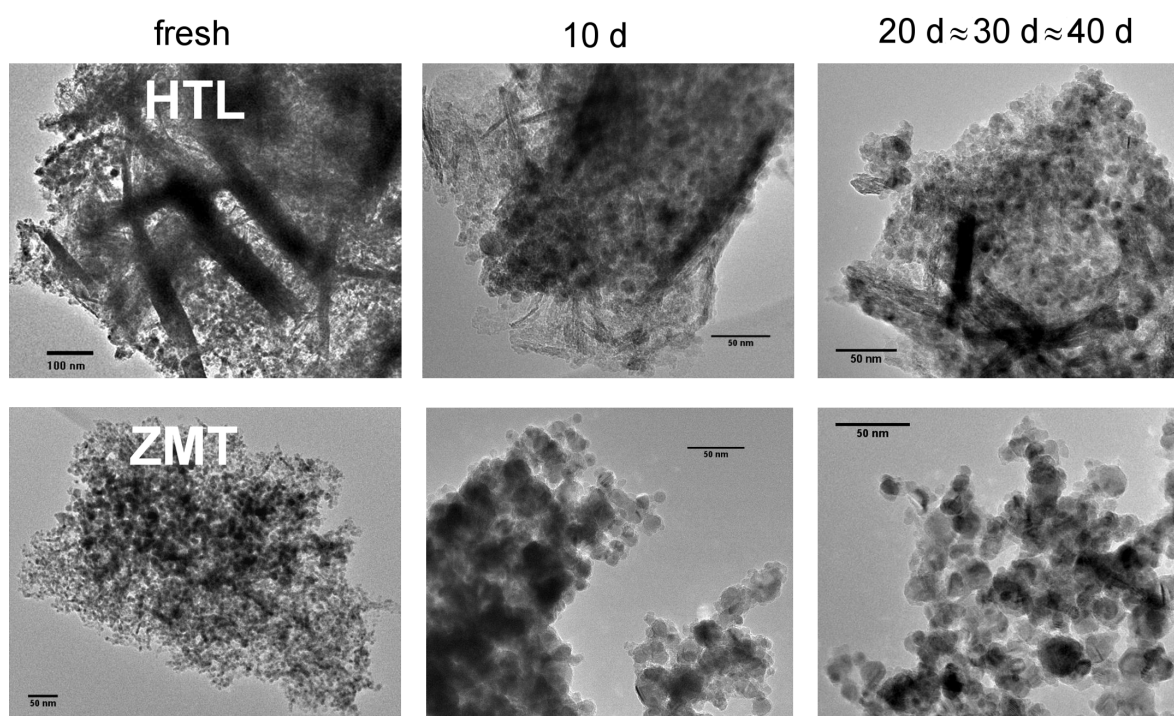


Figure 4.3: Deactivation behavior of Cu Particles in the governing HTL and ZMT phases.

In the alumina rich HTL structure the copper particles are embedded in a compact matrix of zinc alumina spinel and amorphous oxides. This stable matrix keeps the particles well apart so that they show no sintering behavior during the whole deactivation period of 40 days. However, these particles are not accessible very well and are expected to exhibit only a small specific surface area.[40]

The alumina depleted ZMT phases are characterized by an open microstructure where copper particles are partially covered with ZnO_x species and kept apart by ZnO (see figure 4.4). During the aging process sintering of the copper particles is observed and new twinning sites are generated due to particle contact. Furthermore, the formation of a crystalline zinc alumina spinel phase as well as γ -Al₂O₃ and an amorphous overlay over some of the copper particles is observed. Figure 4.4 gives an overview of the different coexisting ZMT and HTL regions and underlines the changes during the aging process.

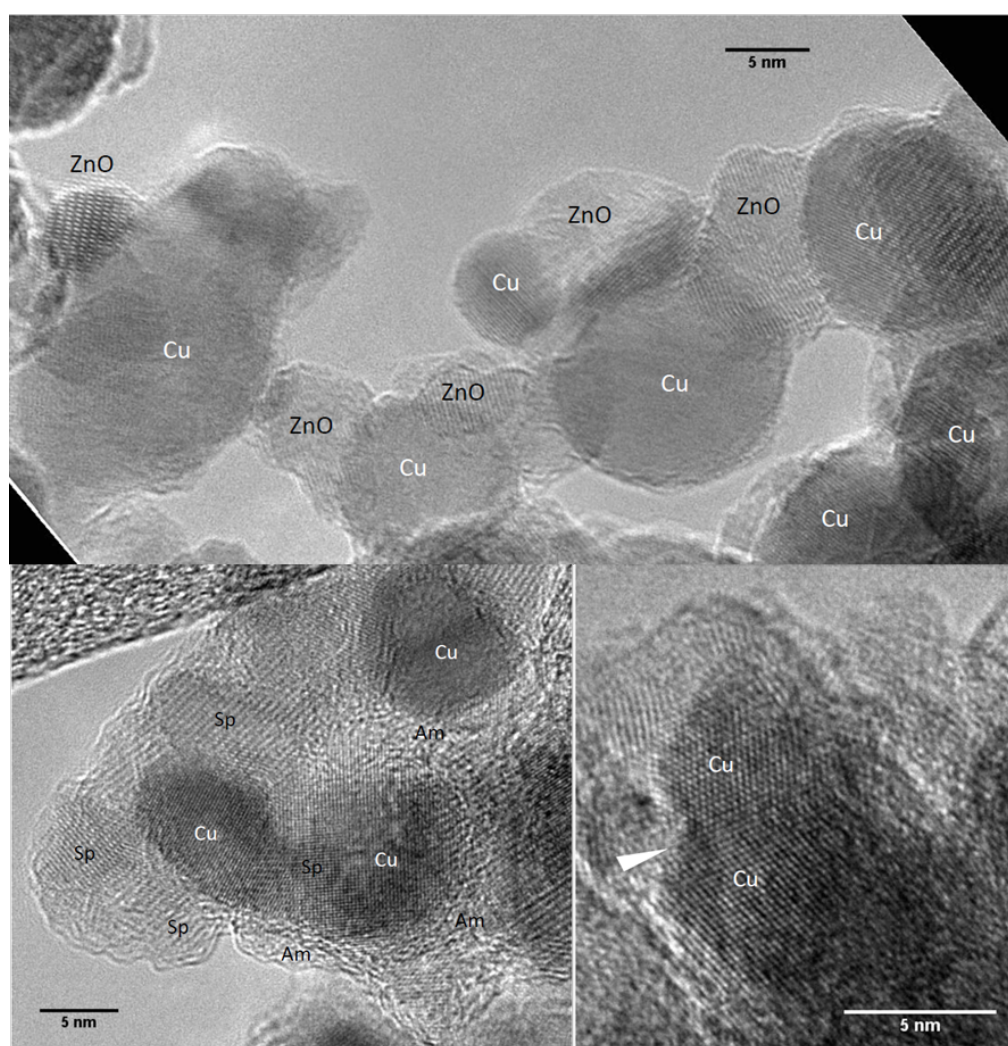


Figure 4.4: Top: Porous microstructure of the ZMT phase in the activated catalysts. Bottom: Embedding of copper particles in a partially amorphous ZnAl₂O₄ ("Sp") matrix in the HTL phase (left) and formation of new twinning boundaries at the grain boundary of contacting particles (right).

The copper particle size distribution of all catalyst samples is given in Table 4.7 and Figure 4.11 in the appendix shedding light on the different sintering behavior of the catalysts. CZA1, CZA2 and CZA5 are very prone for sintering of the copper particles and the mean particle diameter as well as the width of the particle size distribution increase during the aging process. This process slows down after roughly 30 days. In contrast, CZA3 and CZA4 exhibit no significant sintering behavior of copper particles, although the particle size is comparable with the initial value of the other samples. In close resemblance to the HTL structure this is attributed to the strong embedding of the copper particles in a ZnO matrix which also explains why the activity of CZA3 is significantly lower than CZA2, although the copper content is only decreased by 20%.

4.5.3 XRD Analysis

In all samples, the main reflections can be assigned to Cu and ZnO. Furthermore, sample CZA2 and CZA5 show ZnAl₂O₄ spinel reflections which strongly increase in intensity during the deactivation process. CZA4 also shows weak reflections of the spinel phase, but too ill defined to be included in the Rietveld fits. Exemplarily the diffraction pattern of CZA1 and CZA5 are shown after 0 and 40 days in figure 5. The (nominal) amount of spinel formed during methanol synthesis is given in table 4.5 and further examined in the discussion part.

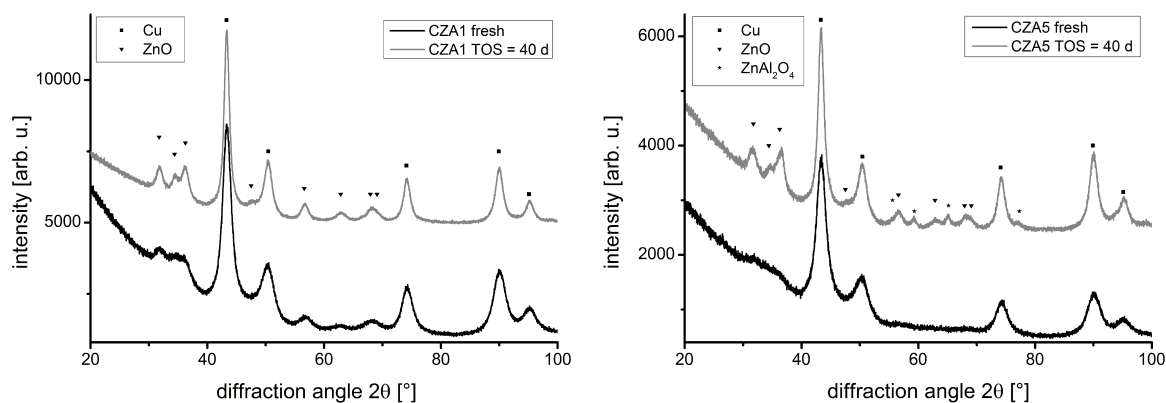


Figure 4.5: Exemplary diffraction pattern of CZA1(left) and CZA5(right) after activation and 40 days TOS.

The pattern of the Cu metal proved to be strongly affected by stacking faults, which cause e.g. hkl dependent peak asymmetries and shifts.[13] Most obvious is the asymmetry of the Cu 200 reflection, which shows a pronounced "foot" on the low angle side. With the conventional Rietveld approach as implemented in the Topas software

such phenomena cannot be modeled on a physical basis. Nevertheless, we used the toolbox of the Rietveld method in order to parameterize the diffraction patterns. For example, the lower angle shoulder of the Cu 200 reflection was fitted using an additional peak with refinable parameters. Stronger deviations in the Rietveld peak intensities were modeled with a spherical harmonics "preferred orientation" model, although we believe that these deviations are not caused by preferred orientation but by stacking faults. Due to these non-physical additions to the fit model, the resulting fit parameters, like crystallite sizes or weight fractions, should not be directly interpreted in their usual physical sense. Rather, the relative evolution of these parameters with time on stream can be tentatively interpreted. For example, crystallite size, microstrain and stacking faults all influence the width of the diffraction peak profiles and cannot be easily deconvoluted. Thus, the (pseudo)crystallite sizes obtained from our fits will probably not represent true crystallite sizes. Nevertheless, we assume that an increase of this parameter with time on stream mostly represents the phenomenon of crystallite growth (sintering). The main results of these fits are presented in figure 4.6 and table 4.4 in the appendix.

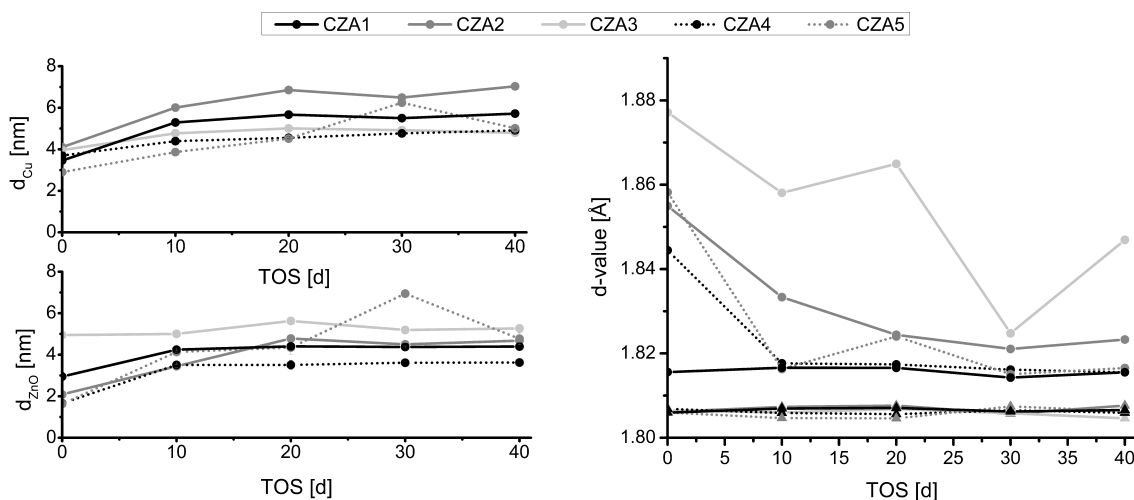


Figure 4.6: Evolution of pseudo-crystallite sizes of Cu and ZnO (left) and of the d-values of the lower angle (circles, right) shoulder and of the Cu 200 main reflection (triangles, right) with time on stream.

As illustrated in the figure, the pseudo-crystallite sizes of Cu and ZnO in most cases increase during the first 10-20 days and then reach a constant value. In case of the samples CZA3 and CZA4, the copper crystallites show only a remarkably slight increase in size. These results are in good agreement with the TEM measurements. The position of the Cu 200 main peak shows no significant variation with time on stream or between

the samples, corresponding to a stable Cu lattice parameter. In contrast, the d-spacing of its lower angle shoulder shows a time dependent evolution for all samples except CZA1. It exhibits a general trend to approach the main peak asymptotically with time, but without reaching it completely. We assume that this indicates a reduction of the stacking fault density with time on stream. However, this does not necessarily mean that the stacking faults are "healed" by annealing. Rather, we suspect that the observed reduction in stacking faults is associated with the crystallite growth. If we assume a growth mechanism similar to Ostwald ripening, then energetically less favorable (i.e. small and/or defect rich) crystallites will be consumed, including their defects. The more stable crystallites, which grow by re-deposition of the dissolved material, would probably retain their original defects, which could explain why a residual amount of stacking faults remains even for long TOS. It has been shown, that these defects heavily contribute to the catalytic activity and are part of the active center of methanol synthesis on copper.[13] The coherent domain size of the ZnO phase also increases with TOS, which - in combination with the other characterization results - generates another aspect of the deactivation behavior of Cu/ZnO/Al₂O₃ catalysts and will be discussed below.

4.5.4 Particle Surface Area and Pore Structure

The catalysts' surface areas and average pore diameter according to N₂ physisorption is given in figure 4.7 and table 4.4 in the appendix. The fresh activated samples CZA4 and CZA5 exhibit a significantly higher BET surface area than CZA1-3 which is attributed to the modified precipitation procedure.[29] However, during the aging procedure, the BET surface area of all catalysts with exception of CZA4 levels off at roughly 60 m² g_{cat}⁻¹. In all cases the catalyst pore volume does not change significantly with TOS and the decrease in total surface area is hence attributed to an increase in the average pore size, which is also consistent with the BJH results.

Whereas the samples CZA1, CZA4, and CZA5 exhibit a narrow monomodal pore size distribution, the distributions of the traditional coprecipitated samples CZA2 and CZA3 are bimodal. This underlines the strong influence of the synthesis conditions on the catalyst structure, as the catalyst pore size distribution is - just as the resulting catalyst phase composition - determined during the precursor aging and subsequent calcination step.[41] After 20 days of aging no further significant changes in the pore structure occur.

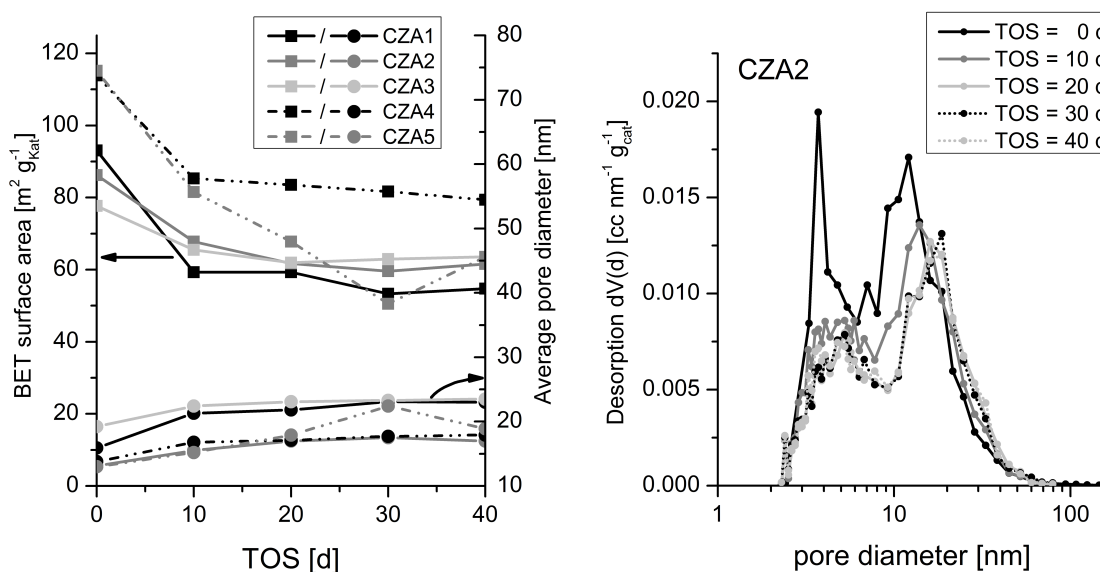


Figure 4.7: (left) BET Surface area and average pore diameter of the fresh activated and aged catalysts. (right) Development of the pore size distribution of CZA2 which stands exemplary for the other samples.

4.5.5 Temperature Programmed Hydrogen Desorption

Recently it has been shown that temperature programmed H₂ desorption can be used as a precise complementary technique to analyze the copper surface area and the extent of the copper-zinc interaction by counting oxygen defect sites in ZnO_x. [33, 42] In addition to the quantitative information about the copper surface area, which influences the intensity of the desorption signal, the Cu-Zn interaction can be evaluated by the temperature range of the desorption signal. [34] An analysis of the fresh and aged samples after TOS = 40 d shows major changes in the resulting TPD spectra where the originally slightly bimodal desorption signal is broadened and significantly shifted to lower desorption temperatures. Furthermore, a signal around 400 K evolves which is attributed to the decomposition of water on the copper surface during the TPD measurement. [43] These changes can be reproduced with very good accuracy (see figure 4.8) and are present in all catalysts. To some extent this phenomenon has been described as a result of morphologic changes during the exposure of the catalyst to different reducing gas atmospheres and hence forming oxygen vacancies at the copper zinc interface, but the resulting shift is much larger than would be expected. [15, 16, 31] Furthermore, a study performed at T = 523 K, p = 24 bar and a WHSV of 29 h⁻¹ shows no significant changes of the H₂-desorption signal

on CZA2 in the first 130 hours and a slow development of the signal in the following 200 hours.

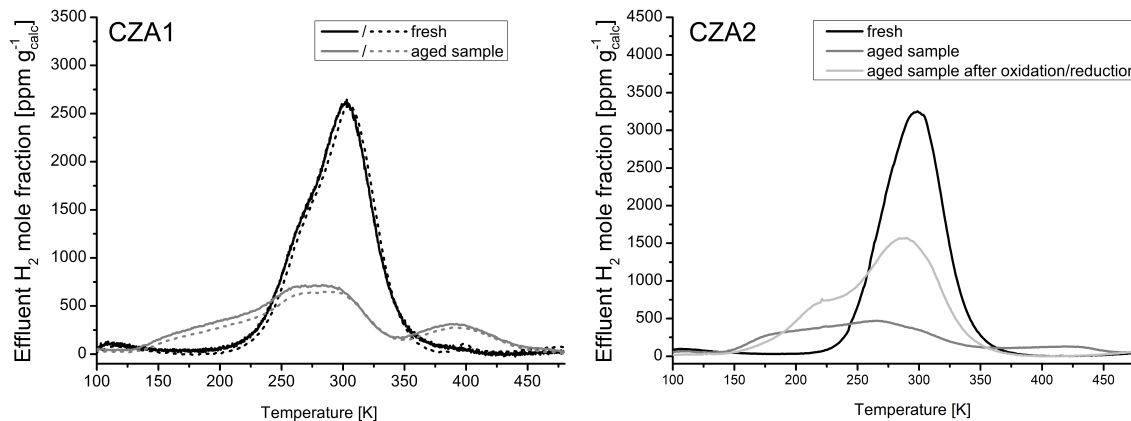


Figure 4.8: (left) Reproduction H₂-TPD experiments of the fresh and aged (TOS = 40 d) CZA1 catalyst samples. (right) Shift of the H₂ desorption signal during the aging treatment for 40 d and after oxidation/reduction of the aged sample.

The nature of the copper sites causing this shift to low temperatures is not yet known. However, in accordance with the known shift phenomenon caused by morphologic changes of the copper particles under reducing gas atmospheres and migration of ZnO_x onto the catalyst particles, a change in the copper surface decoration is conceivable.[15] This could be attributed to a change in the copper/zinc interaction as well as to the decoration of copper with another strong adsorbate. As this low temperature signal is broad and not very distinctive, no ordered surface feature but rather a transient change of the surface is expected. The assumption of covering the copper surface with an oxidisable adsorbate like ZnO_x is also supported by the results of the oxidation/reduction experiment on CZA2. After the mild oxidation and catalyst activation procedure the intensity of the original Cu/Zn signal located at 300 K and the overall copper surface area according to the H₂-TPD measurements is remarkably higher. In contrast, the N₂O surface area - which measures ZnO_x sites and the copper surface - decreases during the oxidation step. Also the low temperature signal sharpens which indicates a more defined structure of the resulting surface feature. The trend in specific copper surface area is in good agreement with an increased wetting of the copper particles by partially reduced ZnO_x during the aging treatment. During the oxidative treatment this process is partially reversed and the copper surface is more accessible for the hydrogen atoms whereas less oxygen defect sites are counted via N₂O-RFC. The activity measurements at 24 bar synthesis gas and temperatures ranging from 453 K up to 523 K show an increase in catalytic activity which is constant for more than 8 h. This proves that

these structural changes are relatively stable compared to conventional morphologic or weak adsorbate induced activity changes.[15, 31] The results of the TPD analysis and the oxidation experiment are given in figure 4.8 and table 4.2. The reported relative activity a_{rel} is determined according to equation 4.1. It can be concluded that the sample was successfully transferred from the aging setup to the TPD setup as the N₂O-RFC measurements of the fresh and aged catalyst are well comparable. It should be noted that - due to the difficult preparation process using activated catalyst samples - the kinetic measurements at the TPD setup are performed under low dilution with SiC. Therefore the relative activity of the very active fresh sample might be overestimated by a minor hotspot formation of roughly 5 K.

Table 4.2: Comparison of N₂O-RFC and activity results on the different measurement setups and resulting H₂-TPD area for sample CZA2.

TOS	$n_{N_2O}^{[a,b]}$	$n_{H_2}^{[a,c]}$	$a_{rel,aging}^{[d]}$	$a_{rel,TPD}^{[e]}$
fresh	360 / 365 (100%)	180 (100%)	1	1
40 d	230 / 203 (56%)	61 (34%)	0.53	0.32
40 d ox/red	n.d. / 129 (35%)	141 (78%)	-	0.50

[a] $\mu\text{mol g}_{cat}^{-1}$ [b] aging setup / TPD setup [c] in the aged samples only signals below 350 K are considered as Cu surface [d] aging setup, $p = 60$ bar [e] TPD setup, $p = 24$ bar

4.6 Discussion

In order to facilitate the discussion of the deactivation processes, the analyzed structural changes of the catalysts are qualitatively outlined in table 4.3, the corresponding quantitative values can be found in table 4.4 in the appendix.

Table 4.3: Qualitative outline of the structural changes after 40 d aging procedure.

Sample	Phase	a _{rel}	SA _{Cu}	D _{Cu}	D _{ZnO}	d(200)	ZnAl ₂ O ₄	S _{BET}	D _{Pore}
CZA1	ZMT	--	--	+	+	0	0	--	++
CZA2	ZMT + HTL	--	--	++	++	-	++	--	+
CZA3	ex-Aurichalcite	-	-	0	0	-	0	--	+
CZA4	n.d.	n.d.	-	0	++	--	+	-	+
CZA5	n.d.	n.d.	--	++	++	--	++	--	++

Most of the structural and activity changes take place during the first 20 days of catalyst aging which is in a good agreement with the initial formation period described in literature.[23] In general, all catalysts loose BET surface area and specific copper surface area (as determined by N₂O-RFC) accompanied by an initial decrease in the stacking fault concentration in the copper phase. The samples CZA1 and CZA2 exhibit a similar deactivation trend losing roughly 40% of the initial activity whereas the ZnO rich sample CZA3 exhibits a more stable behavior.

The BET measurements show that only minor changes in the pore structure are present which is consistent with no apparent change in the microstructural composition as determined by the TEM-EDX measurements. One prominent feature of the deactivation process is the drop in BET surface area which is accompanied by a shift of the mean pore size distribution to higher pore diameters at constant pore volume. This implies a general coarsening of the particles - especially in the first 10 days TOS - but solid particle formation in a macroscopic scale is neither observed nor expected. This is also supported by the TEM measurements and leads to the assumption that the catalyst deactivation is not accompanied by increasing transport limitation phenomena in the catalyst phase. This indeed suggests the sintering of copper particles to be the main reason for the catalyst deactivation, which can be supported by the copper surface-activity correlation presented in figure 4.9.

An analysis of the activity per copper surface area however yields a significant difference between the CZA1 and CZA2 system, as the specific activity of CZA1 and CZA3 - in contrast to CZA2 - first increases during the first 10 days TOS and then levels off (see figure 4.9). This is in agreement with a strong overestimation of the apparent copper surface area of the fresh CZA1 sample. It should be noted that the copper surface area determined via N₂O-RFC is heavily biased by the Cu-ZnO interaction and

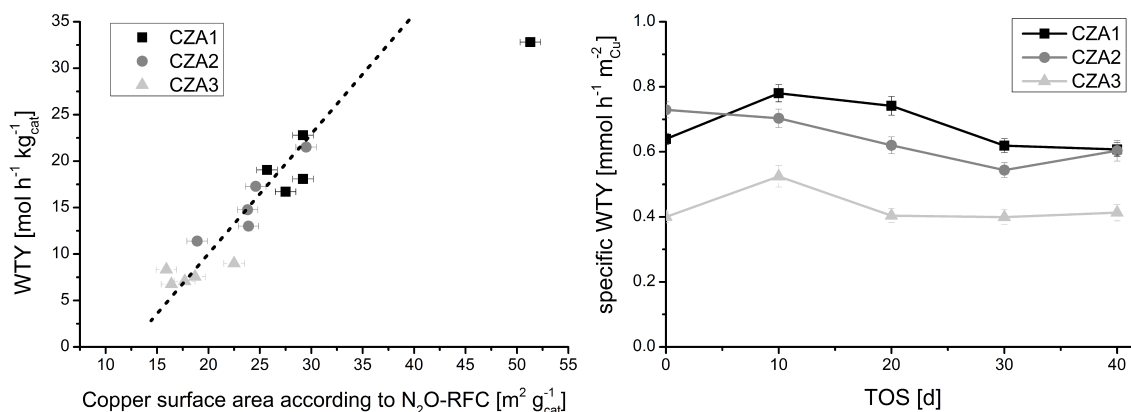


Figure 4.9: (left) Correlation of the specific copper surface area (measured by N₂O-RFC) with the catalyst activity. The dashed line represents the empiric surface area - activity correlation. (right) Specific activity of the catalysts with TOS based on the exposed copper surface area according to N₂O-RFC.

that these area-activity correlations are generally only valid for samples which exhibit similarities in preparation technique and microstructure.[33, 35] As the bias stems from an oxidation of partially reduced ZnO_x sites which depend on the Cu-Zn interaction as well as on the ZnO dispersion, a crystallization of ZnO (vide infra) may lead to a decrease in the measured specific copper surface area determined by N₂O-RFC which would virtually increase the intrinsic activity. Although the N₂O-RFC suffers from those drawbacks, a strong correlation of the specific copper surface area and activity is found. Looking at the copper particle sizes determined by TEM and XRD measurements, a clear distinction has to be made between samples with large (CZA1, CZA2, CZA5) and less (CZA4, CZA3) particle growth.

Taking the observations mentioned above into account, different aging processes and mechanisms leading to catalyst deactivation and sintering phenomena have to be considered. This especially applies to the role of ZnO as structural support: in general, sintering of metal catalysts is traditionally only applied to a mobile metallic phase, whereas the structural support is treated as a static entity. In contrast to this assumption, in all measurements a significant increase of the ZnO pseudo-crystallite size with TOS is observed in the XRD measurements, which contradicts the model assumption of a static support. Especially in the case of CZA4, the ZnO domain size increases by more than 100% whereas the Cu domain size increases by less than 20%. The latter fact is supported nicely by the TEM copper particle size distributions given in figure 4.11. As another clue, the Hüttig temperature of ZnO is much higher than the one of copper and more than 70 K higher than the experimental conditions, which supports

the theory that classical sintering mechanisms like Ostwald ripening are in this case not very likely. Furthermore, the XRD measurements show that the concentration of planar defects in the copper phase does not vanish during the aging period, but reaches a plateau which is consistent with findings that planar defects in copper particles of methanol synthesis catalysts are stable under synthesis conditions.[44] In the analyzed samples, the TEM measurements show the formation of new defect sites at the grain boundary of contacting copper particles which is the initial stage of particle sintering. The stability of those defect sites indicates that the copper particles however behave at least partially rigid and no further sintering occurs. In contrast to the apparent rigidity of copper particles, the mobility of ZnO in presence of Cu - which is attributed to the strong SMSI effect - is well known.[45] As ZnO also acts as the predominant structural spacer in the ZMT phase, a sintering mechanism on the basis of local depletion of ZnO can be proposed: the ZnO initially keeping apart the copper particles is leached out which leads to the formation of grain boundaries and the intraparticle necks observed in the TEM measurements.

With respect to this mechanism also another effect can be explained: although the very homogeneous ZMT sample CZA1 exhibits a higher copper concentration and smaller mean copper particle sizes than CZA2, the degree of sintering of the latter is much higher and leads to the formation of the highest mean copper particle size in all examined systems. As the governing phase in both catalysts is the ZMT and CZA1 contains lower amounts of alumina - which is commonly accepted to act as a structural spacer - this is not expected a priori. However, the higher amount of alumina in CZA2 leads - according to the XRD and TEM analysis - to the formation of significant amounts of crystalline ZnAl₂O₄ thus effectively removing ZnO from the system and increasing the copper particle contact probability. To a smaller degree, the same effect can be observed by comparing CZA1 and CZA5 which also shows the formation of a zinc alumina spinel structure. The proposed sintering mechanism is illustrated in figure 4.10.

In case of the ZnO rich CZA3 sample no significant change in the copper particle diameter is found in the TEM and XRD measurements. Nevertheless the catalyst loses roughly 25% of the initial activity which points to an additional possible deactivation mechanism for methanol synthesis catalysts. An analysis of the copper metal surface via H₂-TPD and N₂O-RFC reveals that the accessible copper surface is reduced by a factor of two which strongly suggests an increased coverage of copper particles with ZnO possibly blocking active sites. This is also supported by the initial strong embedding of copper particles in ZnO which leads to a decreased initial activity of CZA2. This behavior is well known for supported copper model catalysts and the formation of an amorphous overlayer over the copper particles is also visible in the HR-TEM measurements of the samples.[15] As in this process new ZnO_x sites are generated, the N₂O-RFC only shows

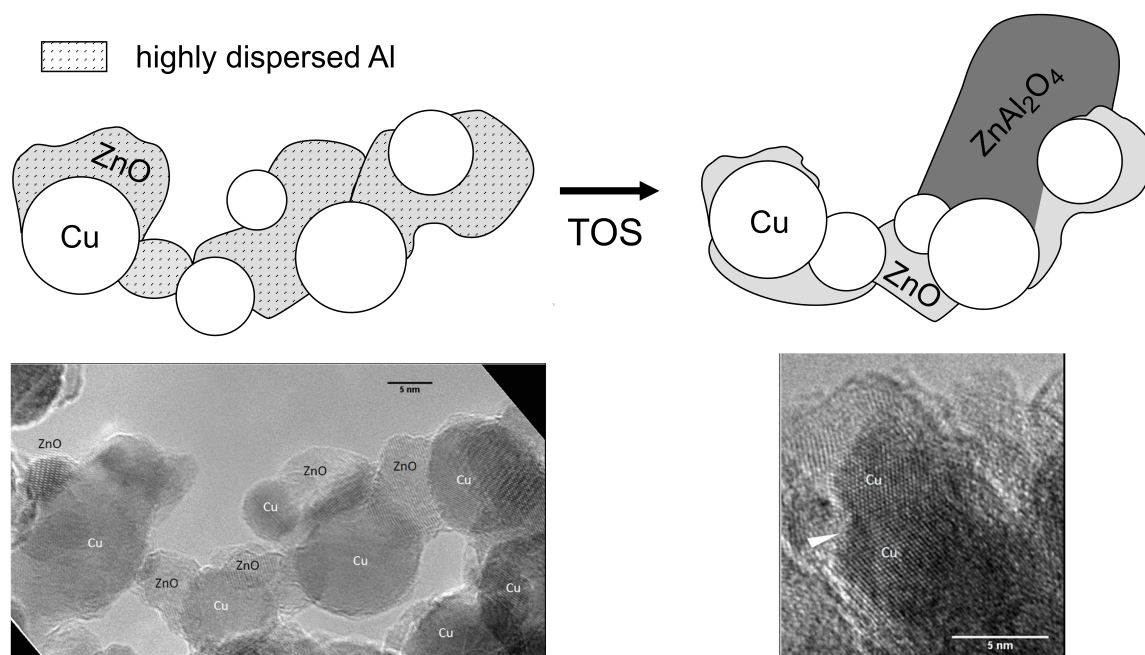


Figure 4.10: Scheme of the deactivation process in the ZMT catalyst phase.

less decrease than the H₂-TPD results would imply. Also in all systems, the formation of a low temperature desorption signal in the H₂-TPD measurements is found, which suggests this process is accompanied by further alteration of the copper surface. The precise implications of the signal - which is present in all catalysts - are not known yet, but the oxidation/reduction cycle experiments on CZA2 imply possible formation of a new surface feature which involves a strongly covered ZnO_x surface or other oxidisable adsorbate molecules. The formation of a unique ZnO layer over copper particles leading to ZnO in lower oxidation states has also been recently proposed by Schott et al. [46]. Furthermore, Kuld et. al. [42] showed that the incorporation of Zn into the copper surface leads to a decrease in hydrogen adsorption enthalpy which shifts the desorption signal to lower temperatures. The oxidation/reduction cycle on CZA2 also shows that this process is partially reversible and that a higher exposed copper surface area is present after the oxidation/reduction treatment which also leads to an increase in catalyst activity. The coinciding drop in copper surface area according to N₂O-RFC after the O₂ treatment can be attributed to a combination of sintering of copper particles during the oxidative treatment and a reduced formation of ZnO_x which stems from the Cu-ZnO interaction.

4.7 Conclusion

In summary, the presented results imply that the deactivation mechanisms of methanol synthesis catalysts are much more complicated and can hardly be described as pure sintering processes. They strongly depend on the particular catalyst microstructure and mobility of ZnO. In the usually present ZMT structure the ZnO residing between copper particles is locally depleted leading to new contacts between the copper particles and the formation of stable twinning boundaries. In excess of alumina this effect is accelerated by the crystallization of ZnAl₂O₄ which acts as a sink for the formerly mobile ZnO species. As in the presence of water the formation of mobile Zn-OH-like species may be promoted, this is also in line with the proposed stronger sintering of copper particles in the presence of water.[9, 22] In the ex-Aurichalcite and HTL structure the copper particles are well stabilized by embedding them in either a partially amorphous ZnO or an amorphous ZnO/Al₂O₃ matrix respectively. However the strong embedding and strong Cu-ZnO interaction blocks the active sites in both cases. In the HTL phase also the depletion of ZnO from the embedded Cu particles by forming ZnAl₂O₄ is possible as observed in HR-TEM measurements. The whole deactivation process is accompanied by a change in the H₂ desorption behavior which points to changes in the nature of the exposed copper surface areas. The presented findings develop a basic understanding of the governing deactivation mechanisms in methanol synthesis catalysts and play a vital role in rational catalyst design and further development of high-performance methanol synthesis catalysts in order to improve catalyst stability and hence more sustainable processes.

4.8 Supporting Information

Table 4.4: Summary of the characterization results of the fresh and aged catalysts. The presented parameters are BET surface area (S_{BET}), pore volume (V_{p}), pore diameter (d_{p}), copper surface area according to N₂O-RFC ($S_{\text{Cu,N}_2\text{O}}$), copper and zinc pseudo particle diameter (d_{Cu} & d_{Zn}) according to XRD and weight time yield of methanol under kinetic conditions (WTY).

CZA1						
TOS	[d]	0	10	20	30	40
S_{BET}	$[\text{m}^2 \text{g}_{\text{cat}}^{-1}]$	93.1	59.3	59.3	53.5	54.7
V_{p}	$[\text{cm}^3 \text{g}_{\text{cat}}^{-1}]$	0.3696	0.3164	0.323	0.3084	0.3138
d_{p}	[nm]	15.9	21.3	21.8	23.1	23.0
$S_{\text{Cu,N}_2\text{O}}$	$[\text{m}^2 \text{g}_{\text{cat}}^{-1}]$	51.3	29.2	25.7	29.2	27.5
d_{Cu}	[nm]	3.5	5.3	5.7	5.5	5.7
d_{Zn}	[nm]	2.9	4.2	4.4	4.4	4.4
WTY	$[\text{mol h}^{-1} \text{kg}_{\text{cat}}^{-1}]$	32.8	22.8	19.1	18.1	16.7

CZA2						
TOS	[d]	0	10	20	30	40
S_{BET}	$[\text{m}^2 \text{g}_{\text{cat}}^{-1}]$	86.2	67.8	61.7	59.6	61.6
V_{p}	$[\text{cm}^3 \text{g}_{\text{cat}}^{-1}]$	0.28	0.26	0.26	0.26	0.26
d_{p}	[nm]	13.1	15.5	17.0	17.5	17.0
$S_{\text{Cu,N}_2\text{O}}$	$[\text{m}^2 \text{g}_{\text{cat}}^{-1}]$	29.5	24.6	23.8	23.9	18.9
d_{Cu}	[nm]	4.1	6.0	6.9	6.5	7.0
d_{Zn}	[nm]	2.1	3.4	4.8	4.5	4.7
WTY	$[\text{mol h}^{-1} \text{kg}_{\text{cat}}^{-1}]$	21.5	17.3	14.8	13.0	11.4

CZA3						
TOS	[d]	0	10	20	30	40
S _{BET}	[m ² g _{cat} ⁻¹]	77.7	65.5	61.9	62.9	63.3
V _p	[cm ³ g _{cat} ⁻¹]	0.373	0.367	0.358	0.366	0.372
d _p	[nm]	19.2	22.4	23.1	23.3	23.5
S _{Cu,N₂O}	[m ² g _{cat} ⁻¹]	22.5	15.9	18.7	17.7	16.4
d _{Cu}	[nm]	4.0	4.8	5.0	4.9	4.8
d _{Zn}	[nm]	4.9	5.0	5.6	5.2	5.3
WTY	[mol h ⁻¹ kg _{cat} ⁻¹]	9.0	8.3	7.5	7.1	6.8

CZA4						
TOS	[d]	0	10	20	30	40
S _{BET}	[m ² g _{cat} ⁻¹]	113.9	85.3	83.5	81.7	79.4
V _p	[cm ³ g _{cat} ⁻¹]	0.3934	0.3581	0.3571	0.3620	0.3561
d _p	[nm]	13.8	16.8	17.1	17.7	17.9
S _{Cu,N₂O}	[m ² g _{cat} ⁻¹]	34.8	27.3	25.2	23.2	21.9
d _{Cu}	[nm]	3.7	4.4	4.6	4.8	4.9
d _{Zn}	[nm]	1.7	3.5	3.5	3.6	3.6

CZA5						
TOS	[d]	0	10	20	30	40
S _{BET}	[m ² g _{cat} ⁻¹]	115.2	81.5	67.8	50.5	63.5
V _p	[cm ³ g _{cat} ⁻¹]	0.3739	0.3094	0.3042	0.2832	0.2998
d _p	[nm]	13.0	15.2	17.9	22.4	18.9
S _{Cu,N₂O}	[m ² g _{cat} ⁻¹]	34.8	27.3	25.2	23.2	21.9
d _{Cu}	[nm]	2.9	3.9	4.5	6.2	5.0
d _{Zn}	[nm]	1.6	4.1	4.3	6.9	4.8

Table 4.5: Relative amount of ZnAl₂O₄ spinell compared to the copper phase as given by the Rietveld analysis.

TOS [d]	fresh	10	20	30	40
CZA2 [%]	8±11	30±4	32±4	44±12	33±4
CZA5 [%]	-	18±5	37±17	30±2	27±3

Table 4.6: Summary of the H₂-TPD and N₂O-RFC adsorption capacities on fresh and aged catalyst.

Sample	CZA1		CZA2		CZA3	
	fresh	40 d	fresh	40 d	fresh	40 d
n _{H₂} [μmol g _{cat} ⁻¹]	173	81 (47%)	180	61 (34%)	119	60 (50%)
n _{N₂O} [μmol g _{cat} ⁻¹]	599	329 (55%)	365	203 (56%)	269	178 (66%)

Table 4.7: Mean copper particle diameter according to the TEM measurements (d_{Cu,TEM}).

d _{Cu,TEM} [nm]	CZA1	CZA2	CZA3	CZA4	CZA5
fresh	8.1	12.3	11.2	11.6	9.4
10 d	9.8	16.1	10.9	10.9	10.1
20 d	10.5	16.7	10.9	11.2	11.2
30 d	11.4	17.7	10.9	11.8	13.4
40 d	11.3	19.7	11.3	11.7	12.8

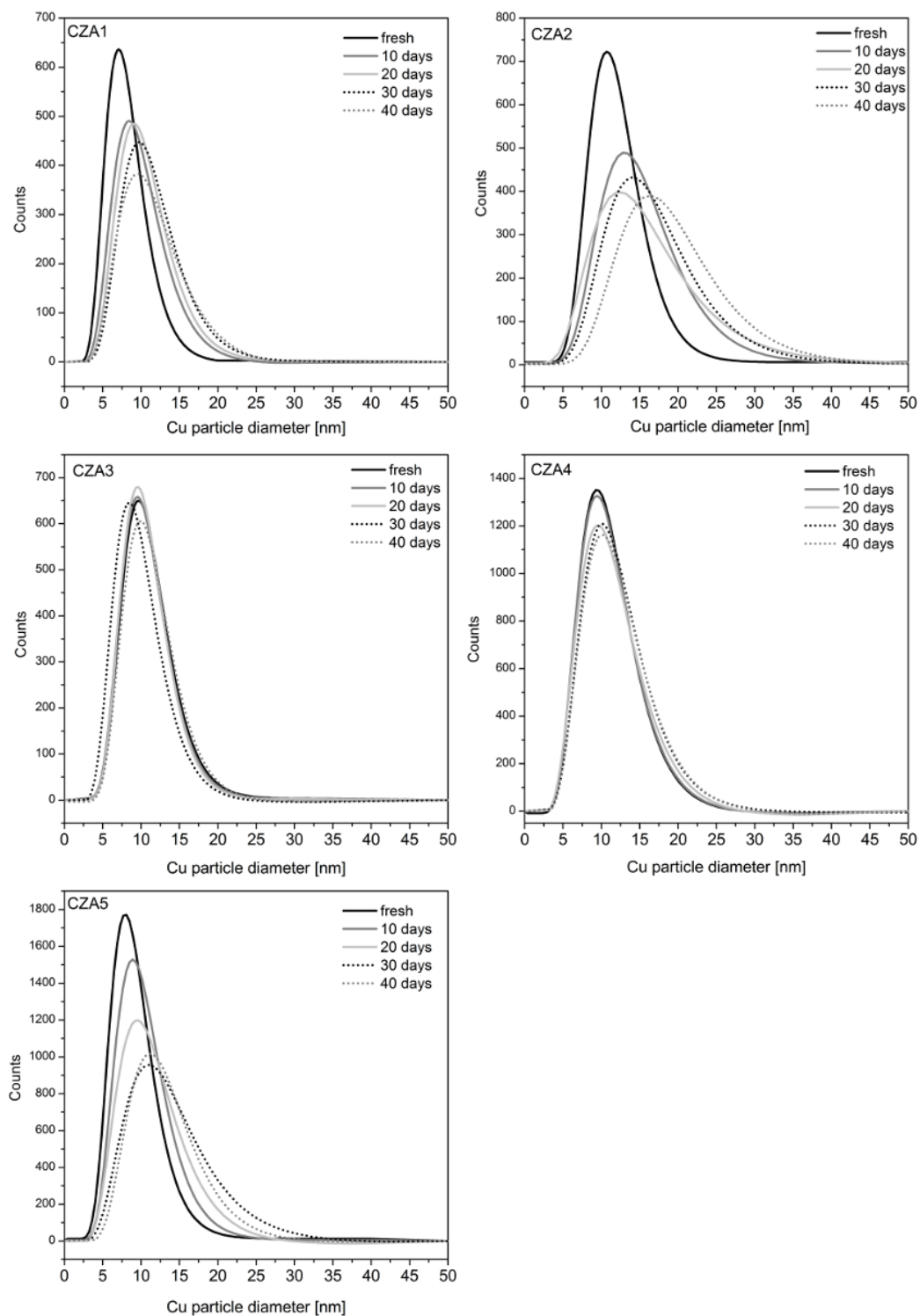


Figure 4.11: Copper particle size distribution according to the TEM measurements.

References

- [1] R. Malhotra, *Fossil Energy*, Springer, New York, **2012**.
- [2] G. A. Olah, A. Goeppert, G. K. S. Prakash, *Beyond Oil and Gas: The Methanol Economy*, Wiley-VCH Verlag GmbH & Co. KGaA, Weinheim, Auflage: 2. vollst. überarb. u. erw. Auflage, **2009**.
- [3] G. A. Olah, *Angew. Chem. Int. Ed.* **2013**, *52*, 104–107, DOI 10.1002/anie.201204995.
- [4] P. Forzatti, L. Lietti, *Catal. Today* **1999**, *52*, 165–181, DOI 10.1016/S0920-5861(99)00074-7.
- [5] C. H. Bartholomew, *Appl. Cat. A* **2001**, *212*, 17–60, DOI 10.1016/S0926-860X(00)00843-7.
- [6] M. V. Twigg, M. S. Spencer, *Top. Catal.* **2003**, *22*, 191–203, DOI 10.1023/A:1023567718303.
- [7] M. V. Twigg, M. S. Spencer, *Appl. Cat. A* **2001**, *212*, 161–174, DOI 10.1016/S0926-860X(00)00854-1.
- [8] G. Hochgesand, *Ind. Eng. Chem.* **1970**, *62*, 37–43, DOI 10.1021/ie50727a007.
- [9] H. H. Kung, *Catal. Today* **1992**, *11*, 443–453, DOI 10.1016/0920-5861(92)80037-N.
- [10] M. R. Rahimpour, B. Moghtaderi, A. Jahanmiri, N. Rezaie, *Chem. Eng. Technol.* **2005**, *28*, 226–234, DOI 10.1002/ceat.200407062.
- [11] L. C. Grabow, M. Mavrikakis, *ACS Catal.* **2011**, *1*, 365–384, DOI 10.1021/cs200055d.
- [12] T Askgaard, *J. Catal.* **1995**, *156*, 229–242, DOI 10.1006/jcat.1995.1250.
- [13] M. Behrens, F. Studt, I. Kasatkin, S. Kühl, M. Hävecker, F. Abild-Pedersen, S. Zander, F. Girgsdies, P. Kurr, B.-L. Kniep, M. Tovar, R. W. Fischer, J. K. Nørskov, R. Schlögl, *Science* **2012**, *336*, 893–897, DOI 10.1126/science.1219831.
- [14] M. Peter, J. Fendt, S. Pleintinger, O. Hinrichsen, *Catal. Sci. Technol* **2012**, *2*, 2249–2257, DOI 10.1039/c2cy20189e.
- [15] P. C. Vesborg, I. Chorkendorff, I. Knudsen, O. Balmes, J. Nerlov, A. M. Molenbroek, B. S. Clausen, S. Helveg, *J. Catal.* **2009**, *262*, 65–72, DOI 10.1016/j.jcat.2008.11.028.
- [16] C. V. Ovesen, B. S. Clausen, J. Schiøtz, P. Stoltze, H. Topsøe, J. K. Nørskov, *J. Catal.* **1997**, *168*, 133–142, DOI 10.1006/jcat.1997.1629.

- [17] I. Kasatkin, P. Kurr, B. Kniep, A. Trunschke, R. Schlögl, *Angew. Chem.* **2007**, *119*, 7465–7468, DOI 10.1002/ange.200702600.
- [18] Y Choi, K Futagami, T Fujitani, J Nakamura, *Appl. Cat. A* **2001**, *208*, 163–167, DOI 10.1016/S0926-860X(00)00712-2.
- [19] S. Polarz, J. Strunk, V. Ischenko, M. W. E. van den Berg, O. Hinrichsen, M. Muhler, M. Driess, *Angew. Chem. Int. Ed* **2006**, *45*, 2965–2969, DOI 10.1002/anie.200503068.
- [20] R. N. d'Alnoncourt, X. Xia, J. Strunk, E. Löffler, O. Hinrichsen, M. Muhler, *Phys. Chem. Chem. Phys.* **2006**, *8*, 1525–1538, DOI 10.1039/B515487A.
- [21] T. Kandemir, D. Wallacher, T. Hansen, K.-D. Liss, R. Naumann d'Alnoncourt, R. Schlögl, M. Behrens, *Nuclear Instruments and Methods in Physics Research Section A: Accelerators Spectrometers Detectors and Associated Equipment* **2012**, *673*, 51–55, DOI 10.1016/j.nima.2012.01.019.
- [22] J. T. Sun, I. S. Metcalfe, M. Sahibzada, *Ind. Eng. Chem. Res.* **1999**, *38*, 3868–3872, DOI 10.1021/ie990078s.
- [23] M. Kurtz, H. Wilmer, T. Genger, O. Hinrichsen, M. Muhler, *Catal. Lett.* **2003**, *86*, 77–80–80, DOI 10.1023/A:1022663125977.
- [24] G. Prieto, J. Zečević, H. Friedrich, K. P. de Jong, P. E. de Jongh, *Nature Materials* **2012**, DOI 10.1038/nmat3471.
- [25] M. Behrens, R. Schlögl, *Z. Anorg. Allg. Chem.* **2013**, *639*, 2683–2695, DOI 10.1002/zaac.201300356.
- [26] M. Behrens, S. Zander, P. Kurr, N. Jacobsen, J. Senker, G. Koch, T. Ressler, R. W. Fischer, R. Schlögl, *J. Am. Chem. Soc.* **2013**, *135*, 6061–6068, DOI 10.1021/ja310456f.
- [27] J. Schumann, T Lunkenbein, A Tarasov, N Thomas, R Schlögl, M. Behrens, *ChemCatChem* **2014**, *submitted*, DOI cctc.201402278.
- [28] E. Doesburg, R. Höppener, B. de Koning, X. Xiaoding, J. Scholten in *Preparation of catalysts IV scientific bases for the preparation of heterogeneous catalysts: proceedings of the fourth international symposium; Louvain-la-Neuve, September 1-4, 1986*, (Ed.: B. Delmon, F. Grange, P.A. Jacobs, G. Poncelet), Preparation of Catalysts IV Scientific Bases for the Preparation of Heterogeneous Catalysts, Elsevier, Amsterdam, **1987**, pp. 767–780.
- [29] S. Kaluza, M. Behrens, N. Schiefenhövel, B. Kniep, R. Fischer, R. Schlögl, M. Muhler, *ChemCatChem* **2011**, *3*, 189–199, DOI 10.1002/cctc.201000329.
- [30] TOPAS v. 4.2, copyright 1999, Bruker AXS, **2009**.

- [31] O. Hinrichsen, T. Genger, M. Muhler, *Chem. Eng. Technol.* **2000**, *23*, 956–959, DOI 10.1002/1521-4125(200011)23:11<956::AID-CEAT956>3.0.CO;2-L.
- [32] T. Genger, O. Hinrichsen, M. Muhler, *Catal. Lett.* **1999**, *59*, 137–141, DOI 10.1023/A:1019076722708.
- [33] M. B. Fichtl, J. Schumann, I. Kasatkin, N. Jacobsen, M. Behrens, R. Schlögl, M. Muhler, O. Hinrichsen, *Angew. Chem. Int. Ed.* **2014**, *53*, 7043–7047, DOI 10.1002/anie.201400575.
- [34] H. Wilmer, T. Genger, O. Hinrichsen, *J. Catal.* **2003**, *215*, 188–198, DOI 10.1016/S0021-9517(03)00003-4.
- [35] O. Martin, J. Pérez-Ramírez, *Catal. Sci. Technol.* **2013**, *3*, 3343–3352, DOI 10.1039/C3CY00573A.
- [36] S. Zander, E. L. Kunkes, M. E. Schuster, J. Schumann, G. Weinberg, D. Teschner, N. Jacobsen, R. Schlögl, M. Behrens, *Angew. Chem. Int. Ed.* **2013**, *52*, 6536–6540, DOI 10.1002/anie.201301419.
- [37] M. M. Günter, T. Ressler, B. Bems, C. Büscher, T. Genger, O. Hinrichsen, M. Muhler, R. Schlögl, *Catal. Lett.* **2001**, *71*, 37–44.
- [38] P. L. Hansen, J. B. Wagner, S. Helveg, J. R. Rostrup-Nielsen, B. S. Clausen, H. Topsøe, *Science* **2002**, *295*, 2053–2055, DOI 10.1126/science.1069325.
- [39] C. Baltés, S. Vukojević, F. Schüth, *J. Catal.* **2008**, *258*, 334–344, DOI 10.1016/j.jcat.2008.07.004.
- [40] M. Behrens, I. Kasatkin, S. Kühn, G. Weinberg, *Chem. Mater.* **2010**, *22*, 386–397, DOI 10.1021/cm9029165.
- [41] M. Behrens, *J. Catal.* **2009**, *267*, 24–29.
- [42] S. Kuld, C. Conradsen, P. G. Moses, I. Chorkendorff, J. Sehested, *Angew. Chem. Int. Ed.* **2014**, *53*, 5941–5945, DOI 10.1002/anie.201311073.
- [43] O. Hinrichsen, T. Genger, M. Muhler in *Studies in Surface Science and Catalysis*, (Eds.: A. Corma, F. V. Melo, S. Mendioroz, J. L. G. Fierro), 12th International Congress on Catalysis Proceedings of the 12th ICC, Elsevier, **2000**, pp. 3825–3830.
- [44] T. Kandemir, F. Girgsdies, T. C. Hansen, K.-D. Liss, I. Kasatkin, E. L. Kunkes, G. Wowsnick, N. Jacobsen, R. Schlögl, M. Behrens, *Angew. Chem. Int. Ed.* **2013**, *52*, 5166–5170, DOI 10.1002/anie.201209539.
- [45] J.-D. Grunwaldt, A. Molenbroek, N.-Y. Topsøe, H. Topsøe, B. S. Clausen, *J. Catal.* **2000**, *194*, 452–460, DOI 10.1006/jcat.2000.2930.

- [46] V. Schott, H. Oberhofer, A. Birkner, M. Xu, Y. Wang, M. Muhler, K. Reuter, C. Wöll, *Angew. Chem. Int. Ed.* **2013**, *52*, 11925–11929, DOI 10.1002/anie.201302315.

5 Kinetics of Deactivation on Cu/ZnO/Al₂O₃ Methanol Synthesis Catalysts

5.1 Abstract

Deactivation behavior is an important topic in catalyst development. In case of methanol synthesis, the conventional Cu/ZnO/Al₂O₃ system is commonly known to be prone to sintering, however, information about the structural development during deactivation or the sintering mechanism are scarce. We present a systematic deactivation study on three different Cu/ZnO/Al₂O₃ catalysts which are aged under constant conditions and periodically analyzed using kinetic measurements and N₂O chemisorption. A power law model for the catalyst activity with time on stream is derived. Also, the corresponding particle size distributions measured by TEM are evaluated and discussed. A numerical simulation of Ostwald Ripening and different coalescence models shows that the sintering of copper in this system is not significantly influenced by the actual particle size, but rather follows a random collision model.

5.2 Introduction

Methanol is one of the most important basic chemicals and represents an important C1 building block for industrial chemicals. It offers access to a whole variety of important industrial products, like formaldehyde, dimethyl ether (DME) or methyl-tert-butylether (MTBE). The methanol to olefins (MTO) and methanol to gasoline (MTG) processes are a pathway to utilize synthesis gas from various feedstocks to produce valuable hydrocarbons. In the typical low-pressure process over Cu/ZnO/Al₂O₃ catalysts pressures ranging from 50 to 100 bar and temperatures of about 483 to 563 K are employed.[1] Apart from usage in the chemical industry, the liquid can also be mixed with gasoline, directly used as fuel for cars or stored and transported as an easy to handle energy carrier. By combining the generation of hydrogen from renewable sources and CO₂ capture methods, methanol can provide sustainable energy storage and feedstock for

various chemicals. This concept of a methanol based economy has been extensively studied by Olah et al.[2, 3]

The deactivation behavior of heterogeneous catalysts is an important characteristic in plant operation and has been studied for many industrial catalytic applications. In these processes, the deactivation mechanisms are classified into different types like chemical poisoning or thermal effects.[4, 5] In case of methanol synthesis catalysts, poisoning with sulfur and halogenides from coal derived synthesis gas was early identified as a problem and prohibited initially the application of the more efficient copper based low pressure process in favor of the more poisoning resistant chromium based high pressure process.[6] However, with the development of more sophisticated desulfurization and halogenide removal methods, poisoning should not be a prominent problem in methanol synthesis anymore.[7, 8] In contrast, the intrinsic deactivation by thermal induced processes like sintering or phase segregation still limits the catalyst lifetime.[9] Especially sintering of copper in ternary Cu/ZnO/Al₂O₃ catalysts has been identified as a major deactivation mechanism in this process. However, detailed or mechanistic studies on sintering of Cu/ZnO/Al₂O₃ are scarce. Hansen and Nielsen mention in their basic introduction to methanol synthesis that under typical operation conditions in a temperature range between 480 and 580 K sintering is a priori not expected according to Tammann's rule ($T_{\text{Tammann}} \approx 680 \text{ K}$).[10] However, they argue it might be possible that sintering occurs by the release of atomic or molecular species according to the Hüttig temperature ($T_{\text{Hüttig}} \approx 450 \text{ K}$). Generally, sintering mechanisms are still under current research and new developments, especially in the field of the transmission electron microscopy, allow a better understanding of the occurring processes.[11] One of the most detailed studies of copper particle growth has recently been presented by Prieto et al. for Cu/ZnO constrained in mesopores of SBA-15.[12] By sophisticated preparation and calcination techniques they succeeded in depositing Cu nanoparticles either homogeneously or concentrated to few mesopores. Electron tomography was used to quantify particle sizes, location in specific pores and interparticle distances of fresh and aged samples. The authors found that classical mean field Ostwald Ripening models failed in describing the particle size distributions and time dependence of sintering. Considerable improvement was gained by introduction of local correlations between particles. Best results were obtained when virtually only the nearest and next-nearest neighbors contributed to the ripening of a particle. For the system with the inhomogeneously distributed particles, however, the model prediction was significantly worse than for the homogeneous system. It was concluded that for short interparticle distances also a coalescence mechanism might have to be considered.

Recently, we presented a study containing detailed characterization data of different conventionally prepared Cu/ZnO/Al₂O₃ catalysts which were systematically aged under

controlled conditions.[13] In contrast to metal support systems - analyzed e.g. by Prieto et al. [12] or Hansen et al. [14] - with the metal nano-particles distributed over an extended support, these catalysts represent bulk catalysts with a particularly different microstructure (see below).

The gathered data led to the conclusion that the mobility and crystallization of ZnO plays a major role in the sintering process and has a large influence on the deactivation behavior. In this study we present a time resolved analysis of the catalyst activity during the aging period and a numerical analysis of the mechanisms, leading to the particle size distributions gathered throughout the deactivation process.

5.3 Experimental and Computational Methods

5.3.1 Catalyst preparation

The preparation, XRD, TEM, TPD and BET characterization of the samples CZA1-3 are accurately described in ref. [13]. After the activation procedure, CZA1 and CZA2 are mainly characterized by an open microstructure in which copper particles are partially covered with ZnO_x and kept apart by ZnO spacers. This catalyst microstructure is well known and commonly ascribed to ex-zincian-malachite precursor phases.[15, 16] In case of CZA2 also some alumina rich regions of γ -Al₂O₃ and ex-hydrotalcite-like precursors are observed. In case of CZA3 the copper particles are strongly embedded in a ZnO matrix which is attributed to the ZnO rich ex-aurichalcite type structure. Typical characterization results are summarized in table 5.1. It should be noted, that in the following context all values based on the mass of calcined catalyst are denoted by m_{calc} , whereas values based on the mass of activated catalyst are denoted by m_{cat} .

Table 5.1: Metal ratio, BET surface area and N₂O-RFC surface area of the analyzed catalyst samples.

Catalyst	Cu:Zn:Al ^[a] [%]	SA _{BET} ^[b] [m ² g _{cat} ⁻¹]	SA _{RFC} ^[b,c] [m ² g _{cat} ⁻¹]	FHI sample number
CZA1	70:28:2	93.1	50.9	15802
CZA2	58:26:16	86.2	29.5	14382
CZA3	43:49:8	77.7	22.5	14383

[a] molar, determined by EDX and XRF [b] activated catalyst [c] error $\pm 1\text{m}^2\text{g}_{\text{cat}}^{-1}$ [d] for future references and comparison with ref. [13]

5.3.2 Deactivation and Kinetic Experiments

The catalysts are aged in a single pass setup equipped with four parallel fixed bed reactors which can be operated up to 70 bar and temperatures up to 773 K. The catalyst bed is placed in glass lined steel tubing (diameter 1/2 inch, maximum length 3 inch) and secured with silica wool plugs. Product analysis is performed with an Agilent 7820A gas chromatograph equipped with two thermal conductivity detectors, a packed Porapak-N column (Sigma Aldrich) for the quantification of CH₄, CO₂, H₂O, CH₂O, CH₃OH and a packed Molsieve 5 Å column (Sigma Aldrich) for the quantification of Ar, N₂, CH₄ and CO. If not reported otherwise, all gas purities are of very high grade (6.0 for Ar, H₂, N₂, 5.5 for CO₂, 5.0 for N₂O, 4.7 for CO) and have been checked for sulfur impurities below 100 ppb. A trap containing 10 g activated methanol synthesis catalyst at room temperature serves as additional guard reactor for traces of sulfur and metal carbonyls. The spent catalysts are dissolved in boiling aqua regia, inspissated and analyzed via ICP-OES (Spectroflame, Spectro Analytical). Within the detection limit of 10 ppm (wt) no traces of iron or nickel were found in the deactivated catalysts, which confirms the absence of metal carbonyl deposition on the catalyst. The synthesis gas used for aging the catalysts and performing the activity tests is a premixed combination of 13.5% CO, 3.5% CO₂, 73.5% H₂ and 9.5% N₂.

In a typical measurement 1000 mg calcined catalyst (sieve fraction 500-710 μm) mixed with 6000 mg purified silicon carbide (sieve fraction 355-500 μm) is heated up at ambient pressure for 15 h in 2.0% H₂ in Argon raising the temperature from 300 to 448 K at 1 K min⁻¹, then in H₂ raising the temperature from 448 K to 513 K at 1 K min⁻¹ and holding for 30 minutes. After the activation procedure the catalysts are cooled down to 308 K in Argon and the first reactive N₂O frontal chromatography (see below) is performed to determine the initial copper surface area. Subsequently the catalysts are heated to 493 K in 2.0% H₂ in Argon, flushed with synthesis gas and pressurized to 60 bar. Initial activity tests are performed for every reactor at 483 K under differential conditions. Afterwards the catalysts are heated up to the aging temperature and aged under a weight hourly space velocity (WHSV, $\frac{\dot{m}_{\text{feed}}}{m_{\text{calc}}}$) of 0.51 h⁻¹. Under these conditions the equilibrium constitution is reached within the first 15% of the catalyst bed length which was confirmed by varying the catalyst loading. Due to dispersion effects at the low flow aging conditions an equilibrated gas atmosphere is obtained over the whole catalyst bed length. This operation provides a way to age the different catalyst samples under constant conditions, even when the respective catalytic activities are different. Although the temperature and pressure region is relevant for industrial methanol production, it should be noted that these conditions were specifically chosen to ensure a fast and reproducible deactivation by stressing the catalysts under high conversions. Hence, these do not represent the gas phase composition which is typically present in the majority of

the catalyst bed in an industrial reactor. Depending on the aging time on stream (TOS) of 1000 h or 1600 h, the catalyst is cooled down to 483 K every 20 or 30 h respectively. After flushing for 30 min with synthesis gas and performing activity measurements under differential conditions, the sample is reheated and further aged. Taking into account the time needed for heating or cooling the reactor, the catalyst is aged under constant conditions for more than 90% of the whole TOS.

To study the influence of the aging temperature, all samples are aged at 523 K as well as at 553 K. In case of CZA1 and CZA3 also aging at 493 K is performed. Here, a second CZA1 sample was further co-fed three times for 12 hours with 4.4 sccm water vapor in order to elucidate its influence on the catalyst stability. In this case the aging WHSV is 0.72 h⁻¹ with the following feed gas composition: 11% CO, 2.9% CO₂, 60.3% H₂, 18% H₂O, 7.8% N₂. This leads to an equilibrium water content of roughly 10%, which can be described as hydrothermal aging of the catalyst. A summary of the aging conditions and the resulting equilibrium gas phase composition is given in table 5.2.

Table 5.2: Aging conditions presented in this study.

T _{aging} [K]	P _{aging} [bar]	CO	CO ₂	H ₂	MeOH [%]	H ₂ O	N ₂
493 ^[a]	60	1.39	3.60	62.68	18.20	1.18	12.96
523	60	3.97	3.73	65.28	14.09	0.75	12.18
553	60	7.73	3.50	68.26	8.74	0.61	11.16
493 + H ₂ O ^[b]	60	1.49	11.28	67.36	1.65	10.17	8.06

[a] CZA1 and CZA3 only [b] CZA1 only

All activity measurements are performed three times in a series which is represented by the error bars in the respective plots. The maximum relative error in methanol yield or CO_x conversion is smaller than 3%. Furthermore, a reduction of the aging period length between activity measurements down to 12 h yielded essentially the same deactivation pattern which confirms that the activity measurements do not influence the catalyst deactivation behavior. Also, careful analysis prior to the deactivation measurements showed that no pore diffusion limitation or hotspot formation are present within the experimental window.

For further analysis, the relative catalyst activity a_{rel} is approximated using the time-dependent CO_x (= CO + CO₂) conversion X_{CO_x} and a power law model (PLM) given in equation 5.1. Since this description of the deactivation mechanism is a pure empiric one and should not be over-interpreted, only even reaction orders m are considered.

$$\frac{da_{rel}}{dt} = -k_a a_{rel}(t)^m \quad (5.1)$$

$$a_{rel}(TOS) = \frac{X_{CO_x}(TOS)}{X_{CO_x}(TOS = 0)} \quad (5.2)$$

It should be noted that this assumption is only valid for differential conversions. With an initial maximum absolute CO_x conversion of 15% and a maximum CO_x conversion of 18% with respect to the equilibrium conversion this assumption is feasible. A reproduction experiment with 250 mg catalyst yielded essentially the same deactivation pattern, however with proceeding catalyst deactivation the kinetic measurements proved to be too inaccurate for a precise analysis.

5.3.3 Reactive N₂O Frontal Chromatography (N₂O-RFC)

During the aging process, the copper surface area according to N₂O-RFC is determined by the method described in ref. [17]. In order to remove surface adsorbates, prior to every measurement the catalyst is flushed for 45 minutes at 523 K with Argon, treated for another 45 minutes with 2% H₂ in Argon at 493 K and cooled down to 308 K in Argon. The surface oxidation is performed with 1% N₂O in an Ar flow and the gas phase composition in the effluent is monitored with a mass spectrometer. In order to ensure comparability with the characterization results presented in ref. [13] all presented N₂O-RFC results are based on the mass of activated catalyst. Hence the sample mass is corrected by the respective mass loss determined by TPR-TG measurements. Due to subsurface oxidation of copper during the N₂O-RFC experiment, an error margin of 1 m² g_{cat}⁻¹ is assumed, which is higher than the actual measured error when reproducing the experiments. It should be noted that this technique in fact does not probe the copper surface area but a combination of exposed copper surface area and oxygen defect sites generated at the Cu-ZnO_x interface.[18, 19] It has been shown that e.g. in case of CZA1 more than 40% of the copper surface area determined by N₂O-RFC is attributed to the oxidation of partially reduced ZnO_x. [18] Furthermore, a fraction of the copper particle surface area is present as interface to the stabilizing oxide matrix and hence not accessible for the gas phase (see below). This effect however, cannot be quantified by XRD or TEM measurements. Hence, the gathered data has to be carefully considered when deducing deactivation or sintering mechanisms solely from one characterization method. Therefore, a combination of TEM-based particle size distributions and N₂O-RFC surface area measurements is used to analyze the deactivation process

5.3.4 Modeling Approach

The copper particle size distribution of the aged catalysts was determined by TEM measurements in ref. [13] after aging at 523 K and an aging period of 0, 240, 480, 720 and 960 h, respectively. Since the catalysts, the aging setup and the aging process are the same as the ones presented in this work these characterization results can be used to describe the measured aging processes, e.g. in terms of numerical sintering models. In this work, Ostwald Ripening using the modified bond-additivity (MBA) approach, a classical coalescence model with a $D \approx r^{-4}$ dependence and a coalescence model employing random particle collisions are examined for the samples CZA1 and CZA2. A detailed description of the models is presented in chapter 5.7.

The MBA Ostwald Ripening model is formulated analogously to ref. [20] and has been validated with the data published for Pb on MgO therein. The log-normal fits of the TEM data for the fresh catalysts are discretized into 7.000 equidistant diameters. The system of coupled ordinary differential equations is solved with the Matlab solver ode23s. The contact angle between metal particle and support and vibrational frequency of an adsorbed atom on a particle are assumed constant as 90° and 10^{14} s^{-1} , respectively. Results are presented as bar graphs of 100 bars between 0 and 40 nm particle diameter.

In case of the random collision model, a dataset comprising 10.000 particles is generated based on the log-normal fits of the TEM particle size data for the fresh catalysts. It has been checked that the number of particles in the generated dataset is sufficient and higher numbers give virtually the same results despite a smaller statistical spread. For a coalescence event, two particles are chosen randomly, removed from the dataset and replaced by a particle of volume equivalent to the sum of the removed particles. This procedure is repeated until the chosen collision number is reached. The results are averaged over several datasets to minimize the statistical spread. To obtain the collision number that best fits the experimental TEM distributions, the sum of squares of the residuals of the discretized size distributions is calculated.

5.4 Results

5.4.1 Deactivation Behavior

An important prerequisite for the applicability of the power law deactivation model in 5.1 is that the apparent activation energy of the methanol formation does not change during the deactivation process. An exemplary Arrhenius plot for the deactivated catalysts is given in figure 5.1. A summary of the measured activation energies for the aging process at 523 K is presented in Table 5.3.

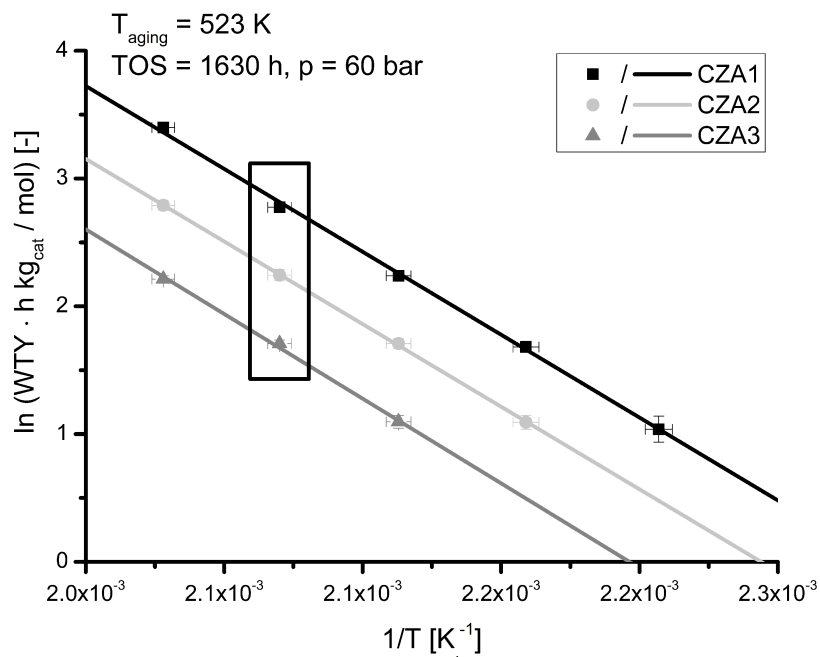


Figure 5.1: Arrhenius plot for the deactivated catalyst samples. The black box represents the conditions for the catalyst activity measurements.

Table 5.3: Activation energy EA before and after the aging process.

Catalyst	CZA1	CZA2	CZA3
$E_{A,0h}$ [kJ mol ⁻¹]	116.6±7.2	110.5±4.5	105.7±3.1
$E_{A,1630h}$ [kJ mol ⁻¹]	112.1±2.2	107.1±1.1	106.5±5.8

As the apparent activation energy of methanol formation during the deactivation process is constant within the error margin, the power law model can be applied

to describe the rate constant k_d of the deactivation process. This also supports the assumption that the active site type stays the same and only the site density decreases. An example of the deactivation behavior at 523 K is given in figure 5.2.

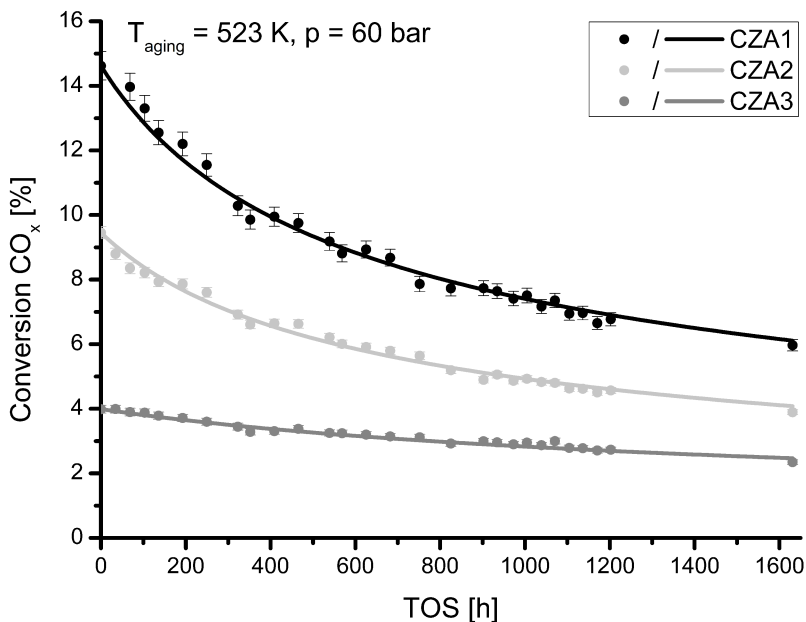


Figure 5.2: Deactivation behavior of the three different catalyst samples at 523 K. The straight lines represent the results according to the PLM fit.

All samples show a good methanol synthesis activity and compare well with other Cu/ZnO/Al₂O₃ systems reported in literature.[21, 22] In all cases the selectivity for methanol is beyond 99% and only traces of formaldehyde and methane are found during the equilibrium aging. The material balance is closed within 3% relative accuracy. Although CZA1 contains only 17% more copper than CZA2, the catalyst activity is increased by more than 50%. This is attributed to an optimal incorporation of Al³⁺ into the ZnO lattice, generating oxygen defect sites and acting as an electronic promotor.[23] The lower activity of CZA3 is a result of the catalyst microstructure, resulting from the ex-aurichalcite precursor phase. Here, the copper particles are strongly embedded in a ZnO matrix effectively blocking the Cu surface from contact with the gas phase. In contrast, the structure of CZA1 and CZA2 is represented by an intimate mixture of spherical ZnO and Cu nanoparticles. This leads to a very porous structure, which is easily accessible for the gas atmosphere. An exemplary image of the microstructure is presented in figure 5.3 and a detailed analysis of the catalyst microstructures is performed in ref. [13].

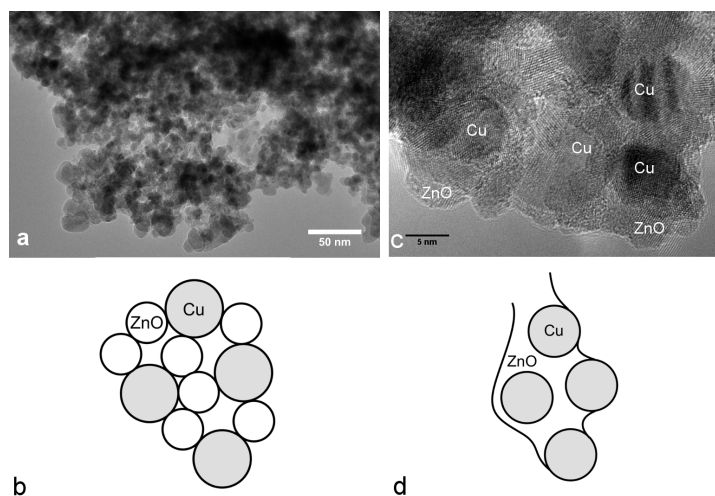


Figure 5.3: TEM images and exemplary representation of the microstructure of CZA1 and CZA2 (a, b) and CZA3 (c, d).

The influence of the aging temperature and the addition of water on the deactivation behavior is presented in figure 5.4. A summary of all determined rate constants of the catalyst deactivation is given in table 5.4.

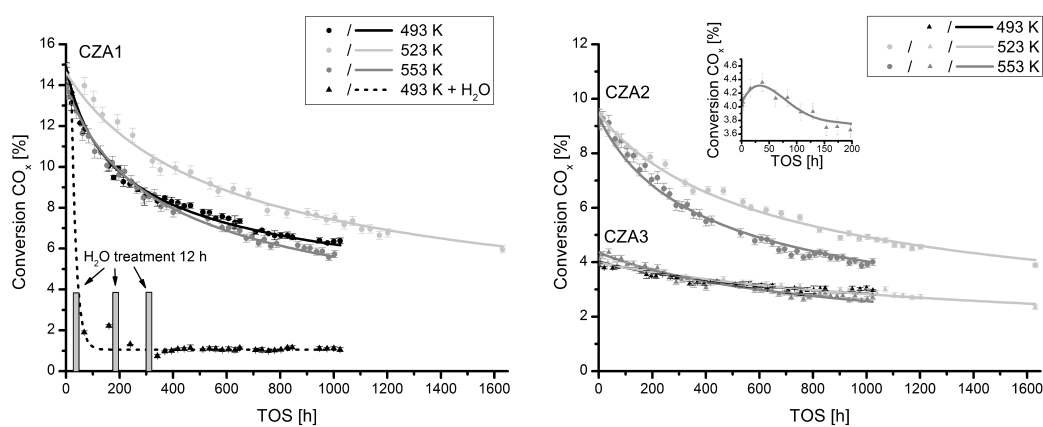


Figure 5.4: Influence of the aging temperature on the deactivation behavior. Straight lines represent the results according to the PLM fit. The inset in the right figure illustrates the transient activation behavior of CZA3 at 553 K.

Table 5.4: Rate constant and reaction order of catalyst deactivation according to the PLM fit.

Catalyst	T _{aging} = 493 K		T _{aging} = 523 K		T _{aging} = 553 K	
	k _d [h ⁻¹]	m	k _d [h ⁻¹]	m	k _d [h ⁻¹]	m
CZA1	4.29e-3	4	1.45e-3	3	2.62e-3	3
CZA2	n.d.	n.d.	1.34e-3	3	2.18e-3	3
CZA3	6.08e-4	4	4.95e-4	3	9.34e-4	3

During the aging period of 1630 h at 523 K CZA1 and CZA2 lose 60% of the initial activity, whereas CZA3 only loses about 40%. This strong deactivation is attributed to the severe conditions chosen for the aging periods. CZA1 and CZA2 show the same trend at 553 K deactivation temperature; in this case the deactivation rate is roughly doubled. Here, sample CZA3 shows an interesting formation behavior at 553 K, illustrated in the inset in figure 5.4. Whereas all catalysts exhibit a monotonic decrease in activity, CZA3 increases in the first 50 hours. Although the simple power law is not able to describe this behavior, it has no significant impact on the determined deactivation rate, as the activation only covers roughly 5% of the whole TOS. The reason for the initial rise in activity is not yet known; a possible mechanism may be the crystallization of the former amorphous Al₂O₃/ZnO matrix embedding the particles in the ex-aurichalcite phase. This could lead to a more porous matrix with copper particles that are better reachable for the gas phase atoms.

The short-term hydrothermal treatment of CZA1 leads to significant catalyst deactivation which underlines the strong influence of water on the deactivation behavior. To a small fraction, this process is reversible within a timescale of hours as can be seen after the last water addition period. However, this effect is minimal compared to the activity loss of more than 90% of the initial activity. Assuming pure sintering of metallic copper, the lowest deactivation rate is expected at 493 K. Nevertheless, the results show that at this temperature catalyst deactivation is almost as strong as at 583 K. This behavior may be explained by the higher water content during the aging process (see table 5.2).

The results of the reactive N₂O frontal chromatography measurements during the aging period are given in figure 5.5.

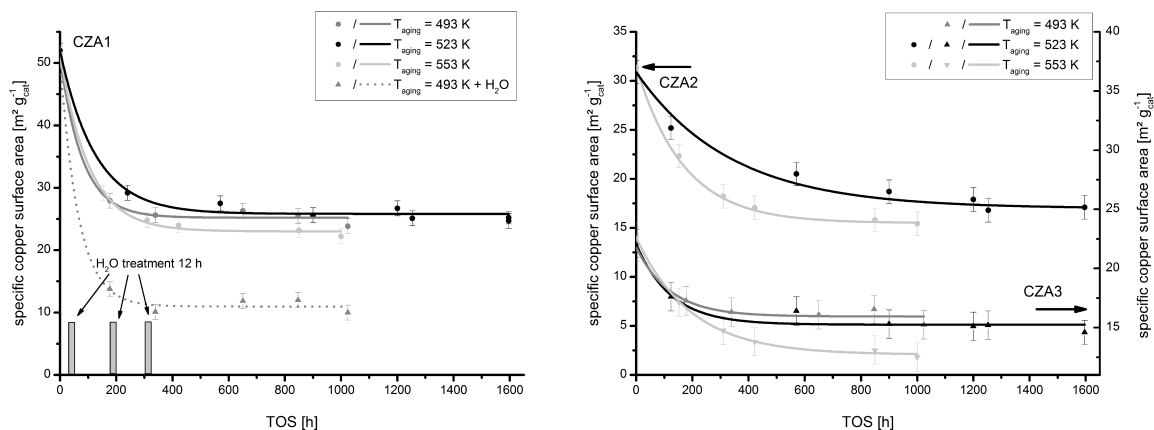


Figure 5.5: Results of the reactive N₂O frontal chromatography. The straight lines represent the trend in the specific copper surface area.

The trend in specific copper surface area is very similar to the development in catalyst activity during the aging period. Furthermore, the samples nicely resemble the results presented in ref. [13] which strengthens the assumption that the characterization data acquired therein can be applied to the presented catalysts.

5.4.2 Modeling Results

Selected results describing the copper particle size distribution of CZA1 and CZA2 in terms of a MBA Ostwald Ripening model and a random collision model are given in figure 5.6 and figure 5.7. Assuming the initial particle size distribution of the CZA1 sample, an adsorption energy of approximately 185 kJ mol⁻¹ between the mobile species and ZnO is required in the MBA Ostwald Ripening model if the exposed copper surface area is to be decreased to 75% of the initial value after 960 h. However, in this case the predicted particle size distribution is very narrow compared to the experimental data and overemphasizes the vanishing of small particles. The same trend can be observed in the classical $D \approx r^{-4}$ collision model given in the supporting information in chapter 5.7.

In contrast, the random collision model, which essentially states that the copper particles coagulate independent of the respective particle diameters, characterizes the sintering behavior of CZA1 and CZA2 very well.

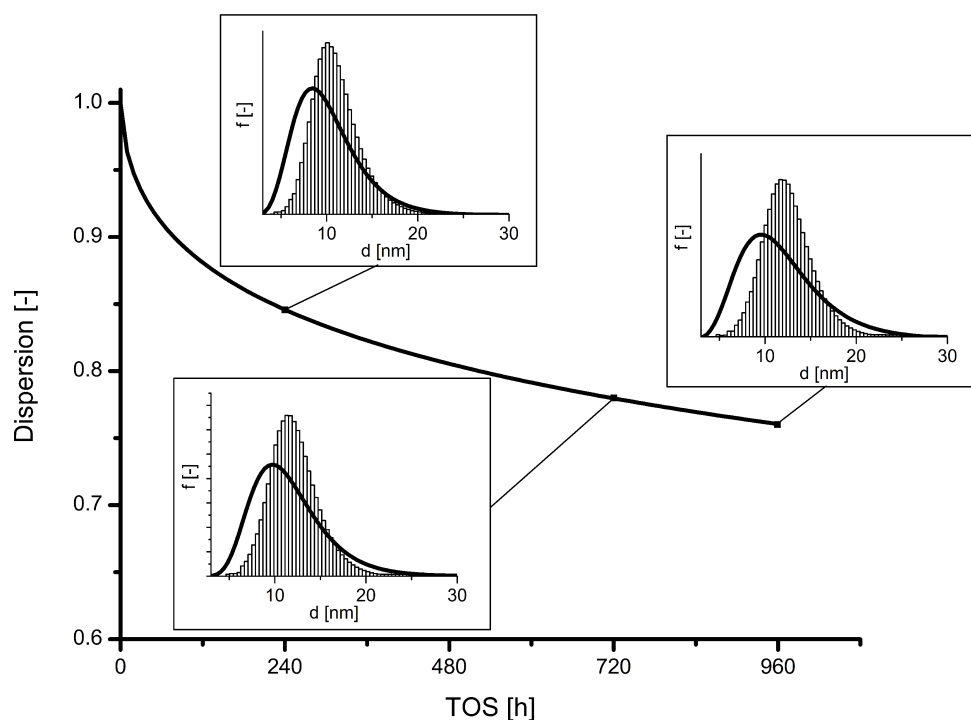


Figure 5.6: Relative dispersion and particle size distribution according to the MBA Ostwald Ripening model ($E_{\text{ads}} = 185 \text{ kJ mol}^{-1}$). The black line in the inset picture represents the measured distribution, whereas the gray bars represent the modelling result.

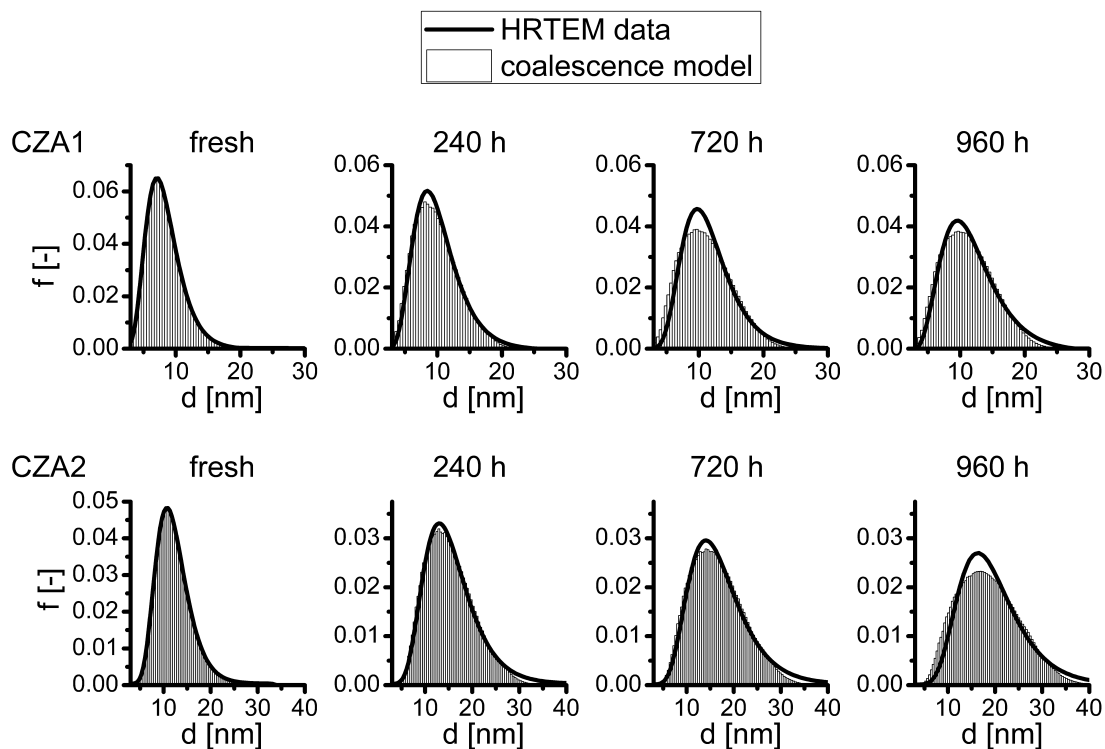


Figure 5.7: Particle Size Distributions according to the random collision model for CZA1 (top row) and CZA2 (bottom row).

5.5 Discussion

The catalyst deactivation can be described by a simple power law model of 3rd order for aging temperatures of 523 and 553 K and 4th order for an aging temperature of 483 K, respectively. To illustrate the deactivation behavior the parameterized power law is extrapolated to a TOS of 400 days and compared with literature values of catalysts aged under similar conditions. As presented in figure 5.8, the gathered data compares well with an industrial Cu/ZnO/Al₂O₃ catalyst presented by Skrzypek et al.[24] and very stable Cu/ZnO systems supported on SBA15 presented by Prieto et al.[12]. A similar exponential loss in activity has also been observed in the methanol steam reforming reaction over copper bases catalysts.[25] However, it should be noted that the presented catalyst samples were aged under specifically severe conditions, so that the described deactivation patterns do not represent the overall catalyst lifetime in industrial reactors. Although, the extrapolation of data should be generally considered with great caution, it underlined the big variety in the methanol synthesis catalyst stability: whereas the mentioned systems roughly retain 25% of their initial activity after 400 days TOS, other systems deactivate even more rapidly.

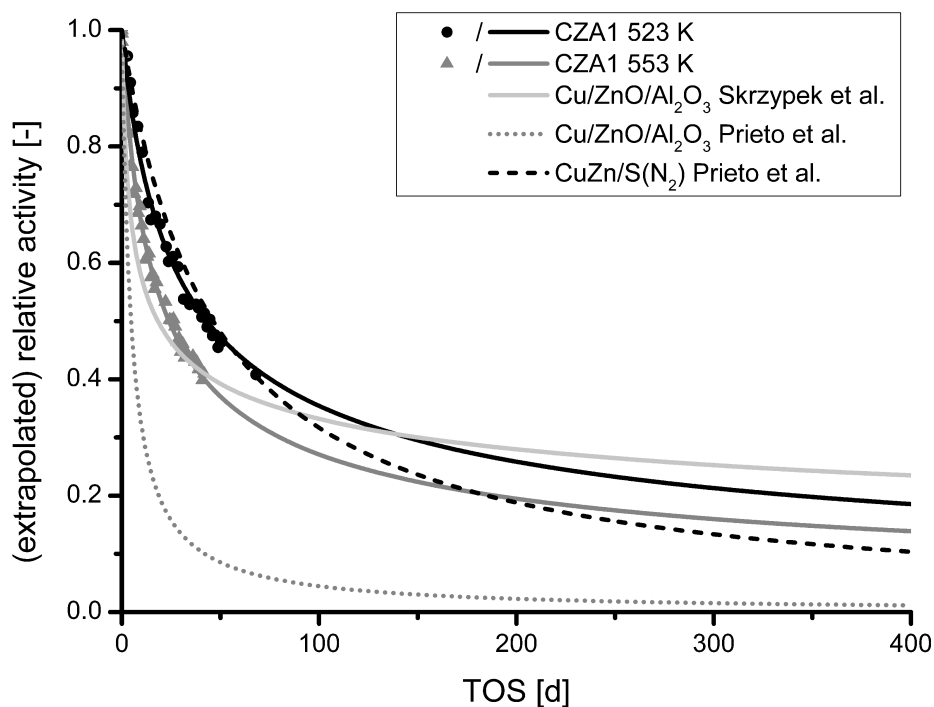


Figure 5.8: Comparison of selected deactivation models with our experimental data for CZA1 (dots and triangles) and the determined PLM fit (straight lines).

Another study by Kuechen et al. [26] on Cu/ZnO systems also reports a similar rapid deactivation which is accompanied by a loss in BET surface area which is not found in the presented systems. This underlines the influence of alumina as promotor not only increasing the ZnO_x defect concentration but also stabilizing the catalysts against degradation.[6, 27]

An analysis of the specific activity under the aging conditions employed is presented in figure 5.9 and shows that the aging temperature has no major impact on the activity per copper surface area ratio.

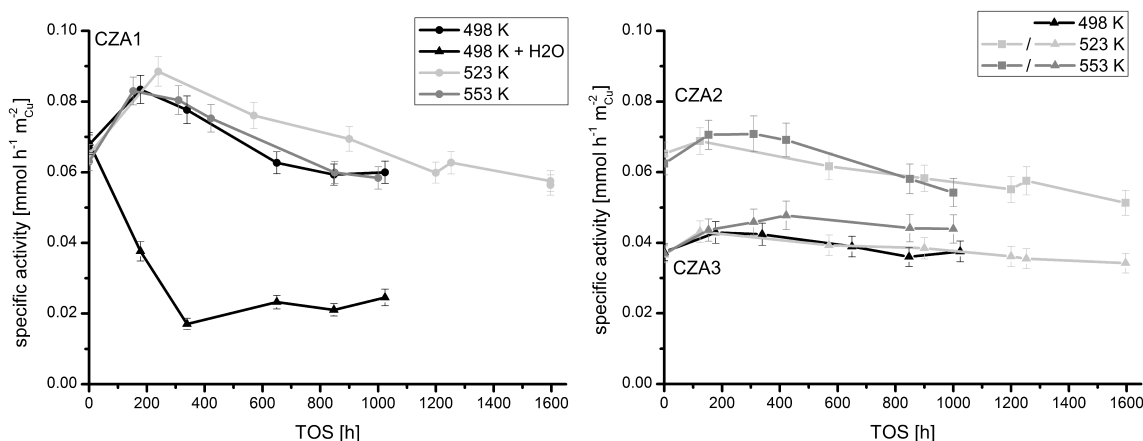


Figure 5.9: Specific catalyst activity in relation to the N₂O-RFC copper surface area.

After an initial formation period accompanied by an increase in specific activity, the specific activity drops for roughly the first 600 h and then reaches a slowly deactivating state. The strong initial increase in activity of CZA1 may be attributed to a drop in ZnO_x defect sites which are initially present due to the influence of the alumina incorporation into the ZnO_x framework.[23, 28] Due to the structural similarity of the precursor material it is not surprising that the specific activities of the deactivated CZA1 and CZA2 samples show a close resemblance.

When treating CZA1 with water, a significant drop in specific activity is noticed. This indicates that under hydrothermal conditions the catalyst undergoes structural changes and hence loses significantly copper surface area. Furthermore, the exposed copper surface is not that active for methanol synthesis anymore, which strongly hints to reduction of the Cu/ZnO interaction important for the catalytic activity. Previous studies by Kandmir et al. [29] suggested the formation of mobile ZnO_x species in such high performance catalysts, but also in model type catalysts mobile ZnO species were reported previously.[30] A reduction of the strong Cu/ZnO interaction could easily occur by retraction of mobile ZnO, which is supported by the observed crystallization

of ZnO and ZnAl₂O₄ in the presented catalysts during the deactivation period.[13] The hydrothermal treatment of CZA1 leads to a pronounced crystallization of ZnO and hence a loss of the intimate Cu/ZnO contact.

Changes in the Cu-Zn interaction may also be responsible for the deactivation behavior CZA3 identified by less copper particle sintering in the TEM analysis. Taking into account that the apparent activation energy for the methanol production is very similar to the one after the aging process, it is reasonable to assume that under the typical aging conditions presented here the nature of the active site(s) does not change. As poisoning of the catalysts was excluded from the experiments and the maximum temperature of 553 K is too low for bulk formation of brass, the deactivation achieved in this work results most likely from a reduction of the active site concentration by sintering of copper or a coverage of copper with excess ZnO.[29] In the very ZnO-rich CZA3 sample, this is mainly attributed to a strong embedding of the Cu particles in ZnO. In case of the less ZnO rich samples CZA1 and CZA2 the mobility of ZnO_x and the formation of bigger ZnO domains leads to a loss in Cu/ZnO interaction and random coagulation of the copper particles due to the depletion of the ZnO spacer material. This phenomenon leads to sintering of copper particles and has been analyzed in detail in ref. [13].

The results from Datye et al. [31] indicate that the discrimination of sintering mechanisms is not possible by only evaluating particle size distributions. However, it is noteworthy that sintering in case of the presented Cu/ZnO/Al₂O₃ catalysts seems to be independent of the copper particle radius. The result that the particle size distribution presented in figure 5.6 does not match the measured TEM particle size distribution is accordingly not to be taken as an argument in disfavor of Ostwald Ripening. As presented below for a coalescence mechanism and similarly also by Prieto et al. [12], the structure of the coprecipitated Cu/ZnO is expected to affect the evolving particle size distributions in terms of the pronounced influence of neighboring Cu particles separated by ZnO spacers. Nevertheless, there are some reasons, indicating that Ostwald Ripening of Cu is not the main sintering mechanism in ternary methanol synthesis catalysts:

1. According to TEM results, new twin boundaries are formed during the sintering of particles which is characteristic for an agglomeration mechanism.[13]
2. There is no trend observable that catalysts with a smaller particle sizes tend to sinter faster. In contrast, the sintering behavior is a strong function of the preparation and structure of the catalysts. Ex-aurichalcite type catalysts as CZA3 are characterized by Cu particles which are strongly embedded in a partially amorphous ZnO matrix. Those systems exhibit a distinct smaller surface area. However, they hardly sinter independent of the Cu particle sizes. The driving force for Ostwald Ripening (see supporting information in chapter 5.7) might

be influenced by a different ratio of the ZnO/Cu contact area than typically found in conventional catalysts. However, it seems unlikely that this phenomenon extinguishes the driving force. In fact, it indicates that there is a lack in mobility of individual atoms or molecules and those systems are stable because the embedment of Cu particles in the ZnO matrix prevents the particles from agglomeration.

Also the general inadequacy of the coalescence model for coprecipitated methanol catalysts is quite obvious since there is no plane support on which copper particles can diffuse and randomly coalesce according to their mobility. In contrast, copper particles are separated by ZnO particles of more or less of the same size. Consequently, the classical model fails in describing the observed sintering behavior of methanol synthesis catalysts in terms of both time dependence and particle size distribution (see figure 5.11). The particle size distributions are too narrow in the model as a result from the r^{-4} dependence of the particle diffusion coefficient. Since the sintering of small particles is highly favored over large particles, first selectively small particles should disappear. The probability for the formation of large particles resulting from coalescence of two large particles is low. In comparison to the experiment, however, the fraction of both small and large particles is systematically underestimated. This indicates that the mobility is either less affected by the radius than assumed or is not the critical factor, but the probability of two particles to sinter is predetermined by the microstructure of the catalyst. Assuming the probability of two particles independent of the radius and consequently equal for all particles, the particle distributions in Figure 6 can be derived. In particular, the description of formation period in the first 10 days is excellent. There is no tendency observable of small particles disappearing first. This observation is similar to that of Prieto et al. [12] who found that the introduction of local correlations in the classical Ostwald Ripening model improved the model predictions for Cu/ZnO constrained in a mesoporous SiO₂ support. Nevertheless, even in case of local correlations small particles tend to disappear first in classical Ostwald Ripening as well as in coalescence models which cannot be derived from the TEM observations used in this study

Since the observed sintering behavior strongly depends on the structure of the individual catalyst and less on physical, size-dependent properties or the distance between particles, the time-dependence of sintering cannot be predicted in the random collision model. However, the similarity of the time-dependent collision number presented in figure 5.10 is striking. This is especially interesting as the initial mean copper particle diameter of CZA2 is more than 50% larger as in CZA1 which would generate a significant difference in the size-dependent surface diffusion behavior.

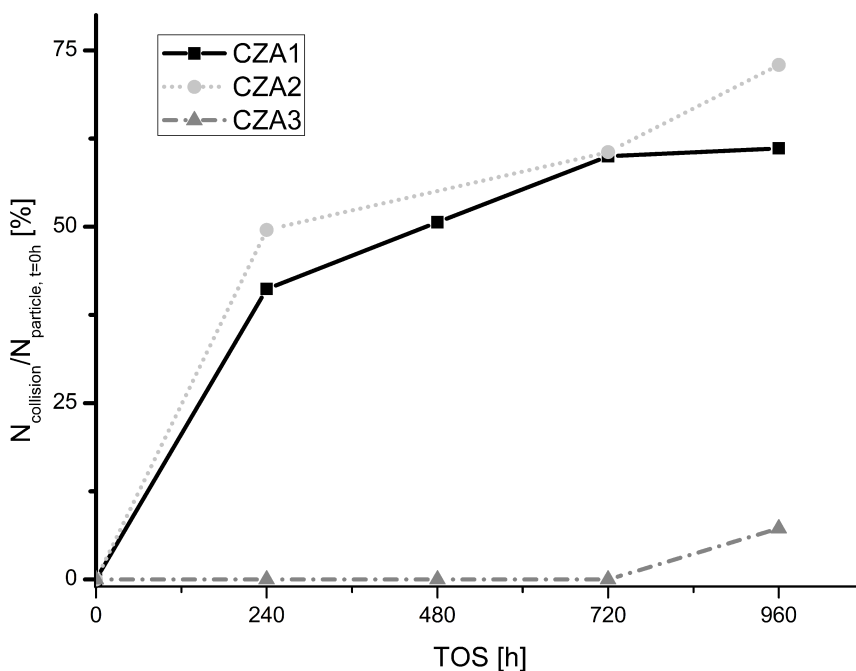


Figure 5.10: Time-dependent collision number according to the random collision model.

The assumption of random colliding copper particles in CZA1 and CZA2 is also highly consistent with the sintering model described in ref. [13] and underlines the possibility of quasi rigid copper particles coagulating following the loss of contact between Cu and the ZnO spacer between the particles. It should be noted that also the deactivation rate of CZA1 and CZA2 are quite similar despite the more than five times larger Al₂O₃ content of the latter one. This indicates that the stability may also be more attributed to the integration of Al³⁺ into the ZnO framework than the sheer abundance of alumina as "mineral" spacer agent.

5.6 Summary

The key aspects of this work can be presented as follows:

1. The deactivation behavior of three different methanol synthesis catalysts was systematically examined and characterized using an empiric power law equation.
2. The nature of the active site does not change under the typical conditions employed and the main deactivation mechanism is hence a reduction of active sites by sintering in case of ex-malachite type materials and increased coverage with ZnO in case of ex-aurichalcite catalysts. Furthermore, the stabilizing effect of alumina seems to be a function of the incorporation of Al³⁺ into the ZnO lattice.
3. The addition of water, even for a short period, does not only increase the sintering tendency but also permanently reduces the specific catalyst activity, possibly by segregating Cu/ZnO and hence reducing the SMSI effect needed for a high catalyst activity.
4. The sintering behavior of copper particles was modeled according to an Ostwald Ripening model and different collision models. It is found that the sintering behavior does not depend on the particle size, but rather follows a random collision of particles.

Owing to the time consuming measurements and many-sided possible error source of systematic long time experiments, the results discussed in this work only present a certain aspects of the deactivation mechanism of methanol synthesis catalysts. Also, it should be noted that the usefulness of the presented results for other systems depends on the similarity of the microstructure and should not be transferred to classical supported metal nano-particles. However, it underlines the necessity for detailed studies in order to unravel the processes happening during and influencing the deactivation behavior. Especially with respect to plant operation where the catalyst bed is aged differently along the reactor length, much more insight into the influence of water in the deactivation mechanism is needed. Our results support the findings that the key component of deactivation in methanol synthesis catalysts with the described microstructure is not the low thermal stability of the copper particles but the mobility of ZnO. Hence, more stable catalysts may also be obtained, when stabilizing the ZnO that functions as spacer in between the copper particles. The presented random-collision-coagulation model proved to be a versatile tool and the results encourage to use the model to analyze the sintering behavior of better catalysts for methanol synthesis.

5.7 Supporting Information

5.7.1 Ostwald Ripening

In general, two sintering mechanisms are distinguished: Ostwald ripening and coalescence. Driving force for the Ostwald ripening is the minimization of the chemical potential of the metal atoms. Since according to the Gibbs-Thomson relation the chemical potential of a metal atom in small particles is largely influenced by the surface energy, large particles are prone to increase in size while smaller particles shrink. Classically, bare metal atoms or molecular species are assumed as mobile species that according to the driving force tend to migrate from smaller to larger particles. As a common in basic models, this net flux results from a concentration difference of a size-specific equilibrium concentration of mobile species present around the particle and the mean-field concentration of mobile species assumed as constant on the oxidic support beyond a screening distance around the metal particles. This equilibrium concentration is smaller for larger particles and vice versa according to the chemical potential of a metal atom in a particle. The mean-field concentration of mobile species on the support is derived from mass conservation. A pioneering Ostwald ripening model was formulated by Wynblatt and Gjostein for the cases of so-called diffusion and interface control, see e.g. reference [20] for details. During the last years, Campbell and coworkers [20, 32, 33] have promoted the development of more sophisticated sintering models for nanoparticles motivated by the lack of the former models in terms of description of the chemical potential of metal atoms as a function of the particle size. Since the surface tension used in the Gibbs-Thomson equation in classical ripening models for calculating the chemical potential is a macroscopic property and assumed as independent on the radius, the modified bond-additivity (MBA) approach has been developed to simply derive an approximation of the chemical potential for a metal atom of a nanoparticle by counting the mean number of bonds per metal atom in a nanoparticle of a specific size. The differential equation for a particle size r can be formulated as

$$\frac{dr}{dt} = \frac{K}{r} \exp\left(-\frac{E_{tot}}{RT}\right) \left[\exp\left(\frac{E(r^*)}{RT}\right) - \exp\left(\frac{E(r)}{RT}\right) \right] \quad (5.3)$$

where r^* is the critical particle radius that is by definition in equilibrium with the mean-field concentration of mobile species, $E(r)$ is the size-specific difference of chemical potential related to a metal atom in a particle of infinite size according to the MBA-model, E_{tot} is the sum of all activation energies and K groups parameters that can be assumed as constant. The total activation energy is expressed as contribution from the

metal's bulk sublimation energy ΔH_{sub} , the diffusion activation energy of the mobile species on the oxide ΔH_m^s and the adsorption energy of a monomer on the support as

$$E_{tot} = \Delta H_{sub} - E_{ad}^s + H_m^s \quad (5.4)$$

Assuming that the diffusion activation energy of the mobile species can be approximated as $0.25 E_{ad}^s$ [20], the total activation energy can be formulated as

$$E_{tot} = \Delta H_{sub} - 0.75 E_{ad}^s \quad (5.5)$$

With these equations the adsorption energy needed for pronounced sintering rates energy can now be approximated. Assuming the initial particle size distribution of the CZA1 sample, an adsorption energy of approximately 185 kJ mol^{-1} is required if the dispersion is to be decreased to 75% after 960 h at an aging temperature of 523 K. This value now can be compared to published adsorption energies for Cu on ZnO. According to a DFT study by Meyer and Marx [34], adsorption energies for single Cu atoms on polar ZnO surfaces range between 166 and 276 kJ mol^{-1} for ideal O- and Zn-terminated polar ZnO surfaces. However, the adsorption energies are found highly dependent on coadsorbates and defect sites which drastically diminish Cu adsorption energies to 79 to 108 kJ mol^{-1} . With an adsorption energy of about 100 kJ mol^{-1} , Ostwald ripening is many orders of magnitudes too slow to account for the observed sintering and the model predicts virtually no sintering at all. Keeping the dependence of the sintering on the gas composition in mind, one might speculate about mobile species on ZnO that nevertheless might enable Ostwald ripening in reasonable rates.

5.7.2 Coalescence

In classical coalescence models for supported metal catalysts it is assumed that the metal particles diffuse on a plane oxidic support. The probability of a collision of two distinct particles is a function of their diffusion coefficients. More mobile particles tend to hit with higher probability and agglomerate. This behavior can be described using the Smoluchowski equation, where the first term stems from the collision of two crystallites whose sum of volumes is equivalent to the size of s while the second term describes the disappearance of a particle of size s due to collision to any other particle [35]:

$$\frac{df(s, t)}{dt} = \int_0^s D(s') f(s', t) f(s - s', t) ds' - \int_0^\infty [D(s) + D(s')] f(s', t) f(s, t) ds' \quad (5.6)$$

Key parameter here is the particle diffusion coefficient that determines both the rate of sintering and the evolution of the particle size distribution since the diffusion coefficient is classically assumed as function of the particle radius and hence determines the relative probability of a particle of size s to sinter in comparison to a particle of other volume. However, the dependence of the diffusion coefficient on the particle radius depends on the assumed mechanism and is an open discussion. The dependence of the diffusion coefficient on the radius is assumed as r^{-4} in ref. [35–37] and r^{-2} in ref. [38] for the diffusion of 3D particles on a 2D support or as r^{-2} in ref. [39] for diffusion of 2D clusters on a 2D support, for instance. Figure 5.11 illustrates the modeled particle size distributions for $D \approx r^{-4}$. Similarly to the Ostwald ripening model, the distributions are too narrow compared to the experimental ones.

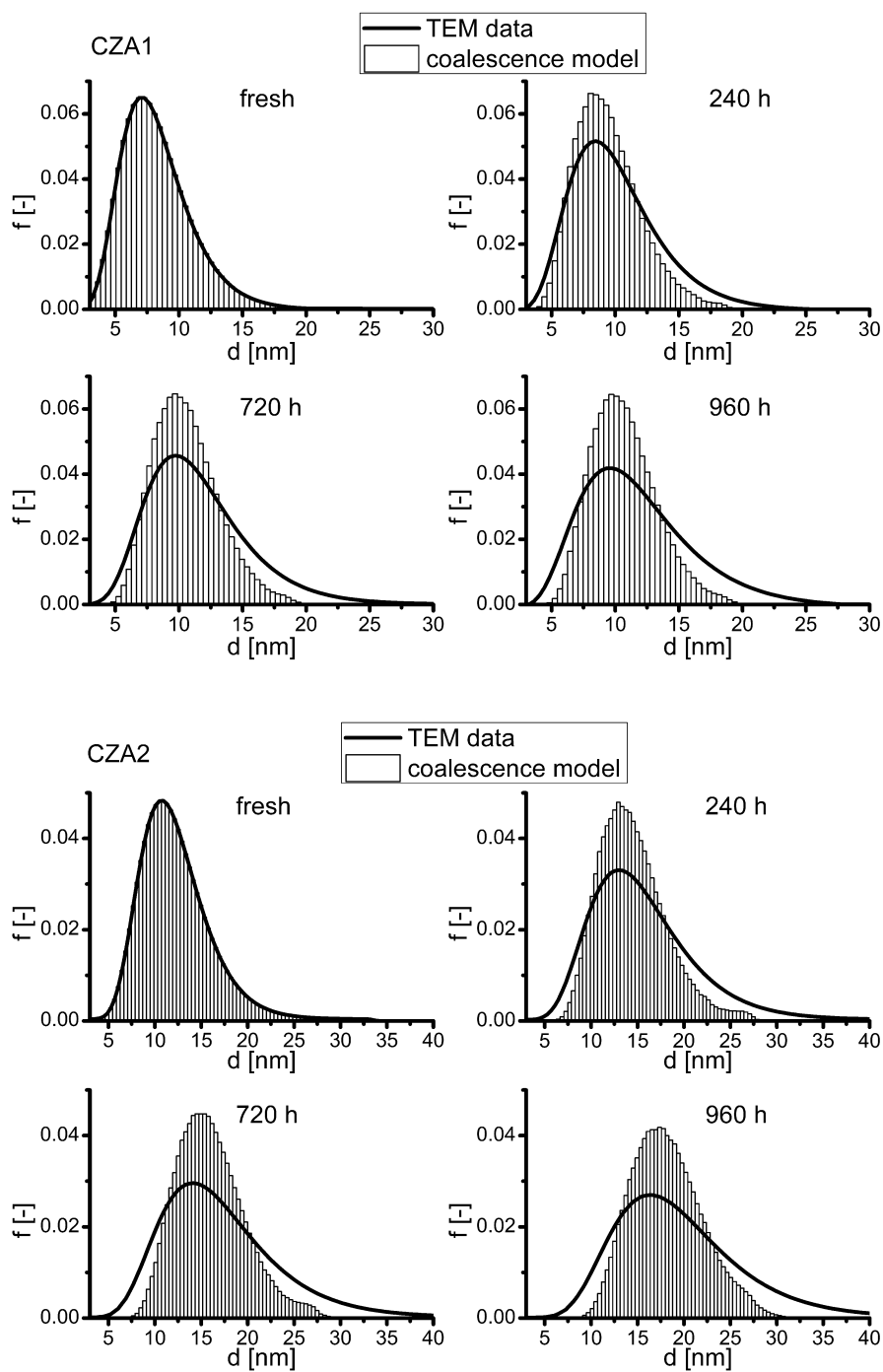


Figure 5.11: Particle Size Distributions according to TEM and classical coalescence model ($D \approx r^{-4}$) for CZA1 (top) and CZA2 (bottom).

References

- [1] R. Mallhotra, *Fossil Energy*, Springer, New York, **2012**.
- [2] G. A. Olah, A. Goeppert, G. K. S. Prakash, *Beyond Oil and Gas: The Methanol Economy*, Wiley-VCH Verlag GmbH & Co. KGaA, Weinheim, Auflage: 2. vollst. überarb. u. erw. Auflage, **2009**.
- [3] G. A. Olah, *Angew. Chem. Int. Ed.* **2013**, *52*, 104–107, DOI 10.1002/anie.201204995.
- [4] P. Forzatti, L. Lietti, *Catal. Today* **1999**, *52*, 165–181, DOI 10.1016/S0920-5861(99)00074-7.
- [5] C. H. Bartholomew, *Appl. Cat. A* **2001**, *212*, 17–60, DOI 10.1016/S0926-860X(00)00843-7.
- [6] M. V. Twigg, M. S. Spencer, *Top. Catal.* **2003**, *22*, 191–203, DOI 10.1023/A:1023567718303.
- [7] G. Hochgesand, *Ind. Eng. Chem.* **1970**, *62*, 37–43, DOI 10.1021/ie50727a007.
- [8] H. H. Kung, *Catal. Today* **1992**, *11*, 443–453, DOI 10.1016/0920-5861(92)80037-N.
- [9] M. R. Rahimpour, B. Moghtaderi, A. Jahanmiri, N. Rezaie, *Chem. Eng. Technol.* **2005**, *28*, 226–234, DOI 10.1002/ceat.200407062.
- [10] *Handbook of Heterogeneous Catalysis: Online*, (Eds.: G. Ertl, H. Knözinger, F. Schüth, J. Weitkamp), Wiley-VCH Verlag GmbH & Co. KGaA, Weinheim, Germany, **2008**.
- [11] T. W. Hansen, A. T. DeLaRiva, S. R. Challa, A. K. Datye, *Acc. Chem. Res.* **2013**, *46*, 1720–1730, DOI 10.1021/ar3002427.
- [12] G. Prieto, J. Zečević, H. Friedrich, K. P. de Jong, P. E. de Jongh, *Nature Materials* **2012**, DOI 10.1038/nmat3471.
- [13] M. B. Fichtl, J. Schumann, N. Jacobsen, W. Busser, M. Muhler, M. Behrens, R. Schlögl, O. Hinrichsen, *in preparation*.
- [14] P. L. Hansen, J. B. Wagner, S. Helveg, J. R. Rostrup-Nielsen, B. S. Clausen, H. Topsøe, *Science* **2002**, *295*, 2053–2055, DOI 10.1126/science.1069325.
- [15] M. Behrens, R. Schlögl, *Z. Anorg. Allg. Chem.* **2013**, *639*, 2683–2695, DOI 10.1002/zaac.201300356.
- [16] M. Behrens, I. Kasatkin, S. Kühl, G. Weinberg, *Chem. Mater.* **2010**, *22*, 386–397, DOI 10.1021/cm9029165.

- [17] O. Hinrichsen, T. Genger, M. Muhler, *Chem. Eng. Technol.* **2000**, *23*, 956–959, DOI 10.1002/1521-4125(200011)23:11<956::AID-CEAT956>3.0.CO;2-L.
- [18] M. B. Fichtl, J. Schumann, I. Kasatkin, N. Jacobsen, M. Behrens, R. Schlögl, M. Muhler, O. Hinrichsen, *Angew. Chem. Int. Ed.* **2014**, *53*, 7043–7047, DOI 10.1002/anie.201400575.
- [19] S. Kuld, C. Conradsen, P. G. Moses, I. Chorkendorff, J. Sehested, *Angew. Chem. Int. Ed.* **2014**, *53*, 5941–5945, DOI 10.1002/anie.201311073.
- [20] S. Parker, C. Campbell, *Phys. Rev. B* **2007**, *75*, DOI 10.1103/PhysRevB.75.035430.
- [21] S. Zander, E. L. Kunkes, M. E. Schuster, J. Schumann, G. Weinberg, D. Teschner, N. Jacobsen, R. Schlögl, M. Behrens, *Angew. Chem. Int. Ed.* **2013**, *52*, 6536–6540, DOI 10.1002/anie.201301419.
- [22] O. Martin, J. Pérez-Ramírez, *Catal. Sci. Technol.* **2013**, *3*, 3343–3352, DOI 10.1039/C3CY00573A.
- [23] M. Behrens, S. Zander, P. Kurr, N. Jacobsen, J. Senker, G. Koch, T. Ressler, R. W. Fischer, R. Schlögl, *J. Am. Chem. Soc.* **2013**, *135*, 6061–6068, DOI 10.1021/ja310456f.
- [24] J. Skrzypek, J. Sloczyński, S. Ledakowicz, *Methanol synthesis: science and engineering*, Polish Scientific Publishers, **1994**.
- [25] D. G. Löffler, S. D. McDermott, C. N. Renn, *J. Power Sources* **2003**, *114*, 15–20, DOI 10.1016/S0378-7753(02)00589-X.
- [26] C. Kuechen, U. Hoffmann, *Chem. Eng. Sci.* **1993**, *48*, 3767–3776, DOI 10.1016/0009-2509(93)80219-G.
- [27] M. Kurtz, H. Wilmer, T. Genger, O. Hinrichsen, M. Muhler, *Catal. Lett.* **2003**, *86*, 77–80–80, DOI 10.1023/A:1022663125977.
- [28] J. Schumann, T. Lunkenbein, A. Tarasov, N. Thomas, R. Schlögl, M. Behrens, *ChemCatChem* **2014**, *submitted*, DOI cctc.201402278.
- [29] T. Kandemir, F. Girgsdies, T. C. Hansen, K.-D. Liss, I. Kasatkin, E. L. Kunkes, G. Wowsnick, N. Jacobsen, R. Schlögl, M. Behrens, *Angew. Chem. Int. Ed.* **2013**, *52*, 5166–5170, DOI 10.1002/anie.201209539.
- [30] Y. Choi, K. Futagami, T. Fujitani, J. Nakamura, *Appl. Cat. A* **2001**, *208*, 163–167, DOI 10.1016/S0926-860X(00)00712-2.

- [31] A. K. Datye, Q. Xu, K. C. Kharas, J. M. McCarty, *Catal. Today*, Frontiers in Catalysis: A Molecular View of Industrial Catalysis Frontiers in Catalysis: A Molecular View of Industrial Catalysis **2006**, *111*, 59–67, DOI 10.1016/j.cattod.2005.10.013.
- [32] C. T. Campbell, *Science* **2002**, *298*, 811–814, DOI 10.1126/science.1075094.
- [33] S. C. Parker, C. T. Campbell, *Top. Catal.* **2007**, *44*, 3–13, DOI 10.1007/s11244-007-0274-z.
- [34] B. Meyer, D. Marx, *Phys. Rev. B* **2004**, *69*, 235420, DOI 10.1103/PhysRevB.69.235420.
- [35] M. J. J. Jak, C. Konstapel, A. van Kreuningen, J. Verhoeven, J. W. M. Frenken, *Surf. Sci.* **2000**, *457*, 295–310, DOI 10.1016/S0039-6028(00)00431-3.
- [36] F. Behafarid, B. Roldan Cuenya, *Surf. Sci.* **2012**, *606*, 908–918, DOI 10.1016/j.susc.2012.01.022.
- [37] P. J. F. Harris, *Int. Mater. Rev.* **1995**, *40*, 97–115, DOI 10.1179/imr.1995.40.3.97.
- [38] N. L. Wu, J. Phillips, *J. Catal.* **1988**, *113*, 129–143, DOI 10.1016/0021-9517(88)90243-6.
- [39] D. Kandel, *Phys. Rev. Lett.* **1997**, *79*, 4238–4241, DOI 10.1103/PhysRevLett.79.4238.

6 Counting of Oxygen Defects vs. Metal Surface Sites in Methanol Synthesis Catalysts by Different Probe Molecules

6.1 Abstract

Different surface sites of solid catalysts are usually quantified by dedicated chemisorption techniques from the adsorption capacity of probe molecules assuming they specifically react with unique sites. In case of methanol synthesis catalysts, the Cu surface area is one of the crucial parameters in catalyst design and was for over 25 years commonly determined using diluted N_2O . In order to disentangle the catalysts' components influence different model catalysts are prepared and characterized using N_2O , temperature programmed desorption of H_2 and kinetic experiments. It turns out that the presence of ZnO dramatically influences the N_2O measurements. This effect can be explained by the presence of oxygen defect sites which are generated at the Cu-ZnO interface and can be used to easily quantify the intensity of Cu-Zn interaction. It can be concluded that N_2O in fact probes the Cu surface plus the oxygen vacancies, whereas the exposed Cu surface area can be accurately determined by H_2 .

6.2 Methods and Results

Methanol counts among the most important basic chemicals and represents an important C1 building block for industrial chemicals. It is commonly produced by hydrogenation of carbon monoxide or carbon dioxide. In the typically used low pressure process over Cu/ZnO/ Al_2O_3 catalysts pressures ranging from 50 to 100 bar and temperatures of 483 to 563 K are employed.[1] Since methanol is a platform molecule and can in general be generated from sustainable hydrogen and CO_2 sources, it gathers rising attention as a renewable energy storage and carrier.[2]

Even today - 50 years after the commercial introduction of the Cu/ZnO/Al₂O₃ system - the nature of the active site(s) of methanol synthesis is still under heavy investigation and a vast amount of techniques is employed to elaborate the reaction mechanism and active centre of the methanol synthesis on copper.[3–6] This lack of understanding can be partially contributed to the strong interaction of the different catalyst components. Especially the role of zinc oxide is still under debate. The well known ZnO promotion of copper has been described by various mechanisms such as alloy material and structural support or a hydrogen reservoir providing adsorbed hydrogen to copper by spill-over.[7–10] Many promotional effects or the activity of pure ZnO in methanol synthesis have in some way been attributed to the reducibility of ZnO and the formation of oxygen vacancy sites and it was shown that the presence of oxygen defects is also a crucial factor for the methanol synthesis activity of pure ZnO.[5, 11, 12] In situ TEM and EXAFS studies have proven the formation of oxygen vacancy sites in ZnO depending on the reactive conditions over the catalyst. This behavior is specifically attributed to the Cu-ZnO interaction (SMSI effect) and the defect concentration is high enough to influence the copper particle morphology in model systems.[13–16] Recently Schott et al. [17] reported about the aplanar distortion of thin ZnO layers on copper, leading to a systematically less strongly oxidized Zn^{δ+}. In real catalysts an amorphous overlayer of partially reduced ZnO_x influencing the adsorption properties of copper is found covering the copper particles after the activation procedure and the resulting catalyst characteristics have been extensively studied.[14, 18] This can be seen as a precursor state to the partial formation of Cu-Zn surface alloys which in fact might be the driving force for the strong interaction. The complexity of the typical surface termination of Cu nanoparticles in common Cu/ZnO/Al₂O₃ catalysts as formed after reduction is shown in the high-resolution TEM image in figure 6.1.

From a structural point of view, it is not easy to decide if under working conditions the extent of ZnO reduction in such arrangement exceeds the observed Zn^{δ+}O_x-covered Cu state and dynamically reaches a true surface alloy state. However, from a functional point of view, the difference of both models seems rather small as they have in common the existence of partially reduced and thus oxophilic Zn^{δ+} atoms in a close neighborhood to metallic Cu sites. These Zn^{δ+} sites are thought to act as adsorption sites for CO₂ and reaction intermediates like formate, while the hydrogen is likely supplied from the metallic Cu sites. A similar bi-functional mechanism was also proposed for methanol synthesis on Cu/ZrO₂ catalysts with CO₂ being activated on the surface of the zirconia promoter.[19] These CO₂ adsorption centers in Cu/ZrO₂ were modeled at the Cu-oxide interface, where in case of Cu/ZnO oxophilic Zn^{δ+} sites can be expected.[20] It has been shown that the contact to Cu can promote the formation of oxygen vacancies in ZnO.[21]

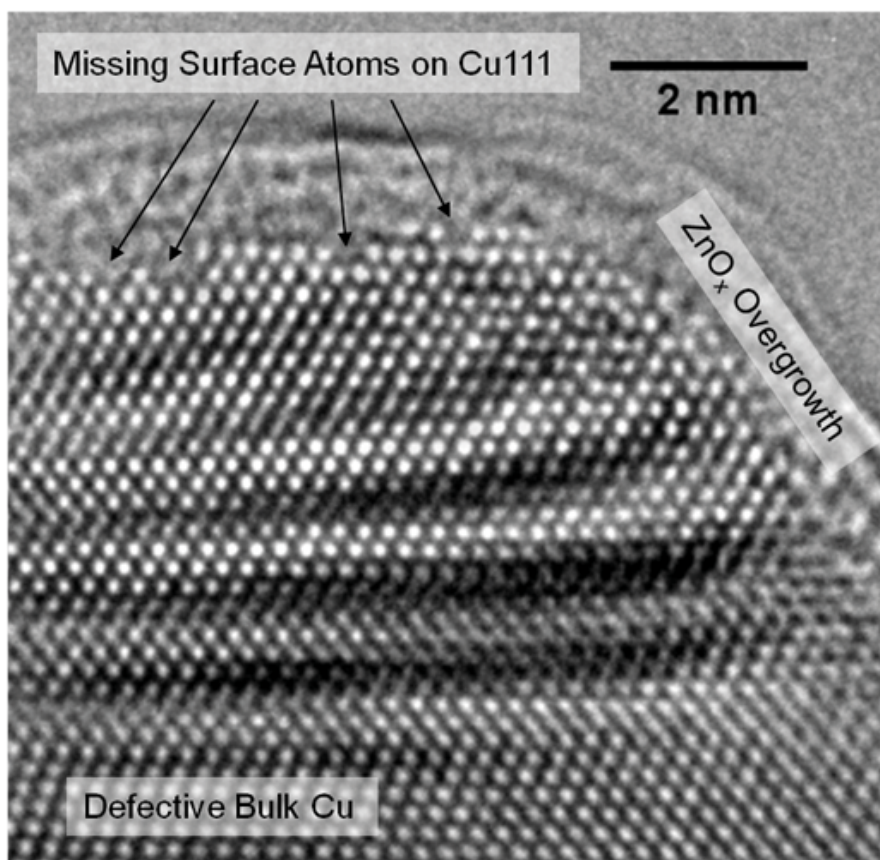


Figure 6.1: HR-TEM image of the surface termination of the ZnO_x-overgrown Cu nanoparticles in the catalyst CMZ1. The contrast fluctuations seen in the bulk of the Cu particle are Moiré fringes arising due to partial overlapping with other particles.

Alternatively, functionally similar oxophilic Zn sites can be modeled by inserting metallic surface Zn atoms on Cu defect sites.[5]

The existence of such oxophilic sites due to ZnO reduction creates an inherent problem when looking at the "classic" characterization of methanol synthesis catalysts by reactive nitrous oxide frontal (N₂O-RFC) or pulse chromatography which has been performed for over 25 years in order to quantify the copper surface area.[22] Especially the assumption that N₂O specifically oxidizes the copper surface and ignores the partially reduced ZnO_x is questionable. This study investigates the influence of ZnO on the copper surface area measured by N₂O-RFC and hydrogen temperature programmed desorption (H₂-TPD) on different Cu/ZnO/Al₂O₃, Cu/ZnO, Cu/MgO and Cu/ZnO/MgO catalysts. It unravels the significant bias which is introduced by the oxidation of ZnO_x sites using H₂-TPD as a complementary characterization method which provides a very selective, sensitive and

accurate way of describing the exposed copper surface area, i.e., the copper surface area not covered by ZnO_x species.[13]

In order to shed light on the interplay of exposed copper surface area, partially reduced zinc oxide and apparent N_2O -RFC area different model catalysts are prepared and characterized (Supporting Information 6.3.1). With the purpose to elucidate the influence of the reducible ZnO component, also Al_2O_3 and MgO were studied as alternative, irreducible structural promoters. Table 6.1 gives an overview of the systems employed and their composition and BET surface areas. To study the effect of ZnO , a ZnO -impregnation was applied to the Cu/MgO system using different synthetic procedures.

Table 6.1: Compositions and BET surface areas of the catalysts used.

Sample	C/X ^[a,b]	S _{BET} ^[c]	Sample	C/X ^[a,b]	S _{BET} ^[c]
C	100/-	15	CMZ1	79/16/5 ^[d]	94
CA1	20/80	100	CMZ2	79/16/5 ^[d]	90
CA2	87/13	70	CMZ3	67/29/4 ^[d]	121
CM1	83/17	100	CZA1	43/49/8	78
CM2	70/30 ^[d]	99	CZA2	58/26/16	74
ZA	-/84/16	78	CZA3	70/28/2	118

[a] Cu, Zn, Al, Mg = C, Z, A, M [b] molar, determined by ICP & XRF [c] calcined precursor, $\text{m}^2\text{g}_{\text{cat}}^{-1}$ [d] nominal composition

After activation of the catalysts in a glass lined single-pass fixed-bed reactor (Supporting Information 6.3.2) multiple H_2 -TPD spectra are gathered at heating ramps of 4, 6 and 10 K min^{-1} (Supporting Information 6.3.3). Next, the N_2O copper surface area is determined using the same catalyst at 308 K, 1 bar pressure using N_2O (1%) in He (Supporting Information 6.3.4). A mean copper surface density of $1.47 \cdot 10^{19}$ atoms per m^2 is used for converting the measured amount of copper into specific surface area. Activity measurements of the Zn-containing catalysts are performed after the H_2 -TPD and N_2O -RFC measurements (Supporting Information 6.3.2).

Correlating the hydrogen adsorption capacity and N_2 -evolution during the N_2O -RFC - which should be proportional to the copper surface area according to both methods - reveals the heavy bias which is introduced by ZnO . This is shown in figure 6.2.

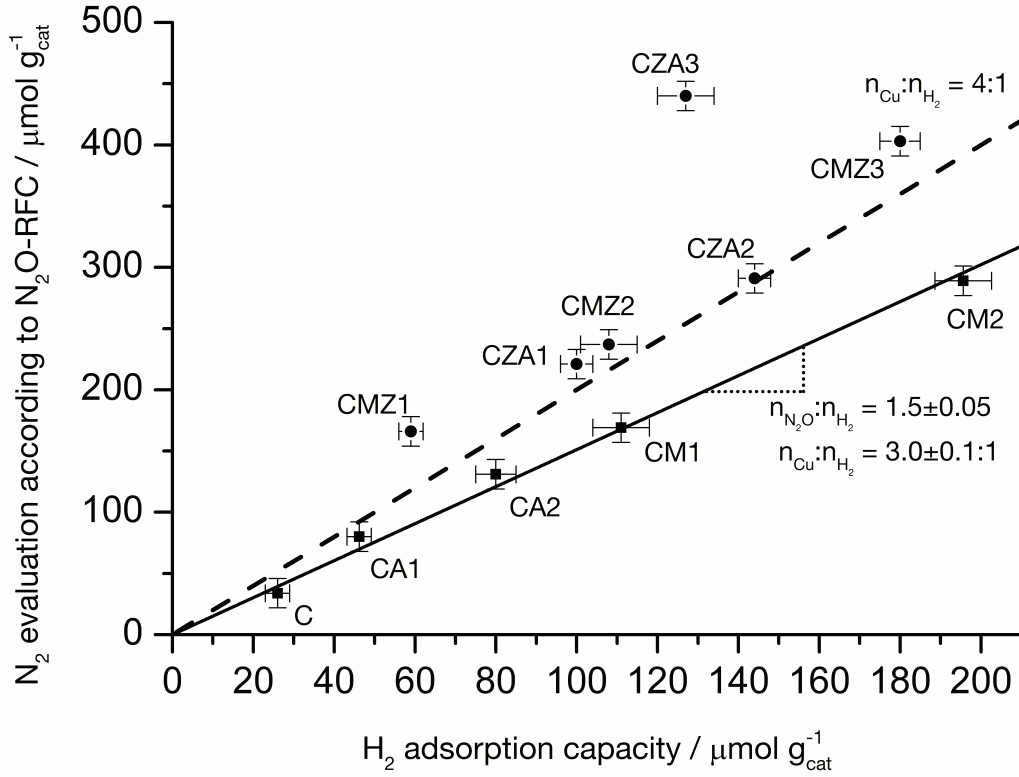


Figure 6.2: Correlation of the H₂-TPD and N₂O-RFC results.

The N₂O surface area of polycrystalline Cu agrees well with published data and the H₂-TPD area of the CA-systems matches with data published by Muhler et al. reasonably well.[5, 23] Assuming the formal oxidation of the exposed copper surface on Zn-free samples by N₂O to Cu₂O, the Cu:H₂ ratio can be determined using equation 6.1 and the value of the decomposed N₂O per adsorbed H₂. This ratio $n_{N_2O} : n_{H_2}$ is given by the slope of the solid line in figure 6.2.

$$\frac{Cu}{N_2} = 2 \frac{n_{N_2O}}{n_{H_2}} \quad (6.1)$$

A Cu:H₂ ratio of $3.0 \pm 0.1 : 1$ is obtained for the Zn-free materials. This experimental value mismatches the classically assumed 4:1 ratio, which is commonly deduced from UHV studies and described with a $\frac{1}{2}$ monolayer (ML) coverage of copper.[24] However, the formation of a $\frac{2}{3}$ ML coverage, which corresponds with the measured Cu:H₂ ratio, has been observed at higher H₂ exposure and theoretically studied in detail.[25–27] These

findings are also in line with the formation of ordered $1/3$ ML and $2/3$ ML adsorption structures during dissociative hydrogen adsorption on other fcc type metals.[28] The Cu/H₂ ratio is independent of the irreducible structural promotor and copper particle size. It also is in very good agreement with the BET surface area ($3.1 \text{ m}^2 \text{ g}_{\text{cat}}^{-1}$) of the activated sample C. The fact that even the low-surface area polycrystalline copper sample C nicely matches the H₂-N₂O correlation underlines the high sensitivity and precision which is obtained using H₂-TPD. The Zn-containing catalysts show a non-linear behavior where the majority roughly follow a Cu:H₂ ratio of 4:1 (dashed line in figure 6.2). Generally, all Zn-containing systems yield a significant higher N₂O-copper surface area than would be expected from the corresponding H₂-TPD experiments. According to the concept of reduced ZnO_x on top of the particles, this can be explained by the overconsumption of N₂O by oxidizing partially reduced ZnO_x. Furthermore, the ZnO_x layer is not necessarily of a monolayer type and de-wetting of previously covered copper upon oxidation of ZnO_x has to be considered.

In case of H₂-TPD measurements it is reasonable to say that hydrogen desorption from ZnO_x species is not observed within the experimental window which is supported by the impregnation experiments (vide infra). In general the position of the H₂-TPD signal is sensitive to the adsorption enthalpy and in case of the examined copper catalysts well aligned with the desorption signal of metallic copper. The difference in measured N₂O-surface area and corresponding theoretical N₂O-surface area according to the H₂-TPD quantifies the amount of over-oxidation and hence oxophilic Zn^{δ+} sites in ZnO_x.

Although the ZA sample exhibits a comparable BET surface area, the H₂-TPD and N₂O-RFC measurements do not show any significant signals in the specified experimental window after activation. This supports the assumption that the high amount of measurable defect sites stems from the copper zinc interaction and is not introduced by the sheer presence of ZnO. The extent of this interaction will be promoted by an initially high inter-dispersion of both phases, which is a function of the catalyst preparation. Thus, a strict linear behavior in case of the Zn-containing catalysts is not expected a priori.

Recently Behrens et al. presented a systematic study about the homogeneous incorporation of the different metals in the methanol synthesis catalysts and presented a highly active system with an optimized incorporation of Al³⁺ in the ZnO phase, leading to a strong defect structure in ZnO_x. [29] The analogously to this publication prepared sample CZA3 nicely confirms this behavior, as the determined defect concentration is more than 100% higher than in the other conventional CZA and CMZ systems. Furthermore, the impregnation experiments of the CM samples support these findings. Normally a drop in metal surface area of the activated impregnated samples should be expected, as a ZnO_x overlayer is formed over the copper particles blocking them from chemisorption.[10] In

case of the presented CMZ samples this is only true for the H₂-TPD measurements, whereas the N₂O-surface area even increases in comparison with the corresponding CM precursors. The results highlight the critical role of catalyst synthesis for the intensity of Cu-Zn interaction. The ZnO-impregnation of the calcined pre-catalyst (CM1 → CMZ1) leads to heavy blocking of half of the Cu surface area detected by the decrease in H₂ capacity and only a low degree of Cu-Zn interaction indicated by the little increase in N₂O capacity. Contrarily, if impregnation is done already on the co-precipitated catalyst precursor (CM1 → CMZ2 and CM2 → CMZ3), a much lower loss in Cu surface area and a substantial increase in N₂O capacity indicative for an intimate Cu-Zn interaction is observed.

The microstructure of the CZA catalysts was additionally characterized by TEM. As observed previously, the Cu particle shape can be described by a pseudo-spherical with an oxide matrix that spatially separates the individual nanoparticles. Based on a statistical Cu particle size evaluation, a theoretical maximal exposed Cu surface area can be calculated assuming that the particles were round and completely unsupported (see table 6.2). This value exceeds the probe gas derived surface areas in all cases, which is reasonable considering that a fraction of this hypothetical surface area must be present as interface to the stabilizing oxide matrix. A microstructural model of the catalyst in relation to the probe gas chemisorption capacities including the insensitivity of hydrogen toward Cu-ZnO interaction is discussed in the supporting information.

Table 6.2: Specific copper surface areas (SSA) and defect concentrations in SSA equivalents. (n.d. = not determined)

Sample	max. SSA _{TEM} ^[a]	SSA _{H₂-TPD} ^[b]	SSA _{N₂O-RFC} ^[b]	O defects ^[b]
CZA1	21.7	12.3	18.1	5.8
CZA2	27.9	17.7	23.8	6.1
CZA3	49.3	15.6	36.1	20.4
CMZ1	n.d.	7.1	13.6	6.5
CMZ2	n.d.	12.9	19.4	6.5
CMZ3	n.d.	22.1	33.0	11

[a] determined as described in the supporting information [b] mass based on calcined precursor, [m²g_{cat}⁻¹]

The specific activity evaluation of the Zn-promoted catalysts in figure 6.3 reveals that there is neither a direct correlation between the H₂- or N₂O-copper surface area and the catalyst activity nor between the catalyst activity and amount of oxophilic sites generated by ZnO. The latter one is estimated from the difference of the N₂O-RFC surface area and real copper surface which is calculated using the H₂-TPD data (see Supporting Information 6.3.4). According to the data, without optimization of the

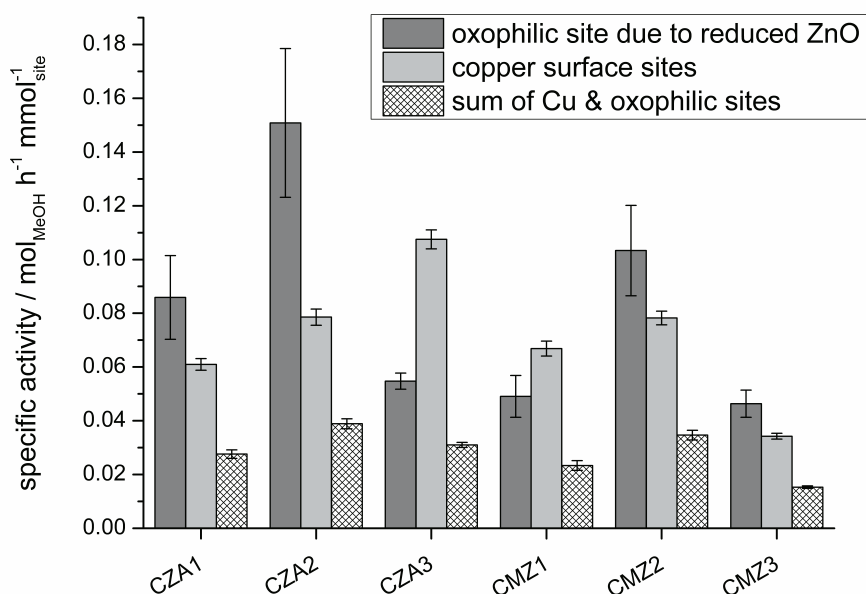


Figure 6.3: Specific activity of the different catalysts depending on the site type.

irreducible structural support (CZA3) this amount is almost constant independent of the preparation technique and Zn content. This implies again the Cu-Zn interaction as origin. Table 6.2 gives an overview of the determined specific surface areas.

The missing direct correlation between surface area and activity is not surprising and has been reported before, as the active site of the methanol synthesis is not considered to be metallic copper or the vacancy sites themselves, but a combination of multiple factors.[5, 10, 30] Interestingly with exception of CMZ3, there is a relationship between the N_2O -RFC surface area and the activity data, which suggests that the N_2O -RFC - despite the conceptual problem - can be used to characterize and evaluate many methanol synthesis catalysts. This trend has been reported in many literature reports, but was often misinterpreted as linear relationship between Cu surface area and activity to conclude structure-insensitivity of methanol synthesis on Cu/ZnO-based catalysts. In case of the highly active catalyst CZA3, it was shown that oxygen vacancies can in fact account for more than 50% of the N_2O -RFC capacity. This result shows that recent progress in catalyst development is not necessarily related to further increase in Cu surface area, but that great potential lies in the design of the Cu-Zn interaction. It furthermore strongly suggests that N_2O -derived surface areas should not be used to calculate TOFs of Cu/ZnO-based catalysts. While the N_2O capacity is an intrinsic

and catalytically important property, it does not (only) represent the amount of metal surface sites, which can be better quantified by H_2 chemisorption.

In summary, we are able to show that the presence of ZnO introduces a heavy bias in the determination of copper surface area using N_2O -RFC whereas both the N_2O -RFC and H_2 -TPD characterization methods lead to well matching results in absence of ZnO. Based on these measurements and recent findings about the nature of the Cu-ZnO interaction we propose, that an over 25 years established method for the characterization of the surface area of methanol synthesis catalysts does in fact not only describe the copper surface area, but also the oxygen defects which are present at the copper zinc interface. Although, the N_2O -RFC has often proved to be characteristic for the description of activity-structure relationships, it draws a misleading picture in terms of functional relationships in the catalysts and might lead to false assumptions for the mechanistic description and understanding. We are able to show that quantitative measurement of ZnO_x oxygen vacancies in methanol synthesis catalysts is possible by combining H_2 -TPD and N_2O -RFC measurements. As both measurements can easily be done in situ in a fixed-bed reactor setup, this greatly enhances the possibility of systematic studies on methanol synthesis catalysts. With little adaption, these measurements can be extended to other important catalytic systems with a pronounced SMSI effect like many group VIII metals supported on reducible transition metal oxides.

Experimental Section

The catalysts C, CA1-2, CZA1-3, ZA, CM1-2, and CMZ1-3 were produced by coprecipitation following literature recipes (see Supporting Information 6.3.1). The catalyst activity and the copper surface area according to H_2 -TPD and nitrous oxide reactive frontal chromatography (N_2O -RFC) are determined in a glass-lined single-pass fixed-bed reactor described in the Supporting Information 6.3.2. A detailed description of the procedures for the activity tests, N_2O -RFC and H_2 -TPD measurements is given in the Supporting Information 6.3.2, 6.3.3 and 6.3.4.

6.3 Supporting Information

6.3.1 Catalyst Preparation and Characterization

The catalysts C, CA2, ZA, CZA1 and CZA2 are produced by coprecipitation of the metal nitrates at a constant pH of 7 and temperature of 333 K following the recipe presented in ref. [31]. CZA3 is a reproduction of the catalyst described in previous work and detailed characterization data can be found therein and in a forthcoming publication.[29] The synthesis procedure is also based on co-precipitation using the concept of the industrial catalyst, which has been recently reviewed in detail elsewhere.[32] In brief, aqueous nitrate solutions of the metals in a Cu:Zn = 70:30 ratio with additional 3 mol% of Al were co-precipitated at a constant pH of 6.5 using sodium carbonate as precipitating agent. The co-precipitate was aged in the mother liquor at 338 K to crystallize a substituted malachite precursor phase, $(\text{Cu,Zn})_2(\text{OH})_2\text{CO}_3$. The precursor was calcined in air at 603 K to yield a CuO/ZnO:Al pre-catalyst with an intimate mixture of the oxides.

The Cu/MgO catalysts labeled CM were produced accordingly, but at a constant pH of 9 to completely precipitate the Mg^{2+} ions. The Cu-to-Mg ratio was 80:20 (CM1) or 70:30 (CM2), allowing co-precipitation of a phase-pure Mg-substituted malachite precursor, $(\text{Cu,Mg})(\text{OH})_2\text{CO}_3$, and subsequent transformation into a uniform material upon calcination and reduction. The follow-up impregnation of the CM catalysts with Zn-citrate to yield CMZ catalyst with a ZnO loading of 5 wt.% was done either on the malachite-like precursors of CM1 and CM2 (CMZ2 and CMZ3) or on the calcined CuO/MgO pre-catalyst of CM1 (CMZ1). In the latter case the catalyst was recalced at 563 K. The resulting nominal molar ratios of the catalysts are given in Table 6.3. The catalysts CM1 and CMZ1 are identical or reproductions of the catalysts already described in previous work.[10] The Cu/ Al_2O_3 catalyst CA1 was co-precipitated from a Cu:Al = 20:80 solution at pH 8, washed and calcined at 603 K. Table 6.3 provides an overview of selected samples used in this study and reports the internal FHI sample database numbers that should be used in future correspondence to facilitate communication.

The metal content of the calcined C, CA2, ZA and CZA1-2 precursors is analyzed by ICP-OES (SpectroFlame FTMOA81A, Spectro Analytical Instruments). Using this method, the samples are also checked for the absence of sodium and potassium impurities. Prior to the analysis, the samples are dissolved in boiling aqua regia, inspissated and diluted with 1 M HNO_3 . Those samples listed in table 6.3 have been investigated by X-ray fluorescence (XRF) using a Bruker S4 Pioneer x-ray spectrometer.

Nitrogen physisorption of the calcined precursors is measured at 78 K in a NOVA 4000e Surface Area & Pore Size Analyzer (Quantachrome Instruments). Prior to analysis, all

Table 6.3: Sample overview and database numbers of selected catalysts.

Label	Metal composition (nominal, molar)	Precursor	Calcined
CZA3 ^[a]	Cu/ZnO/Al ₂ O ₃ (70:28:2)	14328	15018
CM1 ^[b]	Cu/MgO (80:20)	9278	15882
CM2 ^[c]	Cu/MgO (70:30)	15316	15883
CMZ1 ^[d]	Cu/MgO/ZnO (79:16:5)	9278	13537
CMZ2 ^[e]	Cu/MgO/ZnO (79:16:5)	9278	13192
CMZ3 ^[f]	Cu/MgO/ZnO (67:29:4)	15316	16180
CA1	Cu/Al ₂ O ₃ (20:80)	13560	16090

[a] Reproduction of ref. [29] [b] Precursor identical to ref. [10], calcination reproduced

[c] Analogous to CM1 besides composition [d] Precursor identical to ref. [10], impreg-

nation reproduced on calcined catalyst [e] Precursor identical to ref. [10], impregnation

was done on co-precipitated precursor [f] Precursor identical to CM2, impregnation

was done on co-precipitated precursor

samples are outgassed under vacuum at 523 K for 3 h. For analysis of the BET surface area ten evenly spaced points in the pressure region from 0.05 to 0.3 bar are used.

For high resolution TEM investigation shown in figure 6.1 and figure 6.9c,d, a FEI Titan Cs 80-300 microscope operated at 300 kV, equipped with a FEG, Gatan Tridiem Filter was used. Spherical aberrations were corrected by use of the CEOS Cs-corrector reaching an information limit of 0.8 Å. The particle size evaluation leading to the TEM-based Cu surface area estimations given in table 6.2 was based on images such as shown in figure 6.4, which were taken on A Philips CM200FEG microscope operated at 200 kV. The high-resolution image shown in figure 6.9a was taken on the same machine and processed to obtain the power spectra which were used to measure inter-planar distances and angles for phase identification. For all measurements the reduced samples (at 523 K for 30 min in 5% H₂/Ar) were transferred via a glovebox to the microscope using a vacuum transfer holder to exclude the contact to air.

Based on a statistical evaluation of the Cu particle sizes of several images such as shown in figure 6.4a-c, the particle size distribution (figure 6.4d) and the average volume weighted Cu particle sizes for CZA1, CZA2 and CZA3 were determined as 11.9, 13.4 and 8.9 nm, respectively. These values have been used to calculate the hypothetical maximal Cu surface area given in table 6.2 based on the elemental compositions and assuming a spherical shape and bulk density of copper.

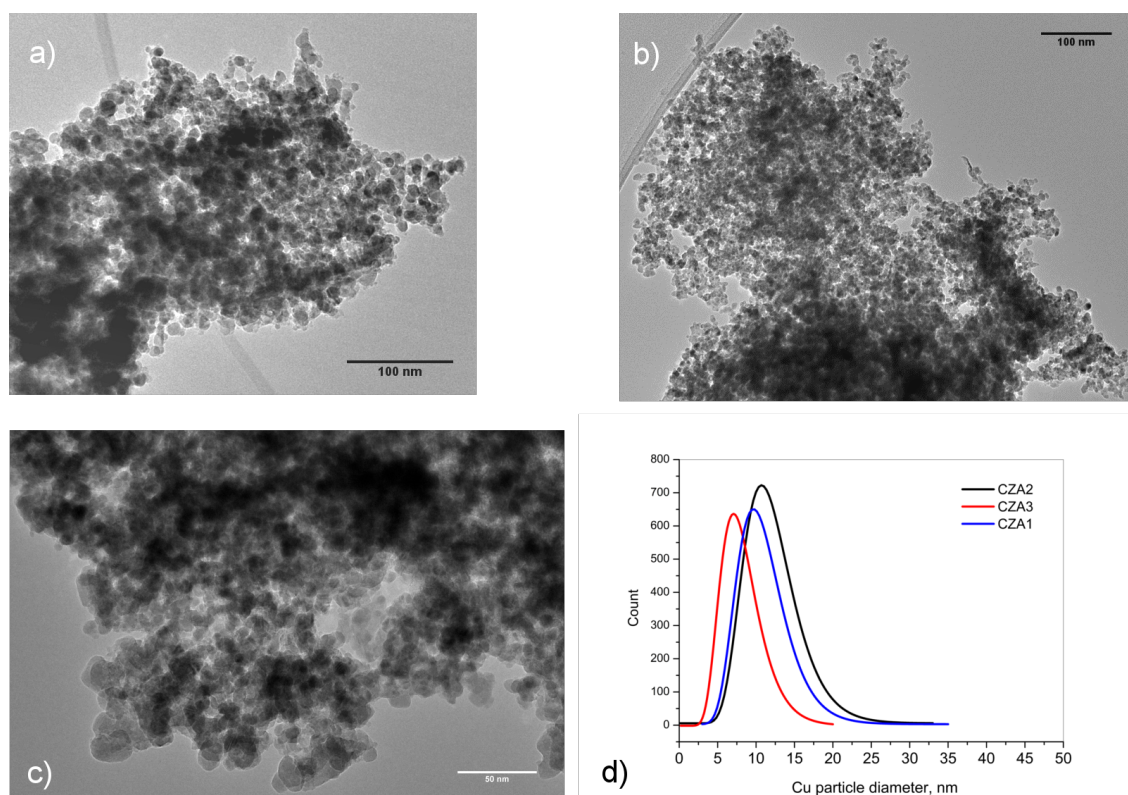


Figure 6.4: Representative TEM images of the catalysts CZA1 (a), CZA2 (b) and CZA3 (c) taken at moderate magnification for a statistical evaluation of the Cu particle size. Based on counting of thousands of Cu particles, the particle size distributions were determined. The log-normal fits to the obtained size histograms are shown in (d).

6.3.2 Experimental Setup, Activation Procedure and Activity Study

The catalyst activity and the copper surface area according to H_2 -TPD and nitrous oxide reactive frontal chromatography (N_2O -RFC) are determined in a glass lined single-pass fixed-bed reactor (internal diameter 4.5 mm) with internal thermocouple, an upstream gas mixing unit and a prior to every experiment calibrated mass spectrometer (Pfeiffer Vacuum OmniStar GSD 301 O) for time resolved in-situ analysis, as well as an Agilent 7820A gas chromatograph equipped with two thermal conductivity detectors, a packed Porapack-N column (Sigma Aldrich) for the quantification of CH_4 , CO_2 , H_2O , CH_2O , CH_3OH and a packed Molsieve 5 Å column (Sigma Aldrich) for the quantification of Ar, N_2 , CH_4 and CO. The setup can be pressurized up to 28 bar and operated in a temperature range from 77 up to 773 K. During the catalyst activation, N_2O -RFC and activity measurements each catalyst is treated with the same premixed gases of the following

compositions and purities: 2% H₂ (99.9999%)/He (99.99999), 1% N₂O (99.9990%)/He (99.9999%), 13.5% CO (99.997%)/3.5% CO₂ (99.9995%)/9.5% N₂ (99.9999)/73.5% H₂ (99.9999%). All other measurements are conducted using single high purity gases: H₂, He, N₂ 99.9999%. In order to remove traces of sulfur and carbonyls from the synthesis gas stream, a guard reactor is employed.

In a typical measurement 75 mg up to 150 mg catalyst (according to the expected amount of surface area) of the 250-355 μm sieve fraction and 500 mg purified silicon carbide of the same sieve fraction are heated up at atmospheric pressure for 15 hours in 2.0% H₂ in He raising the temperature from 300 to 448 K at 1 K min⁻¹, then in pure H₂ raising the temperature from 448 to 513 K at 1 K min⁻¹ and holding for 30 minutes. Under these conditions no brass formation in the catalyst bulk phase takes place.[33] In all cases a specific flow rate of 0.2 sccm g_{cat}⁻¹ is used.

The activity studies are performed after the H₂-TPD and N₂O-RFC measurements at 24 bar in synthesis gas (13.5% CO, 3.5% CO₂, 9.5% N₂, 3.5% H₂). The temperature ranges from 453 to 523 K. Prior to the study, the catalysts are reactivated for 60 minutes at 448 K in 2% H₂/He. All conversions were checked to be lower than 10% of the corresponding equilibrium conversion, the selectivity is in all cases beyond 99% and the mass balances are within 3% relative accuracy. In case of the most active sample CZA3, the formation of hotspots has been thoroughly checked to be absent by varying the dilution with SiC. Here, also the absence of intraparticle diffusion limitation was checked using different particle sieve fractions. The results are given in figure 6.7.

6.3.3 Hydrogen Temperature Programmed Desorption (H₂-TPD)

After the activation procedure, the catalyst is cooled down in helium to 235 K and pressurized for 30 minutes with 24 bar H₂. Variation of the adsorption pressure and adsorption time showed, that a full hydrogen coverage of copper can be achieved using these conditions. After the adsorption period the catalyst is rapidly cooled down to 77 K, depressurized to 1 bar and flushed with He for another 30 minutes until the H₂ baseline in the mass spectrometer is stable. The H₂-TPD experiment is conducted at 1 bar using a He flow rate of 100 sccm and heating rates β of 4, 6 and 10 K min⁻¹. It has been shown that under these conditions transport limitations are absent.[34] The amount of hydrogen is calculated using the full area under the desorption peak. In this context, signals above 375 K are ignored.

Exemplary results of the N₂O-RFC and H₂-TPD measurements are given in figure 6.5 and give an impression of the high data quality available for the detailed description of the catalyst surface. Even for the - compared to the other catalysts - low dispersion of pure copper a clean and distinct H₂-TPD signal is visible. To our knowledge, this is the first time that a clean and fully covered H₂-TPD of polycrystalline copper is presented

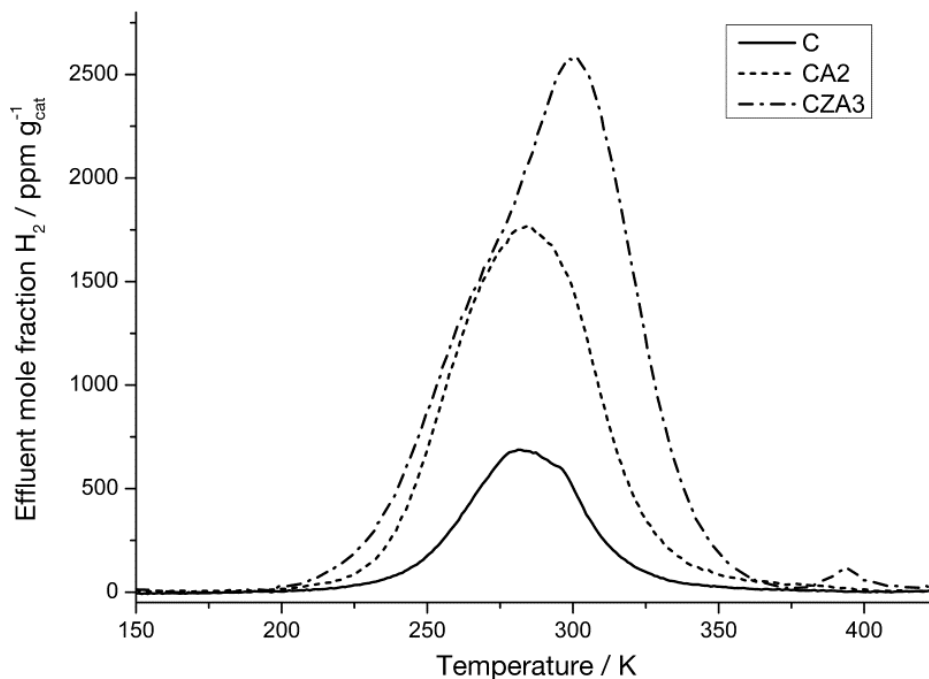


Figure 6.5: H_2 -TPD study on activated methanol synthesis catalysts. Measurement conditions: $Q = 100 \text{ sccm}$, $m_{\text{cat}} = 100 \text{ mg}$ (based on calcined precursor), $\beta = 6 \text{ K min}^{-1}$

under atmospheric conditions. The obtained H_2 -TPD peak temperatures (heating rate $\beta = 6 \text{ K min}^{-1}$: C & CA systems $283 \pm 2 \text{ K}$, CZA systems $300 \pm 2 \text{ K}$) are in good agreement with published data.[35, 36] Whereas in the C, CA and CM samples the desorption curve is perfectly symmetric, in the case of all CZA and CMZ catalysts a typical asymmetric curve is visible, which has been attributed to the morphologic structure of the copper particles.[13, 37] However, it should be noted that the MgO supported samples show no shift of the H_2 -desorption maximum after impregnation with ZnO but resemble the same shape and peak values as CZA samples. Careful reproduction of the experiments with fresh catalyst were performed with C, CA2 and CZA3, resulting in a maximum error margin of 5% for the H_2 area and $\pm 2 \text{ K}$ for the peak temperature. Temperature effects due to the position of the catalyst bed in the reactor have not been observed. With exception of the pure copper sample C no sintering tendencies are observed. The H_2 amount is also independent from the heating rate β . For every catalyst, the reported error bars are a result of at least three measurements, in case of the copper sample C three measurements each with fresh catalyst are employed. In all cases, the activated samples show no or very small traces of water contamination (signals at $T > 375 \text{ K}$)[38]

or other desorption signals within the given temperature range. Also no signal can be found in the given temperature range reproducing the experiments with pure SiC.

6.3.4 Nitrous Oxide - Reactive Frontal Chromatography (N₂O-RFC) and Defect Concentration

The N₂O copper surface area is determined using the activated catalyst sample after the H₂-TPD treatment at 308 K, 1 bar pressure and a flow rate setpoint of 7.5 sccm N₂O (1%) in He. The actual flow rate is determined prior and after the measurement with an automatic flow meter (BIOS Definer 220). At the chosen temperature, no significant bulk oxidation of copper is present and the N₂O decomposes according to theory quantitatively on the copper surface following the reaction:[39]



Holding the reactor under helium, the remaining setup is flushed with N₂O/He and after switching the reactor to 1% N₂O/He a breakthrough curve in the reactor effluent stream is measured using the calibrated mass spectrometer. The amount of copper surface atoms is calculated from the catalyst mass, exact flow rate and nitrogen area until the N₂O breakthrough. The specific Cu metal surface area is determined by using a value of $1.47 \cdot 10^{19}$ atoms per m² for the mean Cu surface atom density. The latter one is the arithmetic mean value of the low index planes Cu(111), Cu(110), Cu(100). As the subsurface oxidation cannot be completely avoided, the intersection between the falling N₂ signal and rising N₂O signal at the breakthrough point is used as a limit for the integration of the N₂ signal and a conservative error margin of $1 \text{ m}^2 \text{ g}_{\text{cat}}^{-1}$ ($12 \mu\text{mol N}_2\text{O g}_{\text{cat}}^{-1}$) is assumed, which is higher than the actual measured error when reproducing the experiments. An exemplary N₂O-RFC curve is given in figure 6.6 and the results are given in figure 6.7. The amount of oxophilic sites generated by the presence of ZnO is calculated from the difference of theoretical N₂O-adsorption capacity according to the copper surface determined via H₂-TPD and experimentally measured N₂O-adsorption capacity:

$$n_{\text{defects}} = n_{\text{N}_2\text{O,experiment}} - \frac{1}{2}n_{\text{Cu,surface}} = n_{\text{N}_2\text{O,experiment}} - \frac{3}{2}n_{\text{H}_2,\text{TPD}} \quad (6.3)$$

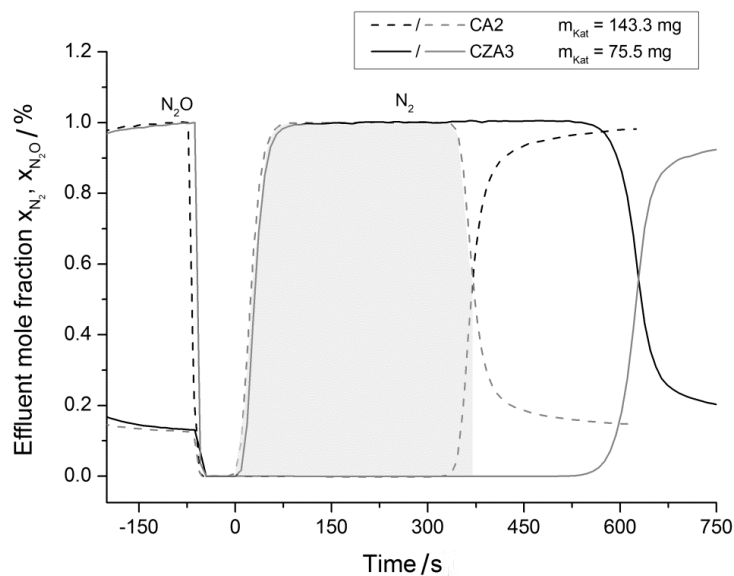


Figure 6.6: Exemplary N_2O -RFC curves of two catalysts. In case of CA2, the area used to determine the amount of produced N_2 is shaded gray. Experimental conditions: $T = 308\text{ K}$, $p = 1\text{ bar}$, $Q = 7.5\text{ sccm}$.

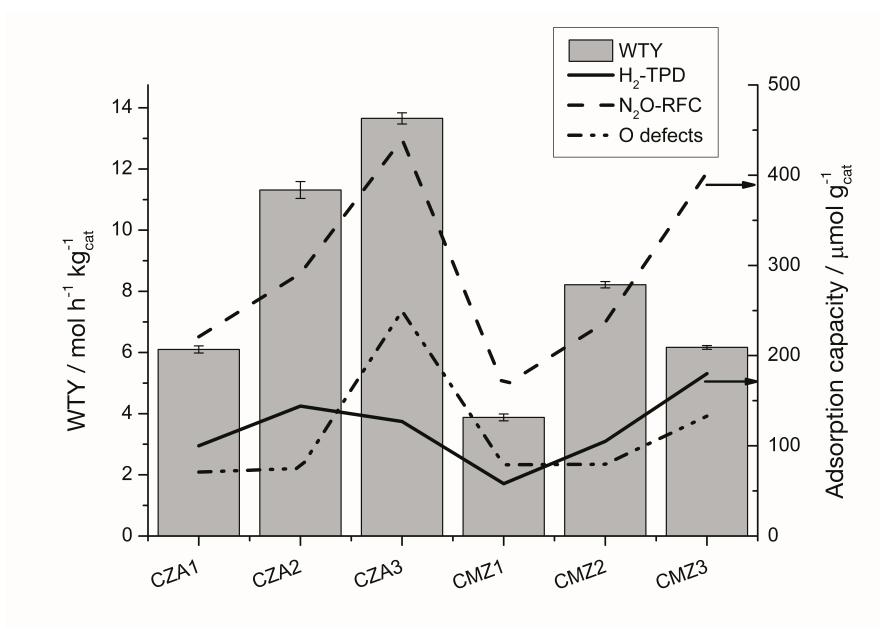


Figure 6.7: Graphical representation of the activity measurements and determined adsorption capacities according to N_2O -RFC, H_2 -TPD and corresponding amount of oxophilic sites generated by the presence of ZnO.

6.3.5 Model For The Microstructure of Common Cu/ZnO/Al₂O₃ Methanol Synthesis Catalysts

Figure 6.8 shows a comparison of the expected "specific Cu surface areas" of the CZA catalysts in $\text{m}^2 \text{g}^{-1}$, that is obtained if the N_2O chemisorption capacity is conventionally evaluated as probing the metallic surface only. The values are compared to the hypothetical maximal Cu surface area as determined by TEM and to the real Cu surface area as determined by H_2 chemisorption. As described in the main text in detail, the discrepancy of N_2O and H_2 Cu surface areas in all ZnO-containing catalysts can be explained with the contribution of SMSI-induced defect sites of ZnO. While it seems clear that the "extra N_2O " is consumed on (partially) reduced Zn sites, we here make an attempt to relate these surface area differences with the microstructure of the Cu/ZnO/Al₂O₃ catalyst as shown in the TEM images in figures 6.1, 6.4 and 6.9.

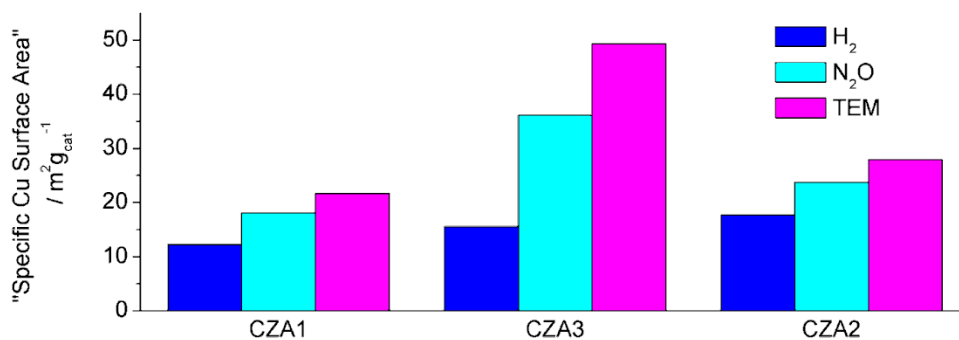


Figure 6.8: Comparison of the probe gas capacities of the CZA catalysts in this study if interpreted as specific Cu surface areas with the hypothetical maximal Cu surface area determined by TEM investigations shown in figure 6.4.

Images of the microstructure of methanol synthesis catalysts are shown in figures 6.1 and 6.9a-c as HRTEM and schematic representation. Typically, a disordered ZnO_x layer of 1-2 nm is found at the surface of the Cu particles after reduction. In rare cases, the ZnO_x overgrowth shows atomic ordering like in Figure 6.9c or stabilizes the atomically flat low-energy (111) facets of Cu and show a smaller down to the monolayer thickness, like the one in Figure 6.9d on the left side of the particle.

We assume that three types of Cu surfaces/interfaces exist: (i) a fraction present as interface to Wurzite-type ZnO particles that act as physical support of the Cu particles, (ii) a fraction that is covered by ZnO_x-overgrowth as shown in 6.1 of the main article and thus involved in Cu-ZnO interaction; and (iii) a fraction that is uncovered and directly exposed to the gas phase. A suggestion of the microstructural arrangement of these

types of surfaces in the catalysts is indicated in figure 6.9b using pink color for type (i), light blue to type (ii) and dark blue for type (iii).

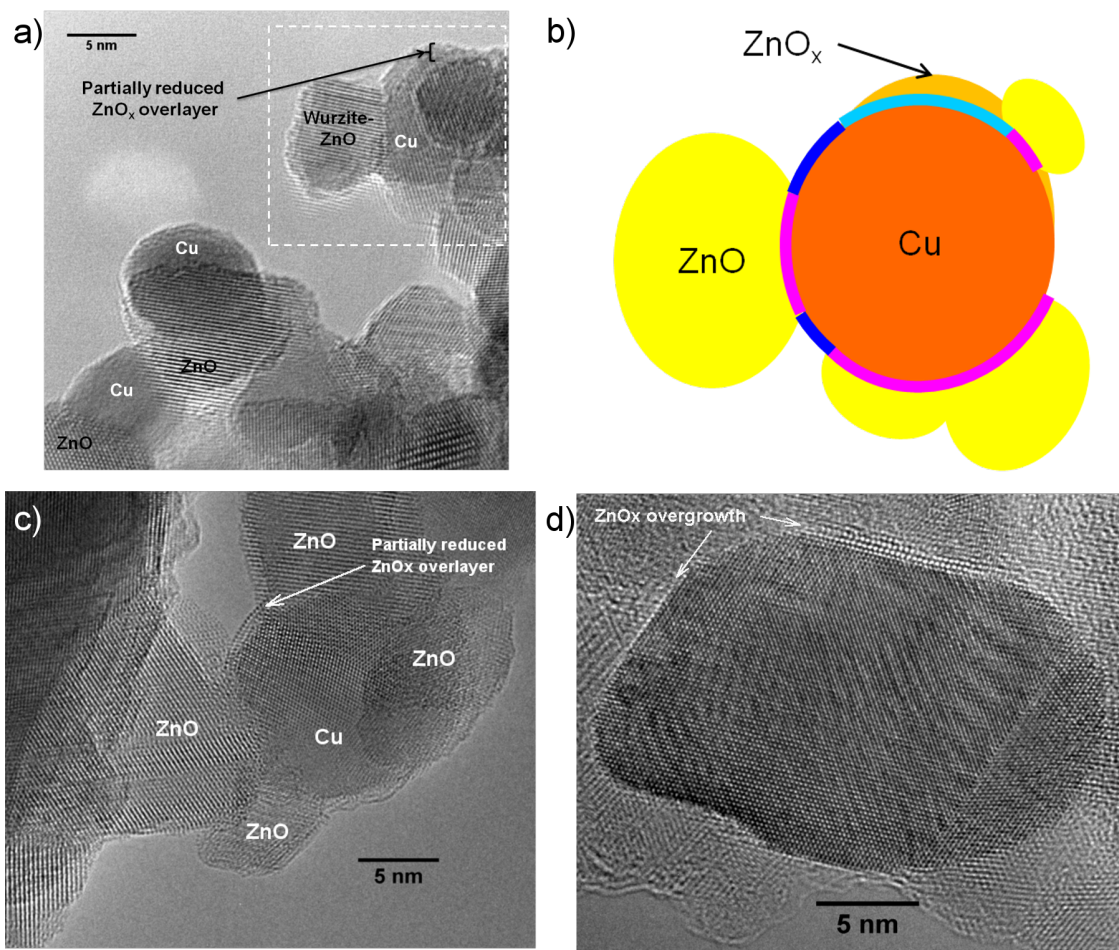


Figure 6.9: Representative HRTEM image of the catalysts CZA1 (a,c,d) and a schematic representation of a cross-section of the area in the dashed box (b). The color code refers to a proposed microstructural interpretation of the measured probe gas capacities shown in figure 6.8 and is explained in the text.

According to this simplified interpretation, the difference between TEM and N₂O surface areas can be seen as an estimate of the contact area between Cu and Wurzite-type ZnO, which are inaccessible for probe molecules and guarantees structural integrity to the catalysts (type (i)). The N₂O surface area would be the sum of type (ii) and type (iii), i.e. the difference between N₂O and H₂ surface areas is a measure for the degree of Cu-ZnO interaction, leading to partial reduction of ZnO and formation of ZnO_x-overgrowth. Finally type (iii) is directly measured by H₂ chemisorption. According to the quantification shown in Figure 6.8, this interpretation seems reasonable. However, other

models involving, e.g., surface alloy formation or dynamic de-wetting of Cu are possible as well. In particular, the reactivity of the ZnO_x-overlayer toward O and H atoms is not clear and needs further investigation. Independent of these structural details, the better correlation of the N₂O-derived chemisorption capacity with the methanol synthesis activity within this catalyst series (sum of metallic Cu and oxophilic Zn^{δ+} sites) compared to the H₂-derived capacity (only Cu sites) or the difference of both (only Zn^{δ+} sites) supports the idea of a bi-functional active site for methanol synthesis.

6.4 Copyright Information

Chapter 6 has been published under the title "*Counting of oxygen defects vs. metal surface sites in methanol synthesis catalysts by different probe molecules*"[40] and is protected by copyright. The reproduction in this thesis has been licensed by *John Wiley and Sons* under license number 3417560772976. A full copy of the license agreement is presented in the appendix.

References

- [1] R. Mallhotra, *Fossil Energy*, Springer, New York, **2012**.
- [2] G. A. Olah, *Angew. Chem. Int. Ed.* **2013**, *52*, 104–107, DOI 10.1002/anie.201204995.
- [3] L. C. Grabow, M. Mavrikakis, *ACS Catal.* **2011**, *1*, 365–384, DOI 10.1021/cs200055d.
- [4] T Askgaard, *J. Catal.* **1995**, *156*, 229–242, DOI 10.1006/jcat.1995.1250.
- [5] M. Behrens, F. Studt, I. Kasatkin, S. Köhl, M. Hävecker, F. Abild-Pedersen, S. Zander, F. Girgsdies, P. Kurr, B.-L. Kniep, M. Tovar, R. W. Fischer, J. K. Nørskov, R. Schlögl, *Science* **2012**, *336*, 893–897, DOI 10.1126/science.1219831.
- [6] C. V. Ovesen, B. S. Clausen, J. Schiøtz, P. Stoltze, H. Topsøe, J. K. Nørskov, *J. Catal.* **1997**, *168*, 133–142, DOI 10.1006/jcat.1997.1629.
- [7] M. S. Spencer, *Top. Catal.* **1999**, *8*, 259–266, DOI 10.1023/A:1019181715731.
- [8] T. Fujitani, J. Nakamura, *Catal. Lett.* **1998**, *56*, 119–124, DOI 10.1023/A:1019000927366.
- [9] R. N. d’Alnoncourt, X. Xia, J. Strunk, E. Löffler, O. Hinrichsen, M. Muhler, *Phys. Chem. Chem. Phys.* **2006**, *8*, 1525–1538, DOI 10.1039/B515487A.
- [10] S. Zander, E. L. Kunkes, M. E. Schuster, J. Schumann, G. Weinberg, D. Teschner, N. Jacobsen, R. Schlögl, M. Behrens, *Angew. Chem. Int. Ed.* **2013**, *52*, 6536–6540, DOI 10.1002/anie.201301419.
- [11] S. Polarz, J. Strunk, V. Ischenko, M. W. E. van den Berg, O. Hinrichsen, M. Muhler, M. Driess, *Angew. Chem. Int. Ed.* **2006**, *45*, 2965–2969, DOI 10.1002/anie.200503068.
- [12] M. Kurtz, J. Strunk, O. Hinrichsen, M. Muhler, K. Fink, B. Meyer, C. Wöll, *Angew. Chem. Int. Ed.* **2005**, *44*, 2790–2794, DOI 10.1002/anie.200462374.
- [13] H. Wilmer, O. Hinrichsen, *Catal. Lett.* **2002**, *82*, 117–122, DOI 10.1023/A:1020560628950.
- [14] J.-D Grunwaldt, A Molenbroek, N.-Y Topsøe, H Topsøe, B. S. Clausen, *J. Catal.* **2000**, *194*, 452–460, DOI 10.1006/jcat.2000.2930.
- [15] P. L. Hansen, J. B. Wagner, S. Helveg, J. R. Rostrup-Nielsen, B. S. Clausen, H. Topsøe, *Science* **2002**, *295*, 2053–2055, DOI 10.1126/science.1069325.
- [16] P. C. Vesborg, I. Chorkendorff, I. Knudsen, O. Balmes, J. Nerlov, A. M. Molenbroek, B. S. Clausen, S. Helveg, *J. Catal.* **2009**, *262*, 65–72, DOI 10.1016/j.jcat.2008.11.028.

- [17] V. Schott, H. Oberhofer, A. Birkner, M. Xu, Y. Wang, M. Muhler, K. Reuter, C. Wöll, *Angew. Chem. Int. Ed.* **2013**, *52*, 11925–11929, DOI 10.1002/anie.201302315.
- [18] T. Fujitani, J. Nakamura, *Appl Catal A* **2000**, *191*, 111–129, DOI 10.1016/S0926-860X(99)00313-0.
- [19] I. A. Fisher, H. C. Woo, A. T. Bell, *Catal. Lett.* **1997**, *44*, 11–17, DOI 10.1023/A:1018916806816.
- [20] Q.-L. Tang, Q.-J. Hong, Z.-P. Liu, *J. Catal.* **2009**, *263*, 114–122, DOI 10.1016/j.jcat.2009.01.017.
- [21] J. Xiao, T. Frauenheim, *J. Phys. Chem. Lett.* **2012**, *3*, 2638–2642, DOI 10.1021/jz301119k.
- [22] G. C. Chinchin, C. M. Hay, H. D. Vandervell, K. C. Waugh, *J. Catal.* **1987**, *103*, 79–86.
- [23] M. Muhler, L. P. Nielsen, E. Törnqvist, B. S. Clausen, H. Topsøe, *Catal. Lett.* **1992**, *14*, 241–249.
- [24] G. Anger, A. Winkler, K. Rendulic, *Surf. Sci.* **1989**, *220*, 1–17, DOI 10.1016/0039-6028(89)90459-7.
- [25] G. Lee, D. B. Poker, D. M. Zehner, E. W. Plummer, *Surf. Sci.* **1996**, *357-358*, 717–720, DOI 10.1016/0039-6028(96)00252-X.
- [26] M. Luo, G. Hu, M. Lee, *Surf. Sci.* **2007**, *601*, 1461–1466, DOI 10.1016/j.susc.2006.12.077.
- [27] E. M. Mccash, S. F. Parker, J. Pritchard, M. A. Chesters, *Surf. Sci.* **1989**, *215*, 363–377, DOI 10.1016/0039-6028(89)90266-5.
- [28] T. Mitsui, M. K. Rose, E. Fomin, D. F. Ogletree, M. Salmeron, *Nature* **2003**, *422*, 705–707, DOI 10.1038/nature01557.
- [29] M. Behrens, S. Zander, P. Kurr, N. Jacobsen, J. Senker, G. Koch, T. Ressler, R. W. Fischer, R. Schlögl, *J. Am. Chem. Soc.* **2013**, *135*, 6061–6068, DOI 10.1021/ja310456f.
- [30] O. Martin, J. Pérez-Ramírez, *Catal. Sci. Technol.* **2013**, *3*, 3343–3352, DOI 10.1039/C3CY00573A.

- [31] E. Doesburg, R. Höppener, B. de Koning, X. Xiaoding, J. Scholten in *Preparation of catalysts IV scientific bases for the preparation of heterogeneous catalysts: proceedings of the fourth international symposium; Louvain-la-Neuve, September 1-4, 1986*, (Ed.: B. Delmon, F. Grange, P.A. Jacobs, G. Poncelet), Preparation of Catalysts IV Scientific Bases for the Preparation of Heterogeneous Catalysts, Elsevier, Amsterdam, **1987**, pp. 767–780.
- [32] M. Behrens, R. Schlögl, *Z. Anorg. Allg. Chem.* **2013**, *639*, 2683–2695, DOI 10.1002/zaac.201300356.
- [33] T. Kandemir, D. Wallacher, T. Hansen, K.-D. Liss, R. Naumann d'Alnoncourt, R. Schlögl, M. Behrens, *Nuclear Instruments and Methods in Physics Research Section A: Accelerators Spectrometers Detectors and Associated Equipment* **2012**, *673*, 51–55, DOI 10.1016/j.nima.2012.01.019.
- [34] M. Peter, J. Fendt, H. Wilmer, O. Hinrichsen, *Catal. Lett.* **2012**, *142*, 547–556, DOI 10.1007/s10562-012-0807-3.
- [35] T. Genger, O. Hinrichsen, M. Muhler, *Catal. Lett.* **1999**, *59*, 137–141, DOI 10.1023/A:1019076722708.
- [36] H. Wilmer, T. Genger, O. Hinrichsen, *J. Catal.* **2003**, *215*, 188–198, DOI 10.1016/S0021-9517(03)00003-4.
- [37] M. Peter, J. Fendt, S. Pleintinger, O. Hinrichsen, *Catal. Sci. Technol* **2012**, *2*, 2249–2257, DOI 10.1039/c2cy20189e.
- [38] O. Hinrichsen, T. Genger, M. Muhler in *Studies in Surface Science and Catalysis*, (Eds.: A. Corma, F. V. Melo, S. Mendioroz, J. L. G. Fierro), 12th International Congress on Catalysis Proceedings of the 12th ICC, Elsevier, **2000**, pp. 3825–3830.
- [39] O. Hinrichsen, T. Genger, M. Muhler, *Chem. Eng. Technol.* **2000**, *23*, 956–959, DOI 10.1002/1521-4125(200011)23:11<956::AID-CEAT956>3.0.CO;2-L.
- [40] M. B. Fichtl, J. Schumann, I. Kasatkin, N. Jacobsen, M. Behrens, R. Schlögl, M. Muhler, O. Hinrichsen, *Angew. Chem. Int. Ed.* **2014**, *53*, 7043–7047, DOI 10.1002/anie.201400575.

7 On the temperature programmed desorption of hydrogen from polycrystalline copper

7.1 Abstract

Temperature programmed hydrogen desorption (H_2 -TPD) is a versatile tool to characterize metal surfaces in heterogeneous catalysts. We present a systematic H_2 -TPD study combined with a kinetic analysis of the H_2 desorption process from pure polycrystalline copper and alumina supported copper. The results show that, in contrast to typical Cu/ZnO based methanol synthesis catalysts, the alumina support has no measurable influence on the desorption process and that the copper surface in both catalyst can be accurately described by a theoretically deduced mixture of the low index planes Cu(100), Cu(110), and Cu(111).

7.2 Introduction

In order to understand the activity and nature of supported metal catalysts, the characterization of the metal surface exposed to the gas atmosphere during reaction conditions is of vital importance. Typically, this is done by specific chemisorption of a probe molecule like hydrogen or carbon monoxide on the metal followed by quantification of the adsorbed amount either by frontal chromatography, pressure or concentration programmed techniques or temperature programmed desorption (TPD).

In case of copper based methanol synthesis catalysts two major techniques, the reactive N_2O frontal chromatography (N_2O -RFC) and temperature programmed hydrogen desorption (H_2 -TPD), have been developed to analyze catalyst activity behavior.[1, 2] Especially the N_2O -RFC is widely employed due to its simplicity and fast measuring process. Although recent results showed that the application of N_2O -RFC in typical Cu/ZnO/ Al_2O_3 systems does not only oxidize the copper surface, but also oxygen defect sites generated at the Cu/ZnO interface, a linear relationship between activity and N_2O adsorption capacity can often be established for catalysts with similar preparation

history.[3–5] In contrast, the H₂-TPD method only describes the exposed copper surface area, but suffers from a more challenging experimental effort as the dissociative adsorption of hydrogen on copper is an activated process and full coverage is only achieved at low temperatures using elevated pressure or predecomposed atomic hydrogen.[6, 7] Apart from a pure quantification of the exposed metal surface area, the desorption signal also contains useful information about the hydrogen desorption enthalpy or possible metal-support interactions in the catalyst. As shown for Cu/ZnO/Al₂O₃ systems, this technique enables to monitor dynamic morphologic changes of the copper crystallites which are induced by partial reduction of the ZnO in vicinity to copper.[8–10] As this process is a function of the gas atmosphere reduction potential and influences the catalyst activity it has also been included in a microkinetic model which can be extrapolated to industrially relevant conditions.[11–13]

However, the nature of the copper surface probed by H₂ desorption is still vague. On the one hand, the activity of typical copper based methanol synthesis catalysts is definitely dependent on a strong synergy between Cu and ZnO. Behrens et al. [14] pointed out that the integration of single Zn atoms into the copper surface enhances the catalyst activity and that the formation of a Cu/Zn surface alloy is an open discussed topic in methanol synthesis catalysts.[15, 16] On the other hand Kuld et al. [5] concluded from their results that the formation of this surface alloy leads to a strong decrease in H₂ binding energy on the copper surface which prohibits the probing of this surface with the common H₂-TPD technique. An analysis of the H₂-TPD desorption signal on Cu/Al₂O₃ and Cu/ZnO by Wilmer et al. [6], however, demonstrated that the desorption signal is shifted to higher temperatures in case of Cu/ZnO systems, i.e. the hydrogen is bond even stronger to the remaining copper surfaces in close contact with ZnO. Although the alumina present in these catalysts is commonly assumed to be only an irreducible structural support, Behrens et al. [17] recently showed that the incorporation of Al³⁺ into the ZnO framework has a significant effect on the Cu/ZnO/Al₂O₃ catalyst activity and has to be considered carefully in systematic catalyst development. With respect to these recent results it seems necessary to also explore the possible influence of alumina on the hydrogen adsorption on copper: Therefore, we present a systematic H₂-TPD study on polycrystalline copper and alumina supported copper to elucidate this issue.

7.3 Experimental and Computational Methods

7.3.1 Catalyst preparation

The synthesis procedure of the polycrystalline copper catalyst C and the Cu/Al₂O₃ catalyst CA with the nominal Cu/Al₂O₃ ratio of 85/15 mol-% is based on a co-precipitation concept for the industrial Cu/ZnO/Al₂O₃ catalyst, which has been recently reviewed in detail elsewhere.[18] The catalysts C and CA are precipitated from the metal nitrate solutions at a constant pH of 7 and a temperature of 303 K using a sodium carbonate solution as precipitating agent. After an aging period of 60 minutes the precipitate is filtered off, washed three times with bidestillated water, and dried at 353 K over night. The dry powder is then calcined for 10 h at 593 K in $Q = 50 \text{ sccm g}^{-1}$ of synthetic air.

The metal content of the calcined precursors is analyzed by ICP-OES (SpectroFlame FTMOA81A, Spectro Analytical Instruments). Here, the samples are also checked for the absence of sodium and potassium impurities. Prior to the analysis, the samples are dissolved in boiling aqua regia, inspissated and diluted with 1 M HNO₃. Nitrogen physisorption of the calcined precursors is measured in a NOVA 4000e Surface Area & Pore Size Analyzer (Quantachrome Instruments) at 78 K. Prior to analysis, all samples are outgassed under vacuum at 523 K for 3 h. For analysis of the BET surface area ten evenly spaced points in the pressure region from 0.05 to 0.3 bar are used. The BET surface area of the reduced polycrystalline copper sample C is analyzed after the activation procedure (see below) in an Autosorb C (Quantachrome Instruments). A summary of the characterization parameters is presented in table 7.1.

Table 7.1: Summary of the characterization results of C and CA.

	Cu/Al [mol – %]	$n_{\text{H}_2\text{-TPD}}$ [$\mu\text{mol g}_{\text{cat}}^{-1}$]	$n_{\text{N}_2\text{O-RFC}}$ [$\mu\text{mol g}_{\text{cat}}^{-1}$]	$S_{\text{BET}}^{\text{[a]}}$ [$\text{m}^2 \text{g}_{\text{cat}}^{-1}$]
C	100/-	23.2 ± 0.5	33.5 ± 0.1	15/3.1
CA	84/16	89.3 ± 1.8	131.5 ± 2.1	46.6/n.d.

[a] calcined sample / activated sample

The copper surface area according to H₂-TPD and nitrous oxide reactive frontal chromatography (N₂O-RFC) are determined in a glass lined single-pass fixed-bed reactor (internal diameter 4.5 mm) with internal thermocouple, an upstream gas mixing unit and a mass spectrometer (Pfeiffer Vacuum OmniStar GSD 301 O) for time resolved in-situ analysis, which is calibrated prior to every measurement. A detailed description and schematic representation of the setup is given in the supporting information (chapter 7.4). The system can be pressurized up to 28 bar and operated in a temperature

range from 77 up to 773 K. During the catalyst activation, N₂O-RFC and H₂-TPD measurements each catalyst is treated with the same gases of the following compositions and purities: H₂ (99.9999%), He (99.9999%), 2% H₂ (99.9999%)/He (99.9999%), and 1% N₂O (99.9990%)/He(99.9999%).

In a typical measurement $m_{\text{calc}} = 75$ mg (CA) or 350 mg (C) calcined catalyst of the 250-355 μmol catalyst sieve fraction and 500 mg purified silicon carbide of the same sieve fraction are heated up at atmospheric pressure for 15 hours in a mixture containing 2.0% H₂ in He using the following temperature program: the temperature is raised from 300 to 448 K at 1 K min⁻¹, followed by switching to pure H₂ raising the temperature from 448 to 513 K at 1 K min⁻¹ and holding for 30 minutes. For the activation procedure, a specific flow rate of 0.2 sccm g_{calc}⁻¹ is used.

7.3.2 Hydrogen Temperature Programmed Desorption (H₂-TPD)

The H₂-TPD measurements follow a well established method described in ref. [1]. The activated catalyst is cooled down to 235 K in helium and pressurized with 24 bar hydrogen for 30 minutes. A variation of the adsorption pressure and time showed that under these conditions full hydrogen coverage of copper is achieved. The catalyst is rapidly cooled down to 77 K, depressurized to atmospheric pressure and flushed at least 30 min with 100 sccm helium until the baseline in the mass spectrometer shows a constant value. Subsequently the catalyst bed is heated up under atmospheric pressure in a helium flow of $Q = 100$ sccm helium ramping linearly at $\beta = 2, 4, 6$ or 10 K min⁻¹. The desorption signal upon heating the catalyst bed is monitored in the mass spectrometer. A typical H₂-TPD curve is presented in figure 7.1.

The symmetric H₂ desorption signal of copper is centered around 280 K, very distinctive, and resembles single crystal UHV experiments by Anger et al.[7] The amount of adsorbed hydrogen is calculated using the full area under the desorption peak. Apart from this desorption peak, a smaller one is found at 90 K, which can be assigned to the desorption of weakly adsorbed hydrogen and nitrogen. In all cases, no significant signal above 350 K is visible, which stems from the decomposition of adsorbed water.[19] The raw data are corrected by subtracting a constant baseline. In order to account for possible sintering of the unsupported copper catalyst, every experiment is performed with a fresh activated amount of catalyst.

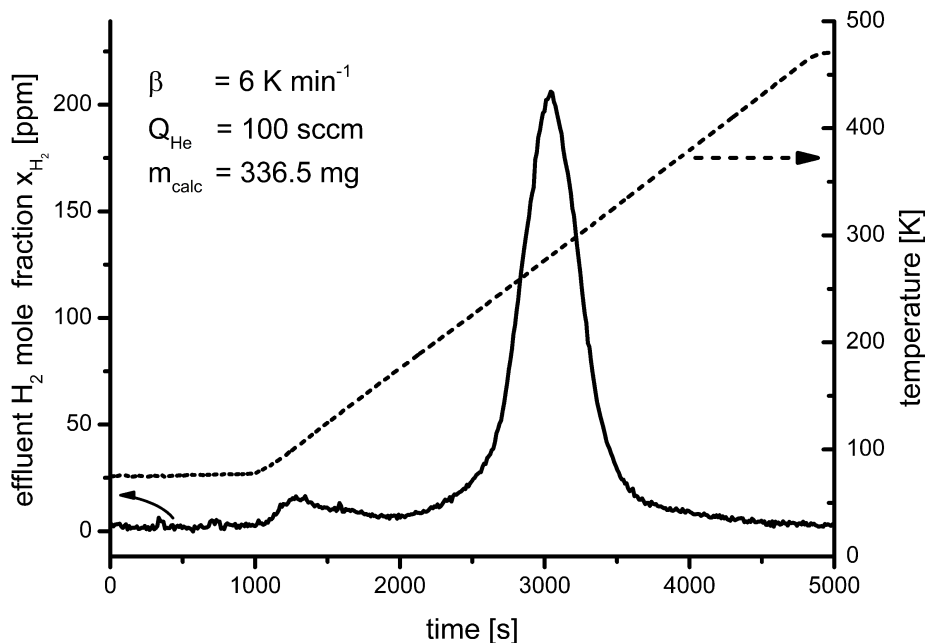


Figure 7.1: Exemplary H₂-TPD of the polycrystalline copper sample C.

7.3.3 Reactive N₂O Frontal Chromatography

The N₂O copper surface area is determined at 1 bar pressure subsequent to the H₂-TPD experiment followed by cooling down to 308 K in helium. At this temperature, no significant bulk oxidation of copper is present and the N₂O decomposes on the copper surface following the reaction:[1]



Holding the reactor under helium, the remaining setup is flushed with N₂O/He and after switching the reactor to 1% N₂O/He a breakthrough curve in the reactor effluent stream is measured in the mass spectrometer. The amount of copper surface atoms is calculated from the catalyst mass, exact flow rate and N₂ area until the N₂O breakthrough. In order to determine the copper surface area, a mean copper surface atom density of $1.47 \cdot 10^{19}$ atoms per m² is used. The latter one is the arithmetic mean value of the low index planes Cu(111), Cu(110), and Cu(100). As subsurface oxidation cannot be completely avoided, the intersection between the falling N₂ signal and rising N₂O signal

at the breakthrough point is used as a limit for the integration of the N_2 signal. This is illustrated in figure 7.2.

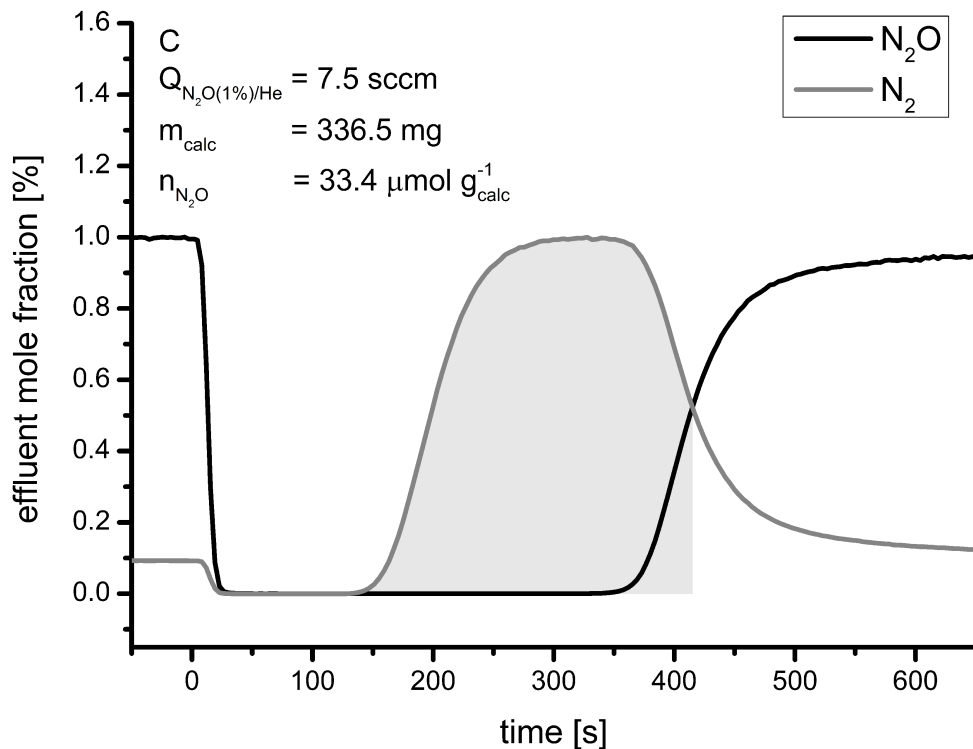


Figure 7.2: Exemplary reactive N_2O frontal chromatography on polycrystalline copper. The area shaded in gray is used to determine the copper surface area.

7.3.4 Modelling of the Desorption Signal

In order to enable a well-founded comparison of the desorption processes on polycrystalline copper with Al_2O_3 -supported systems, a mathematical model describing the desorption signals is used. The modelling approach to describe TPD flow experiments is well established has been extensively described in previous publications.[20, 21] In the most simple case (model 1), the desorption process is described by a second order process from a Cu(111) surface.[21] A coverage-dependent activation energy of desorption ($E_A - E_\Theta \Theta^n$) is used to account for signal asymmetry and peak broadening. The resulting rate constant is implemented in an Arrhenius-type format:

$$k_{des} = k_{0,des} \cdot \exp\left(-\frac{E_A - E_\Theta \Theta^n}{RT}\right) \quad (7.2)$$

Although, the theoretical distribution and different desorption behavior of the low-index (100), (110), and (111) copper facets is well known, this concept has not yet been applied for ZnO free systems.[8, 9, 11, 22] However, due to the absence of possible metal support interactions, the polycrystalline copper catalyst C is an ideal model system to validate this concept. Hence, in the second model (model 2) the presence of the three copper facets with a fixed ratio according to the Wulff construction is considered. In order to reduce the amount of model parameters, a common prefactor $k_{0,des} = 3.75 \cdot 10^{10} \text{ s}^{-1}$, which has been derived from studies on Cu/ZnO/Al₂O₃ systems [21], and in case of model 2 also a facet independent, linear coverage-dependent activation energy is employed.

$$k_{des,hkl} = k_{0,des} \cdot \exp\left(-\frac{E_{A,hkl} - E_{\Theta} \Theta_{H,hkl}}{RT}\right) \quad (7.3)$$

The facet distribution for crystalline copper is calculated using the software package WinXMorph [23, 24] and surface free energies for copper crystals in vacuum.[25] The resulting facet distribution η_{hkl} and the copper surface atom density σ_{hkl} per facet are given in table 7.2. These values are also in good agreement for H₂ treated copper particles adsorbed on ZnO.[8]

Table 7.2: Facet distribution according to the Wulff construction and copper surface atom density per facet.

	Cu(111)	Cu(110)	Cu(100)
η_{hkl} [%]	61	13	26
σ_{hkl} [mol m ²]	$2.94 \cdot 10^{-5}$	$1.79 \cdot 10^{-5}$	$2.54 \cdot 10^{-5}$

The catalyst bed is described by a pseudo homogeneous continuous stirred tank reactor (CSTR) in absence of intraparticle mass transfer and H₂ readsorption on the catalyst surface. In prior studies, both processes showed to have no influence on the results under the given experimental conditions.[21] The governing equations are given as:

$$\frac{\delta n_{H_2}}{\delta t} = \dot{n}_{H_2,0} - \dot{n}_{H_2} - \sum \left(N_{H_2,hkl} \frac{\delta \Theta_{H,hkl}}{\delta t} \right) \quad (7.4)$$

$$\frac{\delta \Theta_{H,hkl}}{\delta t} = -2k_{des,hkl} \Theta_{H,hkl}^2 \quad (7.5)$$

Although, every facet exhibits a different surface structure, the Cu:H₂ adsorption stoichiometry is considered constant. Hence, the specific amount of adsorbed hydrogen N_{H_2} is a function of the respective copper surface atom density and the facet distribution:

$$N_{H_2} = \sum (N_{H_2,hkl}) \quad (7.6)$$

$$N_{H_2,100} : N_{H_2,110} : N_{H_2,111} = \eta_{100} \sigma_{100} : \eta_{110} \sigma_{110} : \eta_{111} \sigma_{111} \quad (7.7)$$

Solving the differential equations and the model parameter estimation is done in the Athena Visual Studio engineering software.[26] The hydrogen effluent mole fraction relative to the peak maximum value is chosen as objective function, gradients are calculated using a forward difference scheme, and the absolute objective function tolerance is set to 10^{-10} . For the parameter estimation the integrated Bayesian Estimation method is used. The quality of the fit is evaluated using a dimensionless scaled root mean square error (SRMSE) between the experimental hydrogen effluent mole fraction x_{H_2} and the modeling result.

$$SRMSE = \frac{1}{X_{Ref}} \sqrt{\frac{1}{N} \sum_{j=1}^N (x_{H_2,experiment}(T_j) - x_{H_2,model}(T_j))^2} \quad (7.8)$$

For the reference value X_{Ref} , the experimental hydrogen effluent mole fraction at the peak maximum is used. For all peaks, the temperature region for determining the SRMSE values is between 225 K and 350 K. Reproduction experiments showed, that the SRMSE value of two desorption spectra with equal experimental conditions is roughly 0.04, which is a common value for flow TPD experiments.[20]

7.3.5 Results and Discussion

The H₂-TPD results of the heating rate variation for C and CA and the corresponding SRMSE values for the parameterized models 1 and 2 are summarized in table 7.3. An exemplary comparison of the H₂-TPD signals on the polycrystalline copper sample C with measurements on supported copper CA and modelling results according to model 1 is presented in figure 7.3.

Table 7.3: Summary of the measurement and fitting results.

Catalyst	N_{H_2}	N_{N_2O}	β	$T_{max}^{[a]}$	SRMSE	SRMSE ^[b]
	$[\mu\text{mol g}_{\text{calc}}^{-1}]$	$[\mu\text{mol g}_{\text{calc}}^{-1}]$	$[\text{K min}^{-1}]$	$[\text{K}]$	model 1	model 2
C	22.7	n.d.	2	273	0.046	0.042 / 0.032
C	23.2	n.d.	4	278	0.059	0.064 / 0.058
C	23.0	33.6	6	282	0.042	0.051 / 0.043
C	23.9	33.4	10	288	0.040	0.061 / 0.037
CA	87.2	n.d.	4	279	0.029	0.049 / 0.046
CA	90.3	130	6	284	0.032	0.064 / 0.045
CA	90.3	133	10	288	0.029	0.079 / 0.041

[a] from experimental curve [b] without coverage-dependency / with coverage-dependency

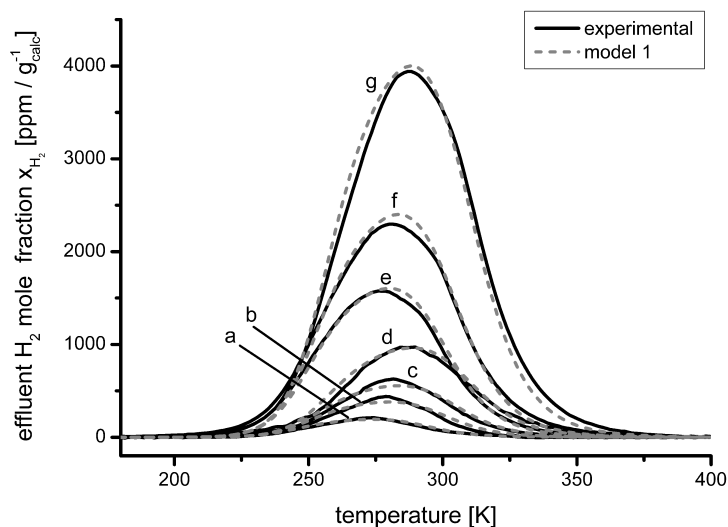


Figure 7.3: Comparison of the experimental H₂-TPD curve with the parameterized model 1 for polycrystalline copper C (a-d: $\beta = 2\text{-}10 \text{ K min}^{-1}$) and for CA (e-g: $\beta = 4\text{-}10 \text{ K min}^{-1}$)

Typically, the presence of strong metal support interaction alters the electronic properties of the metal surface and hence the adsorption properties.[26, 27] In case of Cu/ZnO systems the formation of partially amorphous ZnO_x overlayers and thin polar ZnO films is observed and the effect of partial alloying of Zn atoms into the copper surface on methanol synthesis has been studied in detail.[14, 28] It also leads to a shift of the desorption maximum to higher temperatures. The peak maximum temperatures of CA very much resemble the ones of the polycrystalline copper sample C and are in good agreement with literature data for other Cu/Al₂O₃ systems.[6] This suggests that Al₂O₃ in fact only acts a rigid support for the copper particles and has no pronounced influence on the electronic structure of the system. This is also supported by the high similarity of the peak shapes of C and CA. Although the specific copper surface area of CA results in a roughly four times higher value than of C, all signals can be described by the same model. The optimized parameters for the evaluated models 1 and 2 are presented in table 7.4.

Table 7.4: Optimized parameters for model 1 and 2. In both models a fixed prefactor of $k_{0,des} = 3.75 \cdot 10^{10} \text{s}^{-1}$ is used.

model 1	model 2
$E_A = 71.26 \pm 0.11 \text{ kJ mol}^{-1}$	$E_{A,100} = 63.97 \pm 0.14 \text{ kJ mol}^{-1}$
$E_{\Theta} = 5.27 \pm 0.11 \text{ kJ mol}^{-1}$	$E_{A,110} = 78.46 \pm 0.54 \text{ kJ mol}^{-1}$
$n = 2.33 \pm 0.11$	$E_{A,111} = 71.01 \pm 0.16 \text{ kJ mol}^{-1}$
	$E_{\Theta} = 0.98 \pm 0.2 \text{ kJ mol}^{-1}$

In both cases acceptable SRMSE values below or only slightly above 0.04 can be achieved. In model 1 the obtained parameters for the coverage dependency are very similar to values for Cu/ZnO/Al₂O₃ systems[21] and the roughly 15 K lower temperature onset of the desorption signal is accounted for by a slightly (4 kJ mol^{-1}) lower activation energy of desorption. It should be noted, that in this model the coverage dependence factor n defines the desorption signal asymmetry and has no real physical meaning. This can be nicely illustrated by applying model 1 on a highly asymmetric H₂-TPD spectrum: figure 7.4 shows the H₂-TPD spectrum and corresponding modelling result for a high performance Cu/ZnO/Al₂O₃ catalyst presented in ref. [4]. Although the catalyst clearly exhibits an at least bimodal desorption signal, it can be accurately described by a coverage-dependent desorption from one single copper facet.

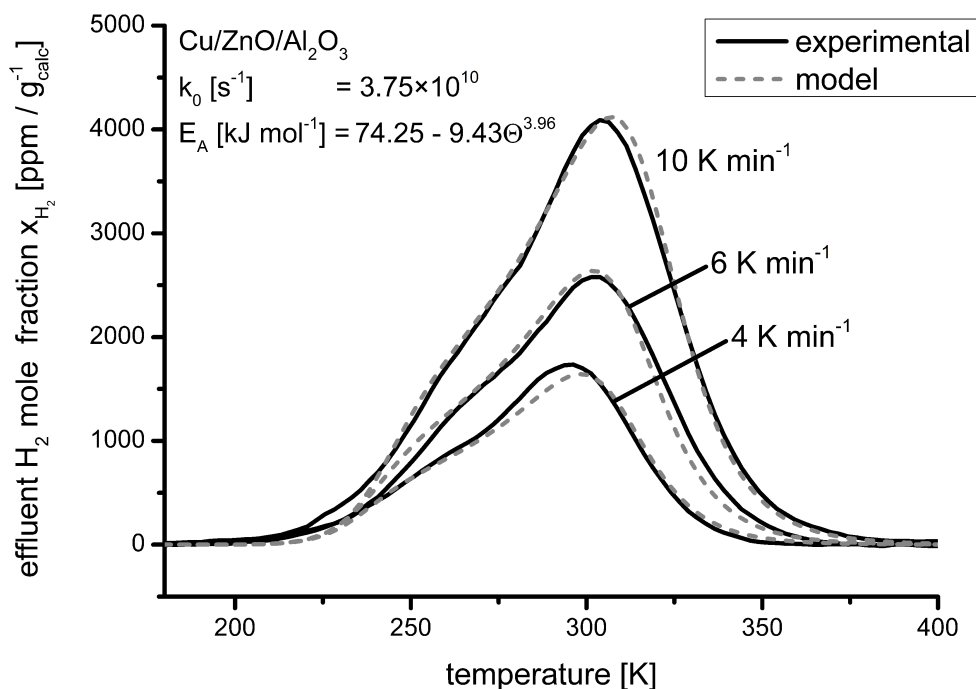


Figure 7.4: Modelling results of H₂-TPD spectra from a Cu/ZnO/Al₂O₃ catalyst.

A physically more reasonable interpretation of the desorption signal can be achieved by considering the presence of the low-index (100), (110), and (111) copper facets in model 2. An exemplary description of the desorption signal according to this model is presented in figure 7.5.

As mentioned above, the fixed facet distribution is deduced from a Wulff construction, which is only valid for free copper crystals. Although, the alumina support structure seems to have no significant electronic influence on the desorption process, it is not known a priori, whether other influences like a preferred contact orientation of the copper facets on alumina exists. Therefore, the fitting process is only applied on the polycrystalline copper sample C and the obtained model parameters are transferred without further alteration to the CA sample. Compared to model 1 this leads to slightly worse SRMSE values for CA, however, the overall model is still in good agreement with the measured spectra which confirms the statement that the alumina support has no significant influence on the exposed copper particle surface. The obtained activation energies result in a desorption process starting from Cu(100) followed by Cu(111) and ending with Cu(110). The same order has been observed and discussed for desorption in differently pretreated Cu/ZnO/Al₂O₃ systems.[22] In order to estimate the coverage dependency of the desorption process, the model is also parametrized without a coverage

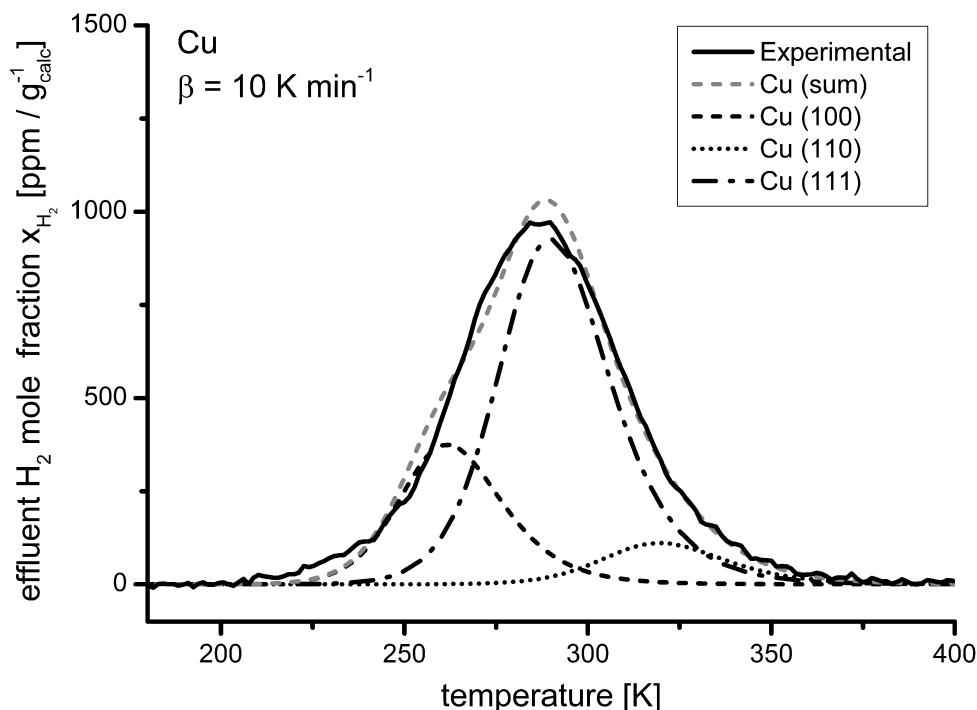


Figure 7.5: Exemplary description of the desorption signal of H_2 from polycrystalline copper considering the presence of Cu(111), Cu(110) and Cu(100) facets.

dependent activation energy of desorption E_{Θ} (see table 7.3). It turns out that the introduction of a linear adsorbate dependency of roughly $E_{\Theta} = 1 \text{ kJ mol}^{-1}$ significantly enhances the description of the experiments and should not be omitted. It should be noted that this model has to be considered very carefully when applying it to describe the facet distribution in coprecipitated Cu/ZnO/ Al_2O_3 catalysts. In contrast to catalysts presented e.g. in ref. [8] and [9], the system in figure 7.4 is not considered a standard metal-support system with (faceted) copper nano-particles sitting on top of a bulk ZnO support, but rather a porous aggregate of quasi-spherical ZnO and Cu nanoparticles of equal size (see ref. [4]). Furthermore, parts of the copper spheres are covered with a partially reduced ZnO_x layer. Due to the complex three dimensional structure, with multiple different Cu-ZnO interfaces per particle, the description of such systems with the Wulff construction has to be examined very carefully. However, as Kuld et al. [5] recently showed, the oxidation state of the ZnO in Cu/ZnO/ Al_2O_3 catalysts can be influenced by the activation procedure and subsequently analyzed via H_2 -TPD and N_2O -RFC. In combination with a shape analysis of the H_2 desorption signal this could

be used to systematically control and analyze the extent of the SMSI effect in such heterogeneous systems and its influence on the signal shape.

In all experiments, the ratio of consumed N_2O to adsorbed H_2 is roughly 1.45, which corresponds with a $\text{Cu}:\text{H}_2$ adsorption stoichiometry of 2.9. This is in line with an atomic hydrogen saturation coverage of $2/3$ ML ($\text{Cu}:\text{H}_2 = 3$). Although, classically a coverage of $1/2$ ML is deduced from UHV studies, the formation of a $2/3$ ML coverage has been observed under higher adsorption pressures.[29, 30] Furthermore, it has recently been shown that the commonly assumed adsorption stoichiometry of $\text{Cu}:\text{H}_2 = 4$ in $\text{Cu}/\text{ZnO}/\text{Al}_2\text{O}_3$ catalysts suffers from an overestimation of the copper surface area by N_2O -experiments.[4, 5] Assuming a saturation H-coverage of $2/3$ ML and a mean copper surface atom density of $1.47 \cdot 10^{19}$ atoms per m^2 , the mean surface area of the polycrystalline copper sample C is $2.9 \text{ m}^2 \text{ g}_{\text{calc}}^{-1}$. This is in excellent agreement with the BET surface area of the activated sample C ($3.1 \text{ m}^2 \text{ g}_{\text{calc}}^{-1}$) and underlines the high sensitivity achievable with H_2 -TPD.

7.3.6 Conclusion

The exposed copper surface area of polycrystalline copper and a $\text{Cu}/\text{Al}_2\text{O}_3$ system was successfully characterized with hydrogen temperature programmed desorption. A comparison of the obtained signals points out that the alumina support has no significant influence on the desorption signal and that both systems can be described using the same mathematical models. It can be concluded from the results that the shift of the desorption maximum in $\text{Cu}/\text{ZnO}/\text{Al}_2\text{O}_3$ catalysts to higher temperatures is indeed a function of the Cu/ZnO synergy and is not directly correlated to a $\text{Cu}/\text{Al}_2\text{O}_3$ interaction. Furthermore, it was demonstrated that the desorption signal can be accurately described using a theoretically derived distribution of the low-index (100), (110) and (111) facets according to the Wulff construction for free copper crystals. Within the scope of copper based $\text{Cu}/\text{ZnO}/\text{Al}_2\text{O}_3$ methanol synthesis catalyst these experiments strengthen our understanding of the catalytic activity, which is determined by metal support interaction and by mutual influence of the specific catalyst components.

7.4 Supporting Information

The copper surface area according to H_2 -TPD and nitrous oxide reactive frontal chromatography (N_2O -RFC) are determined in a glass lined single-pass fixed-bed reactor (internal diameter 4.5 mm) with internal thermocouple, an upstream gas mixing unit and a mass spectrometer (Pfeiffer Vacuum OmniStar GSD 301 O) for time resolved in-situ analysis, which is calibrated prior to every measurement. The gas supply is optimized

for a minimal dead volume and each supply line is capable of dosing 0-100 sccm via calibrated mass flow controllers (Brooks 5850). A schematic representation of the setup is given in 7.6.

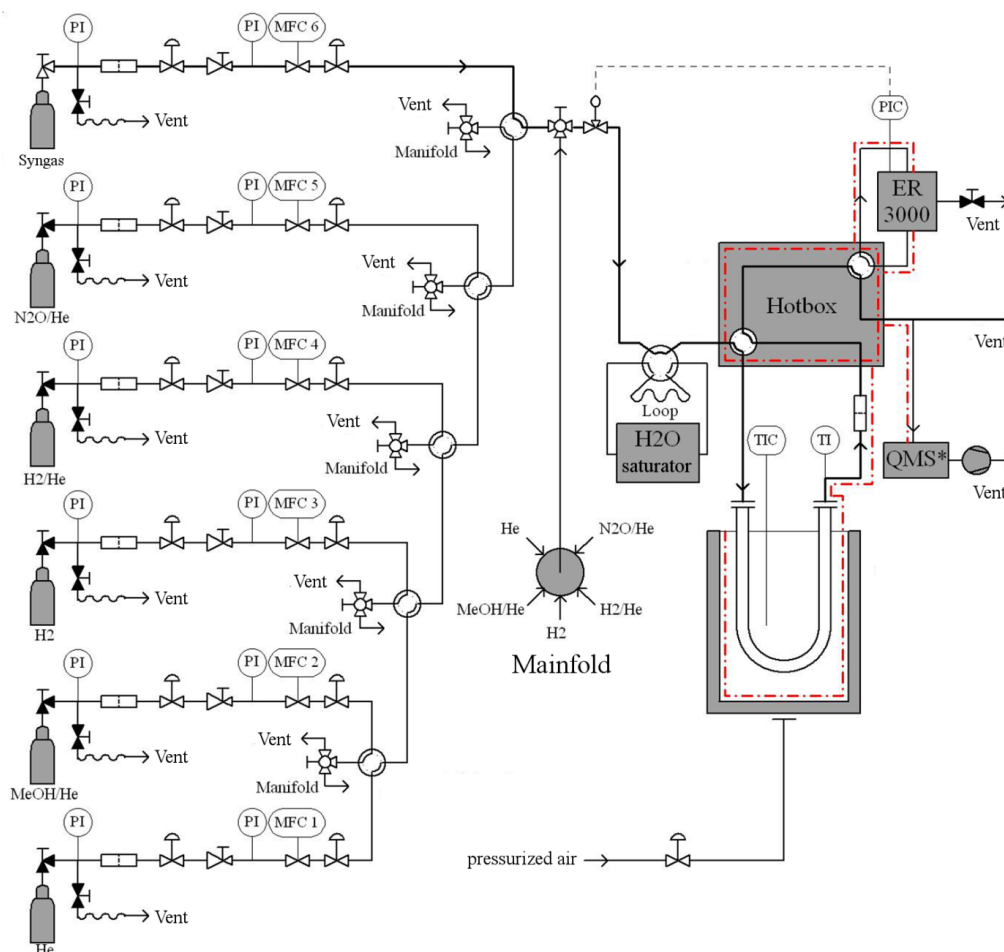


Figure 7.6: Flow schema of the H₂-TPD setup

The powdered sample is placed between two silica wool plugs in a U-shaped reactor which can be pressurized up to 28 bar. The electrically heated reactor block can be immersed in liquid nitrogen for rapid cooling and operated in a temperature range from 77 K up to 773 K. A thermocouple on top of the sample bed is used to measure the actual temperature inside the system. Using the gas mixing unit and the water saturator, also detailed kinetic experiments can be performed on the catalysts. In this case, a gas chromatograph (Agilent 7820A) equipped with two thermal conductivity detectors is employed to analyze the product mixture.

References

- [1] O. Hinrichsen, T. Genger, M. Muhler, *Chem. Eng. Technol.* **2000**, *23*, 956–959, DOI 10.1002/1521-4125(200011)23:11<956::AID-CEAT956>3.0.CO;2-L.
- [2] G. C. Chinchin, C. M. Hay, H. D. Vandervell, K. C. Waugh, *J. Catal.* **1987**, *103*, 79–86.
- [3] M. Kurtz, N. Bauer, C. Büscher, H. Wilmer, O. Hinrichsen, R. Becker, S. Rabe, K. Merz, M. Driess, R. A. Fischer, M. Muhler, *Catal. Lett.* **2004**, *92*, 49–52, DOI 10.1023/B:CATL.0000011085.88267.a6.
- [4] M. B. Fichtl, J. Schumann, I. Kasatkin, N. Jacobsen, M. Behrens, R. Schlögl, M. Muhler, O. Hinrichsen, *Angew. Chem. Int. Ed.* **2014**, *53*, 7043–7047, DOI 10.1002/anie.201400575.
- [5] S. Kuld, C. Conradsen, P. G. Moses, I. Chorkendorff, J. Sehested, *Angew. Chem. Int. Ed.* **2014**, *53*, 5941–5945, DOI 10.1002/anie.201311073.
- [6] H. Wilmer, T. Genger, O. Hinrichsen, *J. Catal.* **2003**, *215*, 188–198, DOI 10.1016/S0021-9517(03)00003-4.
- [7] G. Anger, A. Winkler, K. Rendulic, *Surf. Sci.* **1989**, *220*, 1–17, DOI 10.1016/0039-6028(89)90459-7.
- [8] P. L. Hansen, J. B. Wagner, S. Helveg, J. R. Rostrup-Nielsen, B. S. Clausen, H. Topsøe, *Science* **2002**, *295*, 2053–2055, DOI 10.1126/science.1069325.
- [9] J.-D. Grunwaldt, A. Molenbroek, N.-Y. Topsøe, H. Topsøe, B. S. Clausen, *J. Catal.* **2000**, *194*, 452–460, DOI 10.1006/jcat.2000.2930.
- [10] H. Wilmer, O. Hinrichsen, *Catal. Lett.* **2002**, *82*, 117–122, DOI 10.1023/A:1020560628950.
- [11] C. V. Ovesen, B. S. Clausen, J. Schiøtz, P. Stoltze, H. Topsøe, J. K. Nørskov, *J. Catal.* **1997**, *168*, 133–142, DOI 10.1006/jcat.1997.1629.
- [12] M. Peter, M. B. Fichtl, H. Ruland, S. Kaluza, M. Muhler, O. Hinrichsen, *Chem. Eng. Sci.* **2012**, *203*, 480–491, DOI 10.1016/j.cesj.2012.06.066.
- [13] P. C. Vesborg, I. Chorkendorff, I. Knudsen, O. Balmes, J. Nerlov, A. M. Molenbroek, B. S. Clausen, S. Helveg, *J. Catal.* **2009**, *262*, 65–72, DOI 10.1016/j.jcat.2008.11.028.
- [14] M. Behrens, F. Studt, I. Kasatkin, S. Kühl, M. Hävecker, F. Abild-Pedersen, S. Zander, F. Girgsdies, P. Kurr, B.-L. Kniep, M. Tovar, R. W. Fischer, J. K. Nørskov, R. Schlögl, *Science* **2012**, *336*, 893–897, DOI 10.1126/science.1219831.

- [15] T. Fujitani, J. Nakamura, *Appl Cat A* **2000**, *191*, 111–129, DOI 10.1016/S0926-860X(99)00313-0.
- [16] M. Sano, T. Adaniya, T. Fujitani, J. Nakamura, *J. Phys. Chem. B* **2002**, *106*, 7627–7633, DOI 10.1021/jp012810i.
- [17] M. Behrens, S. Zander, P. Kurr, N. Jacobsen, J. Senker, G. Koch, T. Ressler, R. W. Fischer, R. Schlögl, *J. Am. Chem. Soc.* **2013**, *135*, 6061–6068, DOI 10.1021/ja310456f.
- [18] M. Behrens, R. Schlögl, *Z. Anorg. Allg. Chem.* **2013**, *639*, 2683–2695, DOI 10.1002/zaac.201300356.
- [19] O. Hinrichsen, T. Genger, M. Muhler in *Studies in Surface Science and Catalysis*, (Eds.: A. Corma, F. V. Melo, S. Mendioroz, J. L. G. Fierro), 12th International Congress on Catalysis Proceedings of the 12th ICC, Elsevier, **2000**, pp. 3825–3830.
- [20] J. Kanervo, T. Keskitalo, R. Slioor, A. Krause, *J. Catal.* **2006**, *238*, 382–393, DOI 10.1016/j.jcat.2005.12.026.
- [21] M. Peter, J. Fendt, H. Wilmer, O. Hinrichsen, *Catal. Lett.* **2012**, *142*, 547–556, DOI 10.1007/s10562-012-0807-3.
- [22] M. Peter, J. Fendt, S. Pleintinger, O. Hinrichsen, *Catal. Sci. Technol* **2012**, *2*, 2249–2257, DOI 10.1039/c2cy20189e.
- [23] W. Kaminsky, *J. Appl. Crystallogr.* **2005**, *38*, 566–567, DOI 10.1107/S00218898-05012148.
- [24] W. Kaminsky, *J. Appl. Crystallogr.* **2007**, *40*, 382–385, DOI 10.1107/S00218898-07003986.
- [25] L. Vitos, A. V. Ruban, H. L. Skriver, J. Kollár, *Surf. Sci.* **1998**, *411*, 186–202, DOI 10.1016/S0039-6028(98)00363-X.
- [26] C. T. Campbell, *Nature Chemistry* **2012**, *4*, 597–598, DOI 10.1038/nchem.1412.
- [27] J. M. Herrmann, *J. Catal.* **1984**, *89*, 404–412, DOI 10.1016/0021-9517(84)90316-6.
- [28] V. Schott, H. Oberhofer, A. Birkner, M. Xu, Y. Wang, M. Muhler, K. Reuter, C. Wöll, *Angew. Chem. Int. Ed.* **2013**, *52*, 11925–11929, DOI 10.1002/anie.201302315.
- [29] G. Lee, D. B. Poker, D. M. Zehner, E. W. Plummer, *Surf. Sci.* **1996**, *357-358*, 717–720, DOI 10.1016/0039-6028(96)00252-X.
- [30] E. M. Mccash, S. F. Parker, J. Pritchard, M. A. Chesters, *Surf. Sci.* **1989**, *215*, 363–377, DOI 10.1016/0039-6028(89)90266-5.

8 Closing

8.1 Summary

Methanol is a well established, versatile energy carrier and C1 building block which will gain further importance in the future. Although the synthesis over Cu/ZnO/Al₂O₃ based catalysts has been known for over 50 years, much insight can still be gained. Apart from the "real" active site of the catalyst, further important factors like the detailed deactivation behavior and mechanisms to prevent this loss in activity are still not unambiguously clear.

In the first part of this thesis selected high performance Cu/ZnO/Al₂O₃ catalysts are aged under constant conditions and systematically analyzed. A typical industrially applied temperature of 523 K and a pressure of 60 bar are employed. The catalysts are characterized directly after activation, 240, 480, 720, and 960 h time on stream (TOS) via elemental analysis, (high resolution) transmission electron spectroscopy (HR-TEM), x-ray diffraction (XRD), nitrogen physisorption (BET), H₂-TPD, N₂O-RFC and kinetic experiments. By combining elemental analysis and TEM - energy dispersive x-ray spectroscopy (TEM-EDX), the local microstructure of the catalysts is explored. Depending on the preparation method and metal concentration, the catalysts mainly exhibit ex-zinc-malachite (Cu,Zn)₂(OH)₂(CO₃)₂ (ZMT), ex-aurichalcite (Cu,Zn)₅(CO₃)₂(OH)₆ (ACT), and hydrotalcite like (Cu,Zn)_{1-x}Al_x(OH)₂(CO₃)_{x/2} structures. The results from the TEM particle size distributions and XRD experiments allow the conclusion that the mean copper particle size increases in the ZMT regions of catalysts, whereas HTL and ACT structures show no significant change in the particle size. This can further be connected with the microstructural environment: in the alumina rich HTL structure, the copper particles are embedded in a compact matrix of zinc alumina spinel and amorphous oxides. This stable matrix keeps the particles well apart so that they show no sintering behavior during the whole deactivation period. Analogously the copper particles are strongly embedded in a ZnO matrix in ACT structures.

The alumina depleted ZMT phases are characterized by an open microstructure where copper particles are partially covered with ZnO_x species and kept apart by ZnO. During the aging process sintering of the copper particles is observed and new twinning sites

are generated due to particle contact. Furthermore, the formation of a crystalline zinc alumina spinel phase ZnAl_2O_4 as well as $\gamma\text{-Al}_2\text{O}_3$ and an amorphous overlay over some of the copper particles are observed. Another important key aspect is that in the ZMT phase not only the particle size of copper increases, but also the particle size of ZnO. In combination with the indication that copper twinning boundaries are stable under synthesis conditions, this allows a reinterpretation of the deactivation mechanism in methanol synthesis catalysts: sintering of copper particles does not occur by classic mechanisms like Ostwald Ripening, but is rather described by a leaching of the mobile spacer ZnO, leading to copper particle contact and agglomeration. Although the typical temperatures in methanol synthesis are much too low to promote sintering of ZnO, this may happen due to the strong Cu-ZnO interaction (SMSI effect). This is also supported by an analysis of the particle size distributions derived via TEM measurements: a modeling study of the sintering mechanisms leads to the conclusion that sintering of copper particles does not depend on the particle radius, but rather follows a random collision of the nanoparticles. In excess of alumina this sintering effect may be accelerated by the crystallization of ZnAl_2O_4 which acts as a sink for the formerly mobile ZnO species. In the ACT and HTL structure the copper particles are well stabilized by embedding them in either a partially amorphous ZnO or an amorphous $\text{ZnO}/\text{Al}_2\text{O}_3$ matrix respectively. However, the strong embedding and the strong Cu-ZnO interaction block active sites in both cases and reduce the specific activity.

A detailed analysis of the deactivation behavior of three structural different high performance systems is performed. By cycling the systems between a 20 h long equilibrium condition aging period and a short-term kinetic measurement to determine the catalyst activity, data about the time dependent activity is gathered. Simultaneously, all catalysts are aged under the same (equilibrium) conditions. During the aging period temperatures of 493 K, 523 K and 553 K at a pressure of 60 bar are applied. The results indicate that the deactivation process can be described with an empiric power law equation of third and fourth order respectively. The catalysts lose approximately 40% of the initial activity during the first 1000 h TOS. An analysis of the respective activation energies of fresh and spent catalysts leads to the conclusion that the deactivation process reduces the amount of active sites rather than changing the reaction mechanism. Furthermore, it is shown that the variation in aging temperature has significant influence on the deactivation process; however, a correlation between aging temperature and the rate constant of the deactivation cannot be established. The results indicate that this may be attributed to the change in the equilibrium gas atmosphere with temperature. The water content in the reactor was identified to have significant influence on the deactivation rate constant.

Although, the presented deactivation mechanism for ZMT systems can be explained using sintering phenomena, the deactivation of strongly embedded ACT and HTL phases does not follow this schema. In all cases, no increase in the mean copper particle is detected in the spent catalysts, which leads to the conclusion that deactivation also may occur upon changes in the Cu-ZnO interaction. These interactions and changes therein can be tracked using surface-sensitive techniques like temperature programmed H₂-desorption (H₂-TPD). An analysis of the aged catalysts leads to the conclusion that during the deactivation process a low temperature signal evolves, which cannot be assigned to a known copper surface structure. Furthermore, an oxidative treatment of these systems leads to a reconstruction of the surface structure leading to a higher metal surface area according to H₂-TPD and a partial recovery of the catalytic activity. Based on the results it is safe to conclude that the copper particles are increasingly covered with a, yet unknown, surface species, blocking them from the gas atmosphere and reducing the number of active sites. This surface species can be partially removed by oxidizing the catalyst.

Further analysis of the fresh catalyst samples via H₂-TPD and nitrous oxide reactive frontal chromatography N₂O-RFC unravels significant differences in the respective metal surface area. In a systematic study polycrystalline copper and copper supported on Al₂O₃ and MgO is analyzed via H₂-TPD and N₂O-RFC, and compared with measurements of ZnO containing catalyst samples. The results allow the conclusion that in absence of ZnO a linear correlation between the copper surface area according to both methods can be established. However, in presence of ZnO, the copper surface area according to N₂O-RFC is significantly overestimated due to the presence of ZnO_x defect sites which are generated at the Cu/ZnO interface. It is further shown, that the saturation coverage of copper with hydrogen atoms is reached at 2/3 ML, i.e. three copper atoms bind 2 hydrogen atoms. A combination of N₂O-RFC and H₂-TPD can also be used to calculate the present ZnO_x defect concentration. The catalyst activity, however, cannot be correlated with the "true" metal surface area determined by H₂-TPD, but rather with a combination of surface area and defect concentration, as determined by N₂O-RFC. This underlines the fact that methanol synthesis is a structure sensitive reaction.

Improvements in the H₂-TPD technique allow the precise measurement of very low copper surface areas like the one of polycrystalline copper. For the first time, the H₂ desorption kinetic from pure copper is measured under ambient conditions and model parameters for a second order desorption kinetic are determined. A comparison with the desorption kinetic from Al₂O₃ supported copper leads to the conclusion that the Al₂O₃ support has no significant influence on the desorption process and hence on the electronic structure of the copper surface. Furthermore, it is shown that the desorption signals

can also be described by three single desorption processes from a theoretically derived combination of the copper low index planes Cu(111), Cu(110) and Cu(100). From these results it can be assumed that copper has no significantly preferred adsorption orientation on Al_2O_3 .

8.2 Outlook

Deactivation of methanol synthesis catalysts is a complicated and diverse process. From the presented data it can be concluded that long-term aging studies combined with a detailed analysis are a versatile tool to understand the various implications of the catalyst characteristics. With respect to further studies, the most important key result is that the intrinsic deactivation does not only occur due to simple sintering mechanisms, but is strongly dependent on the catalyst microstructure.

Although it is shown, that mobility of ZnO plays an important role in the deactivation mechanism, the factors inducing this mobility and hence the deactivation by collision of copper particles, are not yet known. Especially the role of water should be investigated, as this leads to dramatic catalyst deactivation. Possible mechanism to explain this influence might be the formation of surface bound but mobile $\text{Zn}(\text{OH})_x$ species or the influence of H_2O on the Cu/ZnO_x reduction state. Another possible mechanism involves the removal of Al^{3+} dopants, which stabilize oxygen defect sites in the ZnO_x matrix. However, without further experiments and surface-sensitive characterization methods no reliable prognosis of the deactivation behavior is possible.

In case of ZnO rich catalysts, where no copper particle sintering is observed at all, also a second deactivation mechanism has to be considered and analyzed. It has been shown that this mechanism has influence on the copper surface characteristics and might be explained via a Cu-Zn surface alloy or a strong adsorbate structure like carbon deposition. Here, combined H_2 -TPD and IR/Raman spectroscopy might give further insight into the copper surface decoration.

With the knowledge that the deactivation mechanisms are dependent on the catalyst's microstructure, it should also be possible to tailor catalysts for higher durability - i.e. by modifying the ZnO spacer structure for higher stability. A major prerequisite for that is a sound understanding of the synthesis parameters, leading to such modified catalysts and of the methods used to characterize such systems. The possibility to separately quantify the true metal surface area and the ZnO_x defect structure by combining H_2 -TPD and N_2O -RFC will help to understand the general structure of high-performance catalysts.

Summarizing all the presented results it can be concluded that the deactivation mechanisms of copper catalysts - not unlikely the catalyst activity - are not just defined by the single catalyst components. They are extensively influenced by the specific

interactions of these and form a system which has to be considered as a whole in order to really understand the processes going on.

Curriculum Vitae

Personal

Name: Matthias Benedikt Fichtl
Date of birth: 05.06.1985
Place of birth: Buchloe
Nationality: German

Education

2010 – present **Ph.D. Candidate (Dr.rer.nat.)**
Technical University Munich (Germany)
Chair of Chemical Engineering
Prof. Dr.-Ing. Kai-Olaf Hinrichsen
Topic: "Efficient Methanol Synthesis Catalysts: Long-Term Stability and Deactivation Phenomena"

2008 – 2010 **Master of Science, Chemistry**
Technical University Munich (Germany)
Major: Technical Chemistry, Minor: Macromolecular Chemistry
Thesis: "Synthesis and Characterization of Novel Fluorides"
Grade 1.2 "passed with high distinction"

2005 – 2008 **Bachelor of Science, Chemistry**
Technical University Munich (Germany)

Thesis: "Synthesis of transition metal ammoniates in liquid ammonia and structural review of $K_2SiF_6 \cdot KF$ "
Grade 1.6 "passed with merit"

2004

Abitur, (A-levels)

Jakob-Brucker-Gymnasium Kaufbeuren

Main subjects: Chemistry, Physics

Grade 1.4 "very good"

Alternative military service

2004

Urban administration of Kaufbeuren (Germany)

Janitor assistant in the town-hall of Kaufbeuren.

Publications

Journal Publications

- F. Kraus, S. A. Baer, M. B. Fichtl, *The Reactions of Silver, Zirconium, and Hafnium Fluorides with Liquid Ammonia: Syntheses and Crystal Structures of $Ag(NH_3)_2F \cdot 2NH_3$, $[M(NH_3)_4F_4] \cdot NH_3$ ($M = Zr, Hf$), and $(N_2H_7)F$* , Eur. J. Inorg. Chem. **2009**, 3, 441-447.
- F. Kraus, M. B. Fichtl, S. A. Baer, *Beryllium Diammine Difluoride $[BeF_2(NH_3)_2]$* , Z. Naturforsch.(B) **2009**, 64, 257-262.
- M. B. Fichtl, L. M. Scherf, S. A. Baer, F. Kraus, *μ -Oxido-bis(pentammine iron(III))-chloride-ammonia(1/8), $[Fe_2(\mu O)(NH_3)_{10}]Cl_4 \cdot 8NH_3$* , Z.Naturforsch.(B) **2011**, 66, 784-792.
- M. Salzinger, M. B. Fichtl, J. A. Lercher, *On the influence of pore geometry and acidity on the activity of parent and modified zeolites in the synthesis of methylenedianiline*, Appl. Catal. A **2011**, 393, 189-194.
- M. Peter, M. B. Fichtl, H. Ruland, S. Kaluza, M. Muhler, O. Hinrichsen, *Detailed kinetic modeling of methanol synthesis over a ternary copper catalyst*, Chem. Eng. Sci. **2012**, 203, 480-491.
- M. B. Fichtl, J. Schumann, I. Kasatkin, N. Jacobsen, M. Behrens, R. Schlögl, M. Muhler, O. Hinrichsen, *Counting of oxygen defects vs. metal surface sites in methanol synthesis catalysts by different probe molecules*, Angew. Chem. Int. Ed. **2014**, 53, 7043-7047.
- M. B. Fichtl, J. Schumann, N. Jacobsen, W. Busser, M. Muhler, M. Behrens, R. Schlögl, O. Hinrichsen, *Deactivation mechanisms on Cu/ZnO/Al₂O₃ methanol synthesis catalysts*, in preparation.
- M. B. Fichtl, D. Schlereth, N. Jacobsen, I. Kasatkin, J. Schumann, M. Behrens, R. Schlögl, O. Hinrichsen, *Kinetics of deactivation on Cu/ZnO/Al₂O₃ methanol synthesis catalysts*, in preparation.

- M. B. Fichtl, O. Hinrichsen, *On the temperature programmed desorption of hydrogen from polycrystalline copper*, Catal. Lett. **2014**, accepted.

Selected conference papers

- M. B. Fichtl, O. Hinrichsen, *Efficient Methanol Synthesis Catalysts: Long-Term Stability and Modelling of Deactivation*, MSE Kolloquium - Sustainable Energy Supply of the Future (Garching, **2011**) .
- M. B. Fichtl, O. Hinrichsen, *Effiziente Methanolsynthese-Katalysatoren Langzeitstabilität und Desaktivierungsverhalten*, 45. Jahrestreffen Deutscher Katalytiker (Weimar, **2012**) .
- M. B. Fichtl, O. Hinrichsen, *Efficient Methanol Synthesis Catalysts: Long-Term Stability and Deactivation Phenomena*, 15th International Congress on Catalysis 2012 (München, **2012**).
- M. B. Fichtl, O. Hinrichsen, *Efficient Methanol Synthesis Catalysts: Long-Term Stability and Deactivation Phenomena* , 46. Jahrestreffen Deutscher Katalytiker (Weimar, **2013**).
- M. B. Fichtl, O. Hinrichsen, *Efficient Methanol Synthesis Catalysts: Long-Term Stability and Deactivation Phenomena*, 528. WE-Heraeus-Seminar "Energy-Related Catalysis Today and Tomorrow: From Fundamentals to Application" (Bad Honnef, **2013**).
- M.B. Fichtl, O. Hinrichsen, *Efficient Methanol Synthesis Catalysts: Long-Term Stability and Deactivation Phenomena*, XIth European Congress on Catalysis (Lyon, **2013**).
- M.B. Fichtl, O. Hinrichsen, *Comparative in situ characterization of the copper metal surface area in methanol synthesis catalysts*, 47. Jahrestreffen Deutscher Katalytiker (Weimar, **2014**).

Licensing Information

Chapter 6 has been published in a peer-reviewed journal: M. B. Fichtl, J. Schumann, I. Kasatkin, N. Jacobsen, M. Behrens, R. Schlögl, M. Muhler, O. Hinrichsen, *Counting of oxygen defects vs. metal surface sites in methanol synthesis catalysts by different probe molecules*, *Angew. Chem. Int. Ed.* **2014**, 53, 7043-7047.

License for Chapter 6

JOHN WILEY AND SONS LICENSE TERMS AND CONDITIONS



Jun 28, 2014

This is a License Agreement between Matthias B Fichtl ("You") and John Wiley and Sons ("John Wiley and Sons") provided by Copyright Clearance Center ("CCC"). The license consists of your order details, the terms and conditions provided by John Wiley and Sons, and the payment terms and conditions.

All payments must be made in full to CCC. For payment instructions, please see information listed at the bottom of this form.

License Number	3417560772976
License date	Jun 28, 2014
Licensed content publisher	John Wiley and Sons
Licensed content publication	Angewandte Chemie International Edition
Licensed content title	Counting of Oxygen Defects versus Metal Surface Sites in Methanol Synthesis Catalysts by Different Probe Molecules
Licensed copyright line	© 2014 WILEY-VCH Verlag GmbH & Co. KGaA, Weinheim
Licensed content author	Matthias B. Fichtl, Julia Schumann, Igor Kasatkin, Nikolas Jacobsen, Malte Behrens, Robert Schlögl, Martin Muhler, Olaf Hinrichsen
Licensed content date	May 21, 2014
Start page	7043
End page	7047
Type of use	Dissertation/Thesis
Requestor type	Author of this Wiley article
Format	Print and electronic
Portion	Full article
Will you be translating?	No
Title of your thesis / dissertation	Efficient Methanol Synthesis Catalysts: Long-Term Stability and Deactivation Phenomena
Expected completion date	Aug 2014
Expected size (number of pages)	130
Total	0.00 EUR
Terms and Conditions	

TERMS AND CONDITIONS

This copyrighted material is owned by or exclusively licensed to John Wiley & Sons, Inc. or one of its group companies (each a "Wiley Company") or handled on behalf of a society with which a Wiley Company has exclusive publishing rights in relation to a particular work (collectively "WILEY"). By clicking  accept  in connection with completing this licensing transaction, you agree that the following terms and conditions apply to this transaction (along with the billing and payment terms and conditions established by the Copyright Clearance Center Inc., ("CCC's Billing and Payment terms and conditions"), at

the time that you opened your Rightslink account (these are available at any time at <http://myaccount.copyright.com>).

Terms and Conditions

- The materials you have requested permission to reproduce or reuse (the "Wiley Materials") are protected by copyright.
- You are hereby granted a personal, non-exclusive, non-sub licensable (on a stand-alone basis), non-transferable, worldwide, limited license to reproduce the Wiley Materials for the purpose specified in the licensing process. This license is for a one-time use only and limited to any maximum distribution number specified in the license. The first instance of republication or reuse granted by this licence must be completed within two years of the date of the grant of this licence (although copies prepared before the end date may be distributed thereafter). The Wiley Materials shall not be used in any other manner or for any other purpose, beyond what is granted in the license. Permission is granted subject to an appropriate acknowledgement given to the author, title of the material/book/journal and the publisher. You shall also duplicate the copyright notice that appears in the Wiley publication in your use of the Wiley Material. Permission is also granted on the understanding that nowhere in the text is a previously published source acknowledged for all or part of this Wiley Material. Any third party content is expressly excluded from this permission.
- With respect to the Wiley Materials, all rights are reserved. Except as expressly granted by the terms of the license, no part of the Wiley Materials may be copied, modified, adapted (except for minor reformatting required by the new Publication), translated, reproduced, transferred or distributed, in any form or by any means, and no derivative works may be made based on the Wiley Materials without the prior permission of the respective copyright owner. You may not alter, remove or suppress in any manner any copyright, trademark or other notices displayed by the Wiley Materials. You may not license, rent, sell, loan, lease, pledge, offer as security, transfer or assign the Wiley Materials on a stand-alone basis, or any of the rights granted to you hereunder to any other person.
- The Wiley Materials and all of the intellectual property rights therein shall at all times remain the exclusive property of John Wiley & Sons Inc, the Wiley Companies, or their respective licensors, and your interest therein is only that of having possession of and the right to reproduce the Wiley Materials pursuant to Section 2 herein during the continuance of this Agreement. You agree that you own no right, title or interest in or to the Wiley Materials or any of the intellectual property rights therein. You shall have no rights hereunder other than the license as provided for above in Section 2. No right, license or interest to any trademark, trade name, service mark or other branding ("Marks") of WILEY or its licensors is granted hereunder, and you agree that you shall not assert any such right, license or interest with respect thereto.
- NEITHER WILEY NOR ITS LICENSORS MAKES ANY WARRANTY OR REPRESENTATION OF ANY KIND TO YOU OR ANY THIRD PARTY, EXPRESS, IMPLIED OR STATUTORY, WITH RESPECT TO THE MATERIALS OR THE ACCURACY OF ANY INFORMATION CONTAINED IN THE MATERIALS, INCLUDING, WITHOUT LIMITATION, ANY IMPLIED

WARRANTY OF MERCHANTABILITY, ACCURACY, SATISFACTORY QUALITY, FITNESS FOR A PARTICULAR PURPOSE, USABILITY, INTEGRATION OR NON-INFRINGEMENT AND ALL SUCH WARRANTIES ARE HEREBY EXCLUDED BY WILEY AND ITS LICENSORS AND WAIVED BY YOU

- WILEY shall have the right to terminate this Agreement immediately upon breach of this Agreement by you.
- You shall indemnify, defend and hold harmless WILEY, its Licensors and their respective directors, officers, agents and employees, from and against any actual or threatened claims, demands, causes of action or proceedings arising from any breach of this Agreement by you.
- IN NO EVENT SHALL WILEY OR ITS LICENSORS BE LIABLE TO YOU OR ANY OTHER PARTY OR ANY OTHER PERSON OR ENTITY FOR ANY SPECIAL, CONSEQUENTIAL, INCIDENTAL, INDIRECT, EXEMPLARY OR PUNITIVE DAMAGES, HOWEVER CAUSED, ARISING OUT OF OR IN CONNECTION WITH THE DOWNLOADING, PROVISIONING, VIEWING OR USE OF THE MATERIALS REGARDLESS OF THE FORM OF ACTION, WHETHER FOR BREACH OF CONTRACT, BREACH OF WARRANTY, TORT, NEGLIGENCE, INFRINGEMENT OR OTHERWISE (INCLUDING, WITHOUT LIMITATION, DAMAGES BASED ON LOSS OF PROFITS, DATA, FILES, USE, BUSINESS OPPORTUNITY OR CLAIMS OF THIRD PARTIES), AND WHETHER OR NOT THE PARTY HAS BEEN ADVISED OF THE POSSIBILITY OF SUCH DAMAGES. THIS LIMITATION SHALL APPLY NOTWITHSTANDING ANY FAILURE OF ESSENTIAL PURPOSE OF ANY LIMITED REMEDY PROVIDED HEREIN.
- Should any provision of this Agreement be held by a court of competent jurisdiction to be illegal, invalid, or unenforceable, that provision shall be deemed amended to achieve as nearly as possible the same economic effect as the original provision, and the legality, validity and enforceability of the remaining provisions of this Agreement shall not be affected or impaired thereby.
- The failure of either party to enforce any term or condition of this Agreement shall not constitute a waiver of either party's right to enforce each and every term and condition of this Agreement. No breach under this agreement shall be deemed waived or excused by either party unless such waiver or consent is in writing signed by the party granting such waiver or consent. The waiver by or consent of a party to a breach of any provision of this Agreement shall not operate or be construed as a waiver of or consent to any other or subsequent breach by such other party.
- This Agreement may not be assigned (including by operation of law or otherwise) by you without WILEY's prior written consent.
- Any fee required for this permission shall be non-refundable after thirty (30) days from receipt by the CCC.
- These terms and conditions together with CCC's Billing and Payment terms and

conditions (which are incorporated herein) form the entire agreement between you and WILEY concerning this licensing transaction and (in the absence of fraud) supersedes all prior agreements and representations of the parties, oral or written. This Agreement may not be amended except in writing signed by both parties. This Agreement shall be binding upon and inure to the benefit of the parties' successors, legal representatives, and authorized assigns.

- In the event of any conflict between your obligations established by these terms and conditions and those established by CCC's Billing and Payment terms and conditions, these terms and conditions shall prevail.
- WILEY expressly reserves all rights not specifically granted in the combination of (i) the license details provided by you and accepted in the course of this licensing transaction, (ii) these terms and conditions and (iii) CCC's Billing and Payment terms and conditions.
- This Agreement will be void if the Type of Use, Format, Circulation, or Requestor Type was misrepresented during the licensing process.
- This Agreement shall be governed by and construed in accordance with the laws of the State of New York, USA, without regards to such state's conflict of law rules. Any legal action, suit or proceeding arising out of or relating to these Terms and Conditions or the breach thereof shall be instituted in a court of competent jurisdiction in New York County in the State of New York in the United States of America and each party hereby consents and submits to the personal jurisdiction of such court, waives any objection to venue in such court and consents to service of process by registered or certified mail, return receipt requested, at the last known address of such party.

WILEY OPEN ACCESS TERMS AND CONDITIONS

Wiley Publishes Open Access Articles in fully Open Access Journals and in Subscription journals offering Online Open. Although most of the fully Open Access journals publish open access articles under the terms of the Creative Commons Attribution (CC BY) License only, the subscription journals and a few of the Open Access Journals offer a choice of Creative Commons Licenses: Creative Commons Attribution (CC-BY) license [Creative Commons Attribution Non-Commercial \(CC-BY-NC\) license](#) and [Creative Commons Attribution Non-Commercial-NoDerivs \(CC-BY-NC-ND\) License](#). The license type is clearly identified on the article.

Copyright in any research article in a journal published as Open Access under a Creative Commons License is retained by the author(s). Authors grant Wiley a license to publish the article and identify itself as the original publisher. Authors also grant any third party the right to use the article freely as long as its integrity is maintained and its original authors, citation details and publisher are identified as follows: [Title of Article/Author/Journal Title and Volume/Issue. Copyright (c) [year] [copyright owner as specified in the Journal]. Links to the final article on Wiley's website are encouraged where applicable.

The Creative Commons Attribution License

The [Creative Commons Attribution License \(CC-BY\)](#) allows users to copy, distribute and transmit an article, adapt the article and make commercial use of the article. The CC-BY license permits commercial and non-commercial re-use of an open access article, as long as the author is properly attributed.

The Creative Commons Attribution License does not affect the moral rights of authors, including without limitation the right not to have their work subjected to derogatory treatment. It also does not affect any other rights held by authors or third parties in the article, including without limitation the rights of privacy and publicity. Use of the article must not assert or imply, whether implicitly or explicitly, any connection with, endorsement or sponsorship of such use by the author, publisher or any other party associated with the article.

For any reuse or distribution, users must include the copyright notice and make clear to others that the article is made available under a Creative Commons Attribution license, linking to the relevant Creative Commons web page.

To the fullest extent permitted by applicable law, the article is made available as is and without representation or warranties of any kind whether express, implied, statutory or otherwise and including, without limitation, warranties of title, merchantability, fitness for a particular purpose, non-infringement, absence of defects, accuracy, or the presence or absence of errors.

Creative Commons Attribution Non-Commercial License

The [Creative Commons Attribution Non-Commercial \(CC-BY-NC\) License](#) permits use, distribution and reproduction in any medium, provided the original work is properly cited and is not used for commercial purposes.(see below)

Creative Commons Attribution-Non-Commercial-NoDerivs License

The [Creative Commons Attribution Non-Commercial-NoDerivs License](#) (CC-BY-NC-ND) permits use, distribution and reproduction in any medium, provided the original work is properly cited, is not used for commercial purposes and no modifications or adaptations are made. (see below)

Use by non-commercial users

For non-commercial and non-promotional purposes, individual users may access, download, copy, display and redistribute to colleagues Wiley Open Access articles, as well as adapt, translate, text- and data-mine the content subject to the following conditions:

- The authors' moral rights are not compromised. These rights include the right of "paternity" (also known as "attribution" - the right for the author to be identified as such) and "integrity" (the right for the author not to have the work altered in such a way that the author's reputation or integrity may be impugned).
- Where content in the article is identified as belonging to a third party, it is the obligation of the user to ensure that any reuse complies with the copyright policies of the owner of that content.
- If article content is copied, downloaded or otherwise reused for non-commercial

research and education purposes, a link to the appropriate bibliographic citation (authors, journal, article title, volume, issue, page numbers, DOI and the link to the definitive published version on **Wiley Online Library**) should be maintained. Copyright notices and disclaimers must not be deleted.

- Any translations, for which a prior translation agreement with Wiley has not been agreed, must prominently display the statement: "This is an unofficial translation of an article that appeared in a Wiley publication. The publisher has not endorsed this translation."

Use by commercial "for-profit" organisations

Use of Wiley Open Access articles for commercial, promotional, or marketing purposes requires further explicit permission from Wiley and will be subject to a fee. Commercial purposes include:

- Copying or downloading of articles, or linking to such articles for further redistribution, sale or licensing;
- Copying, downloading or posting by a site or service that incorporates advertising with such content;
- The inclusion or incorporation of article content in other works or services (other than normal quotations with an appropriate citation) that is then available for sale or licensing, for a fee (for example, a compilation produced for marketing purposes, inclusion in a sales pack)
- Use of article content (other than normal quotations with appropriate citation) by for-profit organisations for promotional purposes
- Linking to article content in e-mails redistributed for promotional, marketing or educational purposes;
- Use for the purposes of monetary reward by means of sale, resale, licence, loan, transfer or other form of commercial exploitation such as marketing products
- Print reprints of Wiley Open Access articles can be purchased from:
corporatesales@wiley.com

Further details can be found on Wiley Online Library <http://olabout.wiley.com/WileyCDA/Section/id-410895.html>

Other Terms and Conditions:

v1.9

If you would like to pay for this license now, please remit this license along with your payment made payable to "COPYRIGHT CLEARANCE CENTER" otherwise you will be

invoiced within 48 hours of the license date. Payment should be in the form of a check or money order referencing your account number and this invoice number 501338995. Once you receive your invoice for this order, you may pay your invoice by credit card. Please follow instructions provided at that time.

Make Payment To:
Copyright Clearance Center
Dept 001
P.O. Box 843006
Boston, MA 02284-3006

For suggestions or comments regarding this order, contact RightsLink Customer Support: customercare@copyright.com or +1-877-622-5543 (toll free in the US) or +1-978-646-2777.

Gratis licenses (referencing \$0 in the Total field) are free. Please retain this printable license for your reference. No payment is required.

List of Figures

1.1	Typical distribution of products derived from methanol.[3, 4]	2
2.1	Equilibrium MeOH yield as a function of pressure and temperature. Synthesis gas composition: 13.5% CO, 3.5% CO ₂ , 73.5% H ₂ , 9.5% N ₂ . . .	7
2.2	Schematic of the Lurgi MegaMethanol [®] methanol reactor concept.[18] . .	8
2.3	Most abundant surface intermediates in copper based methanol synthesis catalysts.	9
2.4	Simplified preparation scheme for Cu/ZnO/Al ₂ O ₃ systems and TEM im- ages of the different preparation stages	11
2.5	HR-TEM image of an activated ex-zinc-malachite catalyst.[60]	13
2.6	Simplified flow diagram for a two-step reforming process and integrated methanol plant.[74]	15
2.7	Deactivation behavior according to selected literature-known power law models. The solid lines represent gas phase reactions and the dashed lines slurry reactors. Reproduction of data presented in [87] and [88].	18
3.1	Experimental setup for the precipitation of copper catalysts.	26
3.2	Exemplary TPR-TG-MS study of a Cu/ZnO/Al ₂ O ₃ system. The dotted lines represent the CO ₂ and H ₂ O content in the purge gas atmosphere. . .	27
3.3	Schematic representation of the kinetic setup for long-term deactivation studies.	28
3.4	Front view of the final setup for long-term deactivation experiments. . . .	29
3.5	View of the four parallel fixed bed reactors in the heating chamber and the attached shutoff valves.	29
3.6	Exemplary results of a combined GC-MS measurement.	30
3.7	Flow scheme of the setup for transient experiments.	31
3.8	Schema of the heating block and attached cooling bath.	32
4.1	Catalyst activity of CZA1, CZA2 and CZA3 as a function of TOS (left) and corresponding specific copper surface area (right).	41

4.2	(left)EDX-results of the local composition of CZA2 during the aging period and an exemplary TEM image of the correlating microstructure (right).	42
4.3	Deactivation behavior of Cu Particles in the governing HTL and ZMT phases.	43
4.4	Top: Porous microstructure of the ZMT phase in the activated catalysts. Bottom: Embedding of copper particles in a partially amorphous ZnAl_2O_4 ("Sp") matrix in the HTL phase (left) and formation of new twinning boundaries at the grain boundary of contacting particles (right).	44
4.5	Exemplary diffraction pattern of CZA1(left) and CZA5(right) after activation and 40 days TOS.	45
4.6	Evolution of pseudo-crystallite sizes of Cu and ZnO (left) and of the d-values of the lower angle (circles, right) shoulder and of the Cu 200 main reflection (triangles, right) with time on stream.	46
4.7	(left) BET Surface area and average pore diameter of the fresh activated and aged catalysts. (right) Development of the pore size distribution of CZA2 which stands exemplary for the other samples.	48
4.8	(left) Reproduction H_2 -TPD experiments of the fresh and aged (TOS = 40 d) CZA1 catalyst samples. (right) Shift of the H_2 desorption signal during the aging treatment for 40 d and after oxidation/reduction of the aged sample.	49
4.9	Correlation of the specific copper surface area (measured by N_2O -RFC) with the catalyst activity.	52
4.10	Scheme of the deactivation process in the ZMT catalyst phase.	54
4.11	Copper particle size distribution according to the TEM measurements.	59
5.1	Arrhenius plot for the deactivated catalyst samples. The black box represents the conditions for the catalyst activity measurements.	71
5.2	Deactivation behavior of the three different catalyst samples at 523 K. The straight lines represent the results according to the PLM fit.	72
5.3	TEM images and exemplary representation of the microstructure of CZA1 and CZA2 (a, b) and CZA3 (c, d).	73
5.4	Influence of the aging temperature on the deactivation behavior. Straight lines represent the results according to the PLM fit. The inset in the right figure illustrates the transient activation behavior of CZA3 at 553 K.	73
5.5	Results of the reactive N_2O frontal chromatography. The straight lines represent the trend in the specific copper surface area.	75

5.6	Relative dispersion and particle size distribution according to the MBA Ostwald Ripening model ($E_{\text{ads}} = 185 \text{ kJ mol}^{-1}$). The black line in the inset picture represents the measured distribution, whereas the gray bars represent the modelling result.	76
5.7	Particle Size Distributions according to the random collision model for CZA1 (top row) and CZA2 (bottom row).	77
5.8	Comparison of selected deactivation models with our experimental data for CZA1 (dots and triangles) and the determined PLM fit (straight lines).	78
5.9	Specific catalyst activity in relation to the N ₂ O-RFC copper surface area.	79
5.10	Time-dependent collision number according to the random collision model.	82
5.11	Particle Size Distributions according to TEM and classical coalescence model ($D \approx r^{-4}$) for CZA1 (top) and CZA2 (bottom).	87
6.1	HR-TEM image of the surface termination of the ZnO _x -overgrown Cu nanoparticles in the catalyst CMZ1. The contrast fluctuations seen in the bulk of the Cu particle are Moiré fringes arising due to partial overlapping with other particles.	93
6.2	Correlation of the H ₂ -TPD and N ₂ O-RFC results.	95
6.3	Specific activity of the different catalysts depending on the site type.	98
6.4	Representative TEM images of the catalysts CZA1, CZA2 and CZA3	102
6.5	H ₂ -TPD study on activated methanol synthesis catalysts. Measurement conditions: Q = 100 sccm, m _{cat} = 100 mg (based on calcined precursor), β = 6 K min ⁻¹	104
6.6	Exemplary N ₂ O-RFC curves of two catalysts. In case of CA2, the area used to determine the amount of produced N ₂ is shaded gray. Experimental conditions: T = 308 K, p = 1 bar, Q = 7.5 sccm.	106
6.7	Graphical representation of the activity measurements and determined adsorption capacities according to N ₂ O-RFC, H ₂ -TPD and corresponding amount of oxophilic sites generated by the presence of ZnO.	106
6.8	Comparison of the probe gas capacities of the CZA catalysts in this study if interpreted as specific Cu surface areas with the hypothetical maximal Cu surface area determined by TEM investigations shown in figure 6.4.	107
6.9	Representative HRTEM image of the catalyst CZA1	108
7.1	Exemplary H ₂ -TPD of the polycrystalline copper sample C.	117
7.2	Exemplary reactive N ₂ O frontal chromatography on polycrystalline copper	118
7.3	Comparison of the experimental H ₂ -TPD curve with the parameterized model 1 for polycrystalline copper	121
7.4	Modelling results of H ₂ -TPD spectra from a Cu/ZnO/Al ₂ O ₃ catalyst.	123

7.5	Exemplary description of the desorption signal of H ₂ from polycrystalline copper considering the presence of Cu(111), Cu(110) and Cu(100) facets.	124
7.6	Flow schema of the H ₂ -TPD setup	126

List of Tables

2.1	Overview of the different reaction mechanisms and active sites in literature.[32]	10
2.2	Overview of the most important phases found in a Cu/ZnO/Al ₂ O ₃ precursor.[32]	12
2.3	Tammann and Hüttig temperatures of selected catalyst components and copper halides	16
4.1	Metal ratio and properties of the synthesized catalysts.	36
4.2	Comparison of N ₂ O-RFC and activity results on the different measurement setups and resulting H ₂ -TPD area for sample CZA2.	50
4.3	Qualitative outline of the structural changes after 40 d aging procedure.	51
4.4	Summary of the characterization results of the fresh and aged catalysts.	56
4.5	Relative amount of ZnAl ₂ O ₄ spinell compared to the copper phase as given by the Rietveld analysis.	58
4.6	Summary of the H ₂ -TPD and N ₂ O-RFC adsorption capacities on fresh and aged catalyst.	58
4.7	Mean copper particle diameter according to the TEM measurements (d _{Cu,TEM}).	58
5.1	Metal ratio, BET surface area and N ₂ O-RFC surface area of the analyzed catalyst samples.	66
5.2	Aging conditions presented in this study.	68
5.3	Activation energy EA before and after the aging process.	71
5.4	Rate constant and reaction order of catalyst deactivation according to the PLM fit.	74
6.1	Compositions and BET surface areas of the catalysts used.	94
6.2	Specific copper surface areas (SSA) and defect concentrations in SSA equivalents. (n.d. = not determined)	97
6.3	Sample overview and database numbers of selected catalysts.	101
7.1	Summary of the characterization results of C and CA.	115

7.2	Facet distribution according to the Wulff construction and copper surface atom density per facet.	119
7.3	Summary of the measurement and fitting results.	121
7.4	Optimized parameters for model 1 and 2. In both models a fixed prefactor of $k_{0,des} = 3.75 \cdot 10^{10} \text{s}^{-1}$ is used.	122

Abschließende Erklärung

Die von mir vorgelegte Arbeit ist von Herrn Prof. Dr.-Ing. Kai-Olaf Hinrichsen (Technische Universität München – Lehrstuhl I für Technische Chemie) betreut worden.

Versicherung

Ich versichere hiermit, dass ich die von mir vorgelegte Arbeit selbständig und ohne unzulässige Hilfe angefertigt, die benutzten Quellen und Hilfsmittel aus der Primär- und Sekundärliteratur vollständig angegeben und die Stellen der Arbeit, einschließlich Tabellen, Karten und Abbildungen, die dieser Literatur im Wortlaut oder dem Sinn nach entnommen sind, in jedem Einzelfall als Entlehnung kenntlich gemacht habe. Desweiteren versichere ich, dass diese Arbeit bisher von mir nicht an Dritte weitergeleitet oder veröffentlicht worden ist. Die Bestimmungen der geltenden Promotionsordnung der Technischen Universität München sind von mir beachtet worden.

Bemerkung zum Internet

Das Internet wurde während der gesamten Arbeit für Recherchen und Gegenrecherchen genutzt. Viele der hier gegebenen Stichworte, Referenzen und sonstige Angaben können im Internet nachgeprüft werden. Es werden aber keine Quellen angegeben, da sämtliche in dieser Arbeit getroffenen Aussagen durch die genannten Literaturquellen vollständig abgedeckt sind. Wegen der Schnellebigkeit des Mediums „Internet“ scheint die Angabe von Adressen zu Webseiten auch nur bedingt verlässlich. Dennoch war das Internet für das Gelingen dieser Arbeit ein wichtiges Hilfsmittel.

Garching, December 19, 2014

Matthias Fichtl